# Synthesis, Characterizations and Applications of Nanomaterials' based Electrodes

Ph.D. Thesis

## By **Devesh Kumar Pathak**



## DEPARTMENT OF PHYSICS INDIAN INSTITUTE OF TECHNOLOGY INDORE

February, 2021

# Synthesis, Characterizations and Applications of Nanomaterials' based Electrodes

#### **A THESIS**

Submitted in partial fulfillment of the requirements for the award of the degree

of

### DOCTOR OF PHILOSOPHY

by **Devesh Kumar Pathak** 



## DEPARTMENT OF PHYSICS INDIAN INSTITUTE OF TECHNOLOGY INDORE

February, 2021



#### INDIAN INSTITUTE OF TECHNOLOGY INDORE

#### CANDIDATE'S DECLARATION

I hereby certify that the work which is being presented in the thesis entitled Synthesis, Characterizations and Applications of Nanomaterials' based Electrodes in the partial fulfillment of the requirements for the award of the degree of **Doctor of Philosophy** and submitted in the **Department** of Physics, Indian Institute of Technology Indore, is an authentic record of my own work carried out during the time period from July 2017 to February 2021 under the supervision of Dr. Rajesh Kumar, Associate Professor, Indian Institute of Technology Indore.

The matter presented in this thesis has not been submitted by me for the award of any other degree of this or any other institute.

25/02/2021 Signature of the student with date (Devesh Kumar Pathak)

This is to certify that the above statement made by the candidate is correct to the best of my/our knowledge.

Signature of Thesis Supervisor with date 25/02/2021

(Dr. Rajesh Kumar)

**Devesh Kumar Pathak** has successfully given his/her Ph.D. Oral Examination held on July 23, 2021.

Signature of Chairperson (OEB)

Date: 23/07/2021

Date: 23/07/2021

Signature of External Examiner Signature(s) of Thesis Supervisor(s)

Date: 23/07/2021

SC

Signature of PSPC Member #1

23/07/2021

Signature of PSPC Member #2

Date: 23/07/2021

Dedicated

to

my family

#### Acknowledgements

Uphill battle is not won by a single person it requires a dedicated team, who performs and guides in every step. Through Ph.D journey, I have learned a lot as a PhD researcher but have also grown as a person who had this incredible opportunity to engage with elderly partition migrants. This thesis is also the result of many experiences that I have encountered at IITI from remarkable individuals who I also wish to acknowledge and thanks.

First and foremost, I thank God Almighty for giving me the wisdom, guidance and understanding to carry out and complete the most significant learning experience of my academic journey with perseverance, zeal and patience. I would like to acknowledge my indebtedness and render my warmest thanks to my supervisor, Dr. Rajesh Kumar, who made this work possible. His friendly guidance and expert advice have been invaluable throughout all stages of my work. Ever since, Dr. Rajesh Kumar has supported me not only by providing a research assistantship, but also academically and emotionally through the bumpy road to finish this thesis. I appreciate all his contributions of time and ideas to make my Ph.D. experience productive and stimulating. The joy and enthusiasm he has for his research was motivational for me, even during difficult times in the Ph.D. pursuit. I am also thankful of your excellency toward a successful teacher, supervisor, administrator, poet, script writer, caring nature which always encouraged me to be like you.

I would also wish to express my gratitude to Dr. Pankaj R Sagdeo for extended discussions and valuable suggestions since my first day at institute who has contributed greatly on my Ph.D. Journey. I take this opportunity to sincerely acknowledge Dr. Sudeshna Chattopadhyay and Dr. Sanjay K Singh for being a member of my research progress evaluation committee (PSPC). Their evaluation, comments, and suggestion help me a lot to improve my research work.

I want to express my gratitude to Director, IIT Indore for his support and motivation which enabled me to successfully complete my journey. On this occasion, I thank all the school teachers who taught me from the initial education of 'first letter A' and made me eligible to take 'utmost degree'. In this sequence, I am happy to acknowledge Dr. Nandan Singh, my M.Sc. faculty, who encouraged me to extend my basic science through a research platform. I would like to always remember the time spend with my M.Sc. friends, especially Dr. Devendra Singh Bhakuni, with whom a discussion of physics used to leave a new zeal and a new goal.

In this arduous journey of mine (Ph.D.), there are people who not only guided me but also work with me on equal footing. I can never forget the amazing support given by Dr. Aanchal Sati, who always took the positive side and encouraged me to do my Ph.D. especially during the time when I was tired and irritable. I would also like to also acknowledge Dr. Vikash Mishra, who helped me at each and every step since my first day in lab and also helped me to make my friendship in almost all departments for carrying out my research work. Since, it is always be a little tough to pursue the research work without the knowledge transfer and training period getting from the lab senior, therefore it is an opportunity here to acknowledge Dr. Shailendra Saxena, Dr. Surykant Mishra, Dr. Priyanka Yogi, Dr. Kamal Warshi, Dr. Harimohan Rai, Dr. K D Shukla, Dr. Swarup Roy for providing the best research platform.

A flower needs both sun and air to bloom and any thesis would not be possible without colleagues helps to make the environment more energetic and happy. I was lucky to spend the Ph.D. time with my colleagues Dr. Anjali Chaudhary, Manushree Tanwar, Chanchal Rani, Suchita Kandpal, Tanushree Ghosh, Anil Kumar, Meenal, Omkar, Nischal, Kailash, Neeshu, Ritika, Rachit, Keertivasan, Rahul, Monika, Bajrang, Simran, Ritu. I would like to extend my thanks to people, Ajaib, Preeti, Kuber, Prashant, Ekta, KC, Ratinavelu, Anil, Rinki, Mithun da, Vivek Gupta, Diksha Tiwari, Mayank, Sarath, Ruhul

badminton group, and all phd-2017 batch friends, outside my lab for their help and support.

I would like to thank Department of Physics and staff members (Mr. Sunny, Mr. Nitin Upadhay, Mr. Ved Prakash, Mr. Prashant) for their academic help, financial support. All staffs of SIC facility at IIT Indore, Mr. Kinny Pandey, Mr. Ghanshyam, is highly acknowledged for their valuable support. I would like to thank Dr. Shilpa Raut and other staff member for taking care physically with keeping good health condition. I would like to thank the all security staffs for caring us and housekeeping staffs to make the institute clean.

I would like to thank again my supervisor on setting up an interdisciplinary collaboration with BSBE (Dr. Hem Chandra Jha) and Civil Engineering (Prof. Sandeep Chaudhary) and Chemistry (Prof. Rajneesh Misra) departments at IIT Indore. Prof. V D Vanker (IIT-Delhi), Dr. Vivek Kumar (IIIT Chennai), Prof. Salim (Jamia Islamia, New Delhi), Dr. Sameera (Guru Jambheshwar University, Hisar), Mr. U K Gautam (RRCAT), Prof. Herbert Pfuner (Leibniz University, Hannover, Germany), Dr. Ajay Kumar Kushawaha (IIT Indore) are also highly acknowledged for fruitful discussion and working together.

Last but least, I want to thank all staff members of IIT Indore for providing all convenience and making this journey easy. I specially want to thank all academic staff for helping me in best possible ways at various labels. Besides this, several people have knowingly and unknowingly helped me in the successful completion of my thesis.

I would like to thank my parents and my lovely brother (Er. Tarun) for their constant motivation, support, and all the sacrifices they have made for me until the submission of the thesis. I am grateful for the financial support from the Council of Scientific and Industrial Research (CSIR).

11 Trail

.....Devesh Kumar Pathak

#### **Abstract**

In the modern science and technology, a new field, nanoscience, has played an important role in the overall development towards addressing several challenging problems related to society. In recent times, a rise in research areas with societal impact has been observed, with nanoscience and nanotechnology being one such area especially where nanodevices are in focus. It has been emerging rapidly and coming up with new solutions to long researched problems in the areas of energy, electronics, etc. When it comes to electronics, the expectations from nanoscience and nanotechnology is increased because of its reputation in terms of deliverables in applied research involving sensing, energy storage, solar cells, memory, electrochromic devices, etc. Looking at a broader picture, finding new materials and reengineering the existing ones are the need of the moment. With the advent of nanotechnology in material science, various new properties can be observed from same compound by simply controlling the size when miniaturized to the nanoscale. At the same time, other properties get improved due to subtle physics taking place at the nanoscales. In this context it is important to underline importance of various materials like semiconducting oxide, transition metal oxides, complex/hybrid compound, layer double hydroxide etc. for their functional use in variety of applications. Therefore, various inorganic and organic materials and their possible combination in a designed paradigm found to make an improved and power efficient device.

Looking at various perspectives of material and their applications, my research work has been summarized in this thesis with primarily focuses on fabricating the inorganic transition metal oxide nanostructures' based electrodes, e.g. NiO,  $Co_3O_4$ ,  $TiO_2$ , PB etc., followed by their application in device engineering. Various inorganic materials for making improved electrochromism in pre-designed display like structure have been explored after the replacement of synthesis process. Therefore, a dense nanofilm of  $Co_3O_4$  is synthesized using constant current electrodeposition on a conducting transparent electrode that works not

only as a counter electrode but also shows electrochromic (EC) properties on its own. The isolated active nano-Co<sub>3</sub>O<sub>4</sub> electrode shows reduction in the redox potential and good color contrast between its yellowish transparent and dark states at different bias conditions. The electrode shows improved color contrast, stability, and cycle life. In situ spectroelectrochemical studies of the 'nano' electrode reveals that the bias induced redox activity of the metal oxide leads to the color change between yellowish and opaque states. The bias-induced color change makes it an active EC counter-ion electrode for appropriate solid-state EC devices.

A solid state electrochromic devices fabricated in two paradigms namely, inorganic/organic ("hybrid" in combination of viologen and Co<sub>3</sub>O<sub>4</sub>) and inorganic/inorganic ("all-inorganic", in a combination of Prussian blue and Co<sub>3</sub>O<sub>4</sub>) in which the fabricated Co<sub>3</sub>O<sub>4</sub> electrode is a common electrode and improves the performance. The performance of the final device with similar or dissimilar materials' combination has been checked through switching time, switching speed, color contrast and coloration efficiency. In-situ spectroscopy techniques like UV-Visible and Raman have an extraordinary advantage to understand and to explain the mechanism for coloring and bleaching state of electrochromic active materials. A good color contrast of hybrid device appears between its yellow and blue states under different bias conditions have been observed, which leads to overall performance enhancement. The solid state device shows an improved efficiency of as high as 360 cm<sup>2</sup>/C and a switching time of as low as 500 ms. All inorganic solid-state device performance between multiple colors with an applied bias occurs less than a couple of volts. A moderate color contrast of ~40% with 1.5 s switching time has been observed with showing stability for more than 900 s of continuous switching. A redox driven electrochromic behavior of individual electrodes makes it possible for the solid-state device to show beautiful colors with a small applied bias with showing the coloration efficiency of 250cm<sup>2</sup>/C. On the whole an "all-inorganic" and "hybrid" solid state electrochromic device

have been successfully fabricated which shows performance for real applications.

To exhibit the multifunctional role of metal oxides, this thesis work also gives some glimpses over the bifunctional role of material toward electrochromic and glucose sensing application. After characterization of metal oxides followed by electrochemistry, uniform nanoneedles of binary oxide (Ni and Co) were synthesized on appropriate conducting substrates [fluorine-doped tin oxide (FTO) coated glass and carbon cloth (CC)] for the investigation of dual application. A low-operating-voltage (+2 V) color modulation with 50% contrast between the whitish translucent and dark-brown colors was achieved from the nanoneedle grown on a transparent FTO substrate. Furthermore, additionally NiCo<sub>2</sub>O<sub>4</sub> nanoneedles grown on a CC substrate, with an enhanced exposed surface area, showed selective glucose-sensing properties with a very high sensitivity of 3000 μA/mM/cm<sup>2</sup>, as revealed using detailed electrochemical and impedance spectroscopic measurements.

Beyond the electrochemistry, electron emission property exploited in field emission display, of metal oxide nanostructures which are known electrochromic materials used in electrochromic displays. Field emission properties of NiO nanopetals and TiO<sub>2</sub> nanorods have been studied and analyzed within the frame work of Fowler-Nordheim formulation. An alternative formulation for the interpretation of field emission properties has been developed and validated using theoretical fitting of the experimentally observed data. The proposed model addresses the little incompleteness presence in the traditionally used Fowler-Nordheim model. Therefore, this thesis work provides a new pathway on searching those materials which can show its diversity in multifunctional applications.



#### LIST OF PUBLICATION

#### (a) Peer reviewed Journal (Thesis)

- D K Pathak, A Chaudhary, M Tanwar, U K Goutam, R Kumar, "Nano-cobalt oxide/viologen hybrid solid state device: Electrochromism beyond chemical cell", Applied Physics Letters, 2020, 116, 14, 141901
- D K Pathak , A Chaudhary, T Ghosh, S Kandpal, M Tanwar, C Rani, R Kumar, "Prussian Blue-Cobalt Oxide Double Layer for Efficient All-Inorganic MulticolorECDs", ACS Appl. Electron. Mater. 2020, 2, 6, 1768–1773
- 3. **Devesh K. Pathak**, A Chaudhary, M Tanwar, U K. Goutam, P Mondal, and R Kumar, Nickel Cobalt Oxide Nanoneedles for EC Glucose Sensors, **ACS Appl. Nano Mater.**,2021, 4, 2, 2143–2152
- 4. **D K Pathak**, S Mishra, A Chaudhary, M Tanwar, P Yogi, P R Sagdeo, R Kumar, "Improved analytical framework for quantifying FEfrom nanostructures", **Materials Chemistry and Physics**, 2020, 245, 122686
- D K Pathak, A Chaudhary, M Tanwar, U K Goutam, Prof. H pfnur, R Kumar, "Chrornopotentiometric deposition of Nano-Cobalt oxide for EC auxiliary active electrode application", Physica status solidi (a), 2020, Phy. Status Solidi A, 2020, 217, 2000173
- D K Pathak, A Chaudhary, S Mishra, P Yogi, P R Sagdeo, R Kumar, "Improved FEfrom appropriately packed TNRs: Designing the miniaturization", Superlattices and Microstructures, 2019, 126, 1-7
- D K Pathak, A Chaudhary, S Mishra, P Yogi, S K Saxena, P R Sagdeo, R Kumar, "Precursor concentration dependent hydrothermal NiO NPs: Tuning morphology for efficient applications", Superlattices and Microstructures, 2019, 125, 138-143

- 8. **Devesh K Pathak,** M Tanwar, C Rani, S Kandpal, T Ghosh, P Yogi, T Anusuya, P Mondal, A Chaudhary, V Kumar and R Kumar, Quantifying Size Dependent Electron Emission from Silicon Nanowires Array, **Silicon** (In press)
- Devesh K Pathak, A Chaudhary, M Tanwar, S Kandpal, T Ghosh, C Rani and R Kumar, Low voltage color modulation in hydrothermally grown Ni-Co nanoneedles for EC application, IET Nanodielectric, 2021,4,75-80

#### (b) Peer reviewed Journal (as a contributory author)

- Vivek Gupta, Devesh K Pathak, Rajesh Kumar, Ankur Miglani, Salman Siddique, Sandeep Chaudhary, Production of colored bi-layered bricks from stone processing wastes: Structural and spectroscopic characterization, Construction and Building Materials, 2021, 278, 5, 122339
- Anjali Chaudhary, Gangala SivaKumar, Devesh Kumar Pathak, M. Tanwar, Rajneesh Misra and Rajesh Kumar, Pentafluorophenyl Substituted Fulleropyrrolidine: A molecule enabling the most efficient flexibleECDs with fast switching, J. Mater. Chem. C, 2021 (online, 10.1039/D0TC04991C)
- Devesh K Pathak, M Tanwar, A Chaudhary, S K Saxena, R Kumar, "Unintended Deviation of Fermi Level from Band Edge in Fractal Silicon Nanostructures: Consequence of Dopants' Zonal Depletion", J. Phys. Chem. C 2020, 124, 30, 16675–16679
- A. Chaudhary, Devesh K Pathak, S Kandpal, T Ghosh, M Tanwar, R Kumar, "Raw hibiscus extract as redox active biomaterial for novel herbalECDs", Solar Energy Materials and Solar Cells, 2020, 215, 110588
- A Chaudhary, M Poddar Devesh K Pathak, R Misra, R Kumar, "Electron Donor Ferrocenyl Phenothiazine: Counter Ion for Improving All-Organic Electrochromism" ACS Appl. Electron. Mater. 2020, 2, 9, 2994–3000

- A Chaudhary, Devesh K Pathak, M Tanwar, R Kumar, "Tracking Dynamic Doping in a SolidStateECDs: Raman Microscopy Validates the Switching Mechanism" Analytical Chemistry, 2020, 92, 8, 6088-6093
- 7. M Sharma, S Rani, **Devesh K Pathak**, R Bhatia, R Kumar, I Sameera, "Manifestation of Anharmonicities in Terms of Phonon Modes' Energy and Lifetime in Multiwall Carbon Nanotubes", **Carbon**, 2021, 171, 568-574
- A Chaudhary, Devesh K Pathak, M Tanwar, J Koch, H Pfnür, R Kumar, "PolythiophenenanoWO3 bilayer as an EC infrared filter: a transparent heat shield", J. Mater. Chem. C, 2020, 8, 1773-1780
- A Chudhary, Devesh K Pathak, S Mishra, P Yogi, P R Sagdeo, R Kumar, "Enhancing Viologen's Electrochromism by Incorporating Thiophene: A Step Toward All-Organic Flexible Device", Phys. Status Solidi A 2019, 216, 1800680
- 10. M Tanwar, Devesh K Pathak, A Chaudhary, P Yogi, S K Saxena, R Kumar, "Mapping longitudinal inhomogeneity in nanostructures using cross-sectional spatial Raman imaging", J. Phys. Chem. C 2020, 124, 11, 6467–6471
- 11. V Gupta, **Devesh K Pathak**, S Siddique, R Kumar, Sandeep Chaudhary, "Study on the mineral phase characteristics of various Indian biomass and coal fly ash for its use in masonry construction products", **Construction and Building Materials**, 2020, 235, 117413
- 12. A Chaudhary, Devesh K Pathak, S Mishra, P Yogi, P R Sagdeo, R Kumar, "Polythiopheneviologen bilayer for electro-trichromic device", Solar Energy Materials and Solar Cells, 2018,188, 249-254
- 13. A Chaudhary, Devesh K Pathak, M Tanwar, P Yogi, P R Sagdeo, R Kumar, "Polythiophene— PCBM-based allorganicECDs: fast and flexible", ACS Appl. Electron. Mater. 2019, 1, 1, 58–63

- 14. A Chaudhary Devesh K Pathak, M Tanwar, P R Sagdeo, R Kumar, "Prussian blue-viologen inorganic—organic hybrid blend for improved EC performance", ACS Appl. Electron. Mater., 2019, 1, 6, 892–899
- 15. D Tiwari, S Jakhmola, **Devesh K Pathak**, R Kumar, H C Jha, "Temporal In Vitro Raman Spectroscopy for Monitoring Replication Kinetics of Epstein–Barr Virus Infection in Glial Cells", **ACS Omega**, 2020, 5, 45, 29547–29560
- 16. M Tanwar, A Chaudhary, Devesh K Pathak, P Yogi, S K Saxena, PR Sagdeo, R Kumar, "Deconvoluting diffuse reflectance spectra for retrieving nanostructures' size details: an easy and efficient approach", J. Phys. Chem. A, 2019, 123, 16, 3607–3614
- 17. P Yogi, S K Saxena, A Chaudhary, Devesh K Pathak, S Mishra, P Mondal, B Joshi, P R Sagdeo, R Kumar, "Porous Silicon's fractal nature revisited" Superlattices and Microstructures, 2018, 120, 141-147
- 18. P Yogi, M Tanwar, S K Saxena, S Mishra, **Devesh K Pathak**, A Chaudhary, P R Sagdeo, R Kumar, "Quantifying the short range order in amorphous silicon by Raman scattering", **Anal. Chem.**, 2018, 90, 8123-8129

### **Contents**

Ack	knowle	edgement	I
Abs	tract		V
List	of Pu	blications	ix
List	of Fig	gures	xix
List	of Ta	able	xxiii
List	t of Ab	obreviations	xxiv
Cha	pter 1:	Introduction	1
1.1	A pre	eliminary discussion	2
1.2	Nano	technology in various fields	4
	1.2.1	Chemical Science	4
	1.2.2	Physical Science	5
	1.2.3	Biological Science	6
	1.2.4	Engineering	7
1.3	Elect	rochromic	8
	1.3.1	Appearance of Color	9
	1.3.2	Types of Electrochromic Material	10
	1.3.3	Electrochemistry of EC materials	13
	1.3.4	EC Device Formation	14
	1.3.5	Device Performance	15
1.4	Multi	ifunctional Application of EC Material	17
	1.4.1	Electrochromic memory	17
	1.4.2	Energy Storage and Sensing	18
	1.4.3	Heat Shielding	18
1.5	Elect	ron Field Emission	19
	1.5.1	Experimental and Quantum Mechanical	_
	Aı	pproach	20

	1.5.2	Fowler-Nordheim (F-N) Framework	22
1.6	Objec	ctive	23
1.7	Orga	nization of Thesis	24
Cha	pter 2:	<b>Experimental Details</b>	27
2.1	Mate	rial Synthesis Process	28
	2.1.1	Hydrothermal Synthesis	12
	2.1.2	Electrodeposition technique	30
	2.1.3	Spin coating and Drop casting	31
2.2	Chara	acterisation Techniques	32
	2.2.1	Scanning electron microscopy	32
	2.2.2	Transmission electron microscopy	34
	2.2.3	Atomic Electron Microscopy	36
	2.2.4	X-ray Diffraction	37
	2.2.5	Raman spectroscopy	39
	2.2.6	X-ray Photoelectron spectroscopy	41
	2.2.7	UV-Visible spectroscopy	43
2.3	Elect	rochemical measurement	45
	2.3.1	Linear Sweep Voltammetry	46
	2.3.2	Cyclic Voltammetry	46
	2.3.3	Chronopotentiometry	46
	2.3.4	Chronoamperometry	47
	2.3.5	Nyquist plot	47
2.4	Samp	ole preparation recipes	47
	2.6.1	Synthesis of NiO Nanopetals	47
	2.6.2	Synthesis of TiO <sub>2</sub> Nanorod	48
	2.6.3	Synthesis of NiCo <sub>2</sub> O <sub>4</sub> Nanoneedle	48
	2.6.4	Electrodeposition of Nano-Co <sub>3</sub> O <sub>4</sub>	49
	2.6.5	Electrodeposition of Nano-Purssian Blue film	49
	2.6.6	Synthesis of Ethyl Viologen gel	50

Cha	pter 3: Inorganic Nanomaterials for EC	
Elec	trodes	51
3.1	Transition metal oxide: Inoraganic EC material	52
	3.1.1 Background study	52
	3.1.2 Redox polarity dependent EC	52
3.2	Nickel oxide	54
	3.2.1 Characterisation of prepared NiO film	54
	3.2.2 Electrochemistry of Nickel oxide	57
3.3	Titanium Oxide Nanostructures	58
	3.3.1 Characterisation of Titanium oxide	58
	3.3.2 Electrochemical activity of TiO <sub>2</sub> @FTO	61
3.4	Cobalt oxide	63
	3.4.1 Characterisation of Cobalt oxide	64
	3.4.2 Spectroelectrochemistry of Cobalt oxide and	
	Efficient Elctrochromism	66
3.5	Prussian blue	69
	3.5.1 Characterisation of Prussian blue solid thin film	70
	3.5.2 Electrochemistry of PB thin film	70
3.6	Summary	73
Cha	pter 4: All-Inorganic & Hybrid EC Solid State	
Devi		75
		13
4.1	Electrochromic Double layer Device and	
	Engineering	76
4.2	Nano-Cobalt Oxide/Viologen Hybrid Solid	
	State Electrochromic device	77
	4.2.1 Device Fabrication and Characterization	78
	4.2.2 Electrochromic Performance of Device	81

4.3	An "all-inorganic" Nano-Cobalt Oxide/Prussian	84
	Blue Electrochromic Device	85
	4.3.1 Electrochemistry of PB- and Co <sub>3</sub> O <sub>4</sub> -Electrodes	87
	4.3.2 Device Fabrication and characterization	90
	4.3.3 EC Performance of Device	93
4.4	Summary	
	pter 5: Bifunctional Application of Nano	0.5
Nick	tel Cobalt Oxide	95
5.1	Binary transition metal oxide nanostructures	
	and their application	96
5.2	Preparation of NiCo <sub>2</sub> O <sub>4</sub> Nanoneddle	97
	5.2.1 Characterization of NiCo <sub>2</sub> O <sub>4</sub>	98
	5.2.2 Morphology of NiCo <sub>2</sub> O <sub>4</sub>	101
	5.2.3 Elemental Composition validation of NiCo <sub>2</sub> O <sub>4</sub>	103
5.3	Electrochromism of Nano-NiCo <sub>2</sub> O <sub>4</sub>	105
5.4	Glucose- Sensing of Nano-NiCo <sub>2</sub> O <sub>4</sub>	108
5.5	Summary	112
Cha	pter 6: Metal Oxides Nanostructures: Field	
Emi	tters	115
6.1	Electron Field Emission	116
6.2	NiO Nanopetals	116
	6.2.1 Reaction Route and Surface Analysis	117
	6.2.2 Geometrical Analysis	119
	6.2.3 Electron Field Emission	121
6.3	Field Emission from Packed TiO <sub>2</sub> Nanorod	123
	6.3.1 Structural analysis and characterization of TNR	124
	6.3.2 Field Emission from TNR	124

6.4	Alternate Analytical FE Framework	128
	6.4.1 Background study	128
	6.4.2 Origin of New Framework: Two Validation	129
6.5	Summary	136
•	pter 7: Conclusion, Summary and Future	139
scop	e	139
7.1	Conclusion and Summary	142
7.2	New Findings Reposted in the Thesis	143
7.3	Future Scope of the Work	143
APP	ENDIX-	145
<b>A.1</b> ]	Diode behavior of hybrid ECDs	145
<b>A.2</b>	Quantifying Electron Emission from Silicon Nanowires	
using	new framework	
		146
Refe	erences	149



### **List of Figures**

Figure 1.1	Electron micrograph of a few nanomaterials	3
Figure 1.2	Application of electrochromism in (a) aircraft window, (b) specs, (c) car's rear-view mirrors, (d) flexible digital displays and (e) meeting room at Microsoft head office.	9
Figure 1.3	Color wheel to check the appearance definite colour with absorbance of others.	10
Figure 1.4 Figure 1.5	Schematic electrochromic device representation.  (a) Schematic representation of arrangement for	15
	electron emission measurement from nanostructure material, (b) actual photograph of field emission measurement setup and the two electrode arrangement made of copper (inset), (c) distribution profile of potential as a function of distance from the nano-structure showing image charge potential (green dotted line), applied potential (blue dotted line) and effective rounded edge triangular barrier (red bold line).	21
Figure 2.1	Schematic diagram showing a typical hydrothermal setup.	29
Figure 2.2	Schematic representation of an electrochemical cell used for electrodeposition using three electrode systems	31
Figure 2.3	Schematic illustration of Spin coating (a) and Drop casting (b) techniques	31
Figure 2.4	Schematic illustration of a FE scanning electron microscope (SEM).	33
Figure 2.5	Schematic illustration of transmission electron microscope.	35
Figure 2.6	Schematic illustration of atomic force microscopy with the different operating contact mode.	36
Figure 2.7	Schematic illustration of an X-ray diffractometer and diffraction from atomic	38
Figure 2.8	planes. Schematic illustration of a typical Raman	40
Figure 2.9	spectrometer. Schematic illustration of X-ray photo electron spectroscopy.	42
Figure 2.10	Schematic illustration of UV-Visible spectrospeopy in absorption/transmission mode.	45

Figure 3.1	(a) X-ray diffraction pattern of NiO NPs along with (b) Raman Spectrum, (c) Transmission and absorption (inset), (d) diffused reflectance spectroscopy (e) top view-SEM, (f) Zoomed view at 200nm scale (g) TEM and (h) corresponding SAED pattern.	56
Figure 3.2	(a) CV of NiO@ITO in 1M KOH (aq) electrolyte with two chromic state and (b) Optical absorption of colored (brown) and bleached (transparent) state of NiO@ITO electrode under two different bias states.	58
Figure 3.3	Basic characterization of the hydrothermally deposited TiO <sub>2</sub> using (a) XRD, (b) Raman spectroscopy, (c) Transmission and absorption (inset) spectroscopy, (d) DRS, (e) top view SEM and (f) cross-sectional SEM, (g) HRTEM image showing lattice planes and its line profile (inset) and (h) Fast Fourier Transform pattern obtained using ImageJ.	60
Figure 3.4	(a) CV of EC active TNR showing cathodic nature along with its whitish and bluish chromic states (actual image in background) and (b) optical absorption for colored (black curve) and bleached state (red curve) of TNR (zoomed portion in inset).	63
Figure 3.5	Surface morphology of electrodeposited film as observed using (a) SEM with inset showing surface profile obtained using Image J and (b) on fluorine doped tin oxide (FTO) electrode as seen using (a) SEM showing cracks (inset, scale bar: 200 nm) and (b) AFM.	65
Figure 3.6	(a) X-ray diffraction pattern showing Co <sub>3</sub> O <sub>4</sub> peak (*) and FTO peaks (unmarked), (b) Raman spectrum and (c, d) XPS from Co <sub>3</sub> O <sub>4</sub> film.	66
Figure 3.7	(a) Cyclic voltammogram from $Co_3O_4$ film in 0.1M KOH electrolyte and the actual image of the electrode in the background corresponding to the applied bias, (b) bias dependent in-situ absorption spectra in an electrochemical cell, (c) absorption kinetics of $Co_3O_4$ electrode in the same electrochemical cell having switching between $\pm 2V$ (with one response in inset) along with its chronoamperometric response with respect to single applied voltage pulse (d).	67
Figure 3.8	(a) SEM image and (b) Raman spectrum of asprepared PB thin film on FTO substrate.	70
Figure 3.9	Schematic representation of spectroelectrochemisty of PB@ITO electrode in three electrode system (a), CV measurement of	73

PB electrode in KCl electrolyte (b), In-situ
Optical spectroscopy of PB electrode under the
effect of external biasing (c),
Chronoamperometric measurement of current
with respect to the applied potential pules
toggling between -2V to +2V (d), Switching
absorption cycle of PB electrode for coloration
and bleaching state (e), (f) Zoomed portion of
one complete absorption cycle

Figure 4.1	(a) CV curve of Co <sub>3</sub> O <sub>4</sub> @FTO electrode with changing EC state from pale yellow to brown/black under anodic scan and (b) CV curve of EV solution at bare FTO substrate with changing colour from transparent to blue color under cathodic scan.	78
Figure 4.2	Schematic representation of fabrication process involved in making solid-state hybrid inorganic-organic ECD.	79
Figure 4.3	(a) Schematic representation and actual images of device in cross bar geometry with and without bias, (b) in-situ absorbance spectra of fabricated device under three biasing states, (c) in-situ Raman spectroscopy of device 'with' and 'without' bias (1.8V) condition	81
Figure 4.4	(a) Absorption switching kinetics of device with switching voltage from -1V to 1.8V of fabricated device, (b) color (ON) and bleached (OFF) representation through one absorption cycle.	82
Figure 4.5	(a) Current response of the devices under 1.8V/-1V potential pulse, (b) Optical density variation as a function of charge density.	83
Figure 4.6	(a) Schematic illustration of experimental arrangement showing Co <sub>3</sub> O <sub>4</sub> and PB electrodes dipped in an electrochemical cell, (b-d) with actual images of the set up under different operational conditions and cyclic voltammogram curves of (e) Co <sub>3</sub> O <sub>4</sub> and (f) PB electrodes	87
Figure 4.7	Schematic illustration of fabricated device in (a) unbiased state (0 V) and biased with (b) 2 V and (c) -1.5 V.	89
Figure 4.8	(a) In-situ bias-dependent optical absorption spectra from device under different bias conditions (i)-(iii) along with the actual image of device (insets) and (b) representation of each state on CIE diagram.	90

Figure 4.9	(a) One absorbance switching cycle of the device under bias pulse with extreme bias of 2V & -1.5 V, (b) extended absorbance switching for 300 pulses along with variation of current with applied bias in (c), and (d) variation in Optical density with charge density.	91
Figure 5.1	Schematic showing growth process of Ni-Co nanoneedle over FTO and carbon cloth	98
Figure 5.2	substrates using hydrothermal process.  (a) XRD pattern, (b) Raman spectrum, (c) diffused reflectance spectroscopy for finding the band gap using Tauc-plot and (d) BET curve performed under N <sub>2</sub> absorption de-absorption process from the sample in powder form	100
Figure 5.3	obtained by scratching off the film.  (a) Top view of nanoneddle NiCo <sub>2</sub> O <sub>4</sub> @FTO film with enlarged view at 200 nm (b), (c) Top view of nanoneddle NiCo <sub>2</sub> O <sub>4</sub> @CC film (CC in inset) with enlarged view at 1 μm (d). (e) EDX analysis of film over FTO substrate and their (f) different elemental composition ratio, (g) TEM analysis of one nanoneddle with the average diameter (inset) of 45 nm, (h) SAED pattern of nanoneddle.	103
Figure 5.4	Synchrotron source XPS curves from NiCo <sub>2</sub> O <sub>4</sub> nanoneedle in (a) full scan, (b) Ni 2p edge, (c)	105
Figure 5.5	Co 2p edge and (d) O 1s edge scans.  (a) CV curves from NiCo2O4@FTO with colour switching for different cycles and, (b) insitu UV-Visible spectroscopy of NiCo2O4@FTO electrode under the external bias of +2V and -1V.	107
Figure 5.6	(a) CV performance of NiCo <sub>2</sub> O <sub>4</sub> @CC WE under different scan rate, (b) Variation of oxidation and reduction current with respect to scan rate, (c) Glucose sensing current response with varying concentration from 1mM to 8mM (d) The variation of sensing current with the varying glucose concentration, (e) Chronoamperometric techniques for measuring exclusive glucose sensing, (f) EIS (Nyquist plot) data of NiCo <sub>2</sub> O <sub>4</sub> @CC with and without presence of glucose.	. 111
Figure 6.1	NiO NPs' micrographs of samples prepared with Ni(NO <sub>3</sub> ) <sub>2</sub> concentration of (a) 60mM, (b) 80mM and (c) 100mM along with (d) Schematic of experimental set up.	118
Figure 6.2	(a) Surface plots extracted from SEM images	120

	using ImageJ and (b) Variation of average petal thickness and petal density as a function of			
	precursor concentration			
Figure 6.3	1	22		
rigure 0.5	characterized NiO NPs with turn on field 1.2			
	V/mm, (b) F-N plot for finding the estimate			
	value of enhancement factor $\beta$			
Figure 6.4	•	26		
119410 011	nanorods measured in a parallel plate geometry	_0		
	(inset). (b) F-N plot in linear relationship for			
	estimation of enhancement factor, (c) Schematic			
	representation of favorable (the green panel)			
	and non-favorable (red panels) situations for			
	efficient field emission.			
Figure 6.5		32		
1 1941 0 010	applied electric field for (a) NiO NPs	-		
	(schematic of electrode geometry in top inset)			
	and (b) TNRs. Bottom insets in (a) and (b)			
	shows portion of corresponding microstructures.			
Figure 6.6		34		
<b>g</b>	depiction of electron tunneling from (a) bulk			
	material and (b) a nanostructured material. The			
	energy levels and behavior of electron wave-			
	function in different regions with dotted plane			
	as the potential profile under applied electric			
	field is shown in the left panel. The right panel			
	shows the effect of quantization of energy bands			
	on effective work function ( $\phi_{eff}$ ) which is less			
	that the bulk counterpart $(\phi_b)$ and the tunneling			
	widths $(\tau_b \& \tau_n)$ under two different applied			
	biases ( $E_{app}$ and $E_{nano}$ ).			
	• • • • • • • • • • • • • • • • • • • •			
List of Tables				
Table 3.1	List of commonly used inorganic EC materials	53		
Table 4.1	Comparison table showing the performance of	84		
	various ECDs containing Co <sub>3</sub> O <sub>4</sub> .			
<b>Table 4.2</b>	Comparison of reported device with known	92		
	inorganic devices containing PB or Co <sub>3</sub> O <sub>4</sub> .			
Table 6.1	Details of linear porosity as a function of precursor	121		
	concentration.			
Table 6.2	Details of parameters calculated by Image J	122		
	software.			
Table 6.3	Summary of FE parameters and obtained master	132		
	fitting parameters along with boost factor and			
	effective work function for NiO NPs and TNRs			



#### **Abbreviations**

Ethyl Viologen EV Nanostructurs NSs Nanopetals **NPs Optical Density** OD Color Contrast ratio CCr Linear Sweep Voltammetry LSV Poly Ethylene Oxide **PEO** Indian doped Tin Oxide ITO Carbon Cloth CCFluorine doped Tin Oxide FTO X-ray diffraction **XRD** Commission Internationale de l'Eclairge CIE Scanning Electron Microscope **SEM** Transmission Electron Microscopy **TEM** X-ray Photoemission Spectroscopy **XPS** Energy Dispersive X-ray EDX **Atomic Force Microscopy AFM** Diffused Reflectance Spectroscopy **DRS** CV Cyclic Voltammetry Brunauer-Emmett-Teller **BET** Fast Fourier Transform **FFT** Electrochromic Devices **ECD** 

Ultra-Violet Visible Spectroscopy UV-Vis

Working Electrode WE

Counter Electrode CE

Reference Electrode RE

Electrochromic EC

Surface to Volume S/V

Quantum Confinement Effect QCE

Charge Coupled Device CCD

EC Double Layer EDL

Transition Metal Oxide TMO

Co-ordination Network Compound CNC

Selective Area Electron Diffraction SAED

Intervalence Charge Transfer IVCT

Field Emission FE

TiO<sub>2</sub> Nanorod TNR

# **Chapter 1**

# Introduction

The commonly used term "ultrafine particles" can be defined in the scientific domain by the term "nanoparticles", one of the terms currently being widely used in research and technology. Looking at a broader picture, finding new materials and reengineering the existing ones are the need of the moment. With the advent of nanotechnology in material science, various new properties can be observed from same compound by simply controlling the size when miniaturized to the nanoscale. Nanoscience has the potential to reshape the world around us. It could lead to revolutionary breakthroughs in fields ranging from manufacturing to health care. The unique physical and chemical properties of nanomaterials also often differ from those of bulk materials and require special assessment. Nanoscience is one the thrust area that may contribute in making India a developed country by year 2022.

# 1.1 A preliminary discussion

In the modern science and technology, a new field, nanoscience, has played an important role in the overall development towards addressing several challenging problems related to society[1,2]. Nanoscience and nanotechnology refer to the science and technology of matter, manipulated at atomic level. Nanoscience is a compound word having two parts, nano and science[3]. Although nano is a prefix as in nanometer, nanoampere, nanosecond etc. referring to 10<sup>-9</sup>, in nanoscience. In this size regime, matter exhibit unusual properties which makes this science unique. The variation of properties as a function of size occur in different materials differently[4]. While properties of materials at nanoscale are distinctly different from the bulk, the act of measurement of length at the nanometer does not offer any new phenomenon. Several aspects have to be clarified in order to proceed further. The dimension refers to the characteristics dimensions and not to the length scale of the piece of matter under investigation along all axes[5,6].

The fabrication of nanomaterials mainly possesses the synthesis process and is categorized in two approaches namely top-down and bottom-up approach[7]. The fundamental difference between these two processes to synthesis the nanomaterial is that the top-down process lead to crystalline sample (single crystal or polycrystalline material) which forms the ideal crystal structure of material whereas the bottom-up approach results the formation of small particles from crystalline areas that do not correspond to ideal lattice which contains the defect structure. This thesis comprises to the synthesis work nanomaterials through bottom-up approach in which the material gets transform into nanoscale via recrystallization route and also form molecular structure resulting in cluster[8,9]. Therefore, it is important to notice that the bottom-up approach may lead to the formation of both defective crystalline structures and molecular clusters in the 'nano' regime. Figure 1.1 is showing the different nanostructures prepared from the different materials mentioned in the respective images through the bottom-up approach. The formation of nanomaterial' are also further categorised based on their quantisation of dimension for their different practical applications with keeping the two imperative properties namely high surface to volume (S/V) ratio and quantum confinement effect (QCE) which highly affects the electronic as well as optical properties.

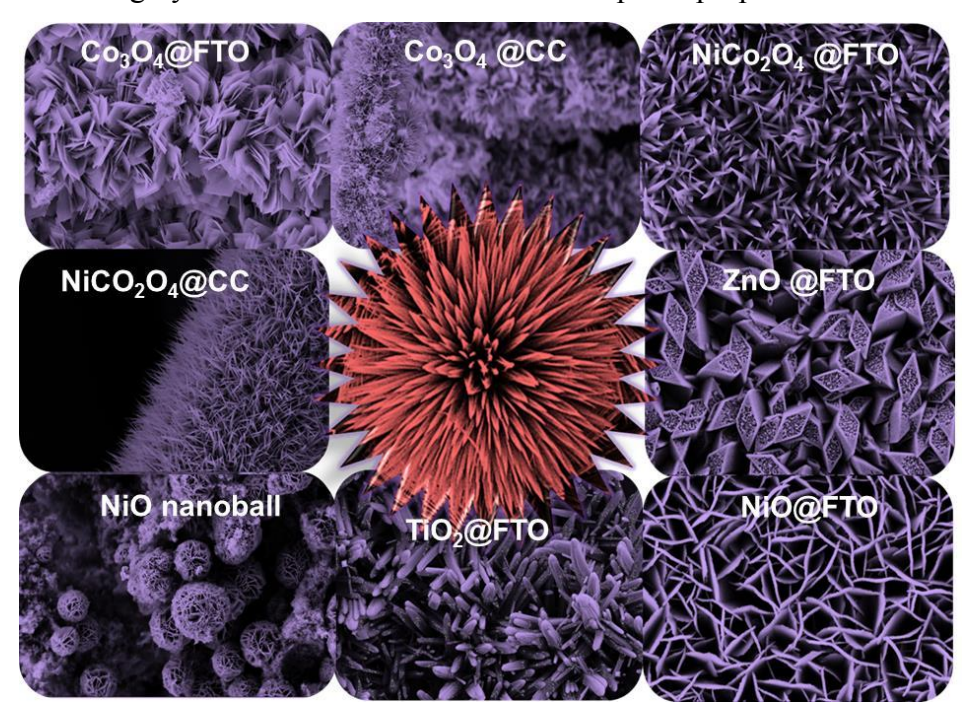


Figure 1.1: Electron micrographs of a few nanomaterials.

#### Surface to Volume ratio::

One of the main features of materials at the nanoscale is the increase in their surface area[10]. The nano forms of material have larger surface area in comparison with the same volume of material in bulk form. As the size of material decreases, S/V ratio increases and shows much higher effect at the nano scale dimension and thus, leads to the nanoparticles being more chemically reactive. Being the acquisition of higher surface area, larger active sites are present in the volume of material to initiate the chemical reaction more speedily and hence the rate of reaction increases.

#### **Quantum confinement effect::**

Nanomaterials' synthesis covers a new science of quantum physics at nanoscale in terms of QCE[11]. It can be expected that the size of the nanostructures in the limit of Bohr exciton diameter lead to the QCE.

The system experience QCE when the diameter of the particle lies in the magnitude of the wavelength of electron wave function and at this condition, optical and electronic property of material get substantially deviated from the bulk materials. The decrease in the confinement dimension up to the nanoscale dimension creates the discretisation of energy level, result in increase of the band gap of material. Therefore, the QCE may lead to affect the electronic and optical properties of material by varying the size and shape of nanomaterials'. These variations at the limit of Bohr exciton radius are sufficient to tune the materials' application broadly. Thus, the nanomaterials' can be taken in the different perspective of application in the domain of physical science, chemical science, biomedical and engineering science for device designing[12].

# 1.2 Nanotechnology in various fields

Nanotechnology, the technology that emerge as a result of nanomaterials, is helping to considerably improve, even revolutionize, many technology and industry sectors, information technology, homeland security, medicine, transportation, energy, food safety, and environmental science, among many others. Emerging application in nanoscience, i.e. nanotechnology, has spread in almost all branches of science with keeping the two basic properties. Thousands of innovative application reflects directly form the various nanostructure in different aspects. Both materials (say inorganic and organic) transform into its nanostructure form and make the well-defined platform to combine the science and engineering together. The various fields are covered from the verity of nanostructures of different materials that some glimpses of which are summarised here briefly in different scientific branch.

#### 1.2.1 Chemical Science

Nanoscience plays an important role in various aspects of chemical science as seen in various applications related to it. Varieties of applications are emerging out in the field of chemical science because of the advent of nanomaterials. The ground work of nanotechnology in

chemical science is to understand by purifying the drinking water using the nanopores thin film of molybdenum disulphide which purifies the water approx. five times better than the conventional filters. One of the most important applications is in sensors that use various chemicals like carbon nanotubes[13,14], zinc oxide[15–18], palladium[19–22], gold nanoparticles[23] and many others[24]. They possess sensing properties in one form or the other. These detecting molecules change their electrical properties such as resistance or capacitance when they are used for sensing applications. Hydrogen sensors are also using a layer of closely spaced palladium nanoparticles that are formed by a beading action like water on a windshield. When hydrogen is absorbed, the palladium nanoparticles swell causing shorts between nanoparticles which lowers the resistance of the palladium layer. Sensors using a layer of gold nanoparticles on a polymer film are made for detecting volatile organic compounds. The polymer swells in the presence of volatile organic compounds, changing the spacing between the gold nanoparticles and thus the resistance of the gold layer. To remove oil form water, researchers have developed magnetic water repellent nanoparticles and used magnets to mechanically remove oil from water in oil spills[25-27]. These are only a few examples to underline the importance of nano-science and -technology in the field of chemical science.

#### 1.2.2 Physical Science

Nanoscience plays an important role in the field of Physical Science to observe and explain many physical phenomena that were not observable in bulk materials. One of the important physical phenomena is non radiative transition and for the same Raman spectroscopy has proven to be a handy technique[28]. Raman spectroscopy has been often used to detect the non-radiative transition from silicon nanostructures. Different unique properties in nanomaterials are observed due to their quantum confinement effect, a special effect that does not occur in their bulk counterpart[29]. Various optical, electronic and electrical properties of nanomaterials can be easily understood with

the concept of quantum confinement, an effect that shows size dependent properties on reaching quantum or nano dimensions. Confinement effect modifies energy levels to change to discrete energy bands when material dimensions become in nanometer range[30–32]. Electrons, holes, phonons and other bound states entities confined inside nano dimensional materials starts giving rise to amazing properties leading to various applications in laser, diode, photovoltaics etc. These applications are possible only due to the fusion of nanoscience in physical science.

#### **1.2.3** Biological Science

Nanoscience has given a new perspective in the field of Biological Science ranging from diagnosis to treatment[33]. Nanoscience is proven to be very effective tool in understanding fundamental life processes with the development of probe that are capable to do so. As we look at life forms in smaller and smaller dimensions, we end up with biological objects which are involved in fundamental life processes. The key molecule in biology such as DNA, enzymes, receptors, antigens, antibodies and oxygen carriers can be included in the dimension of nanometers. Thus it is clear that all fundamental processes of biology are taking place at nano level. The science of nanobiology has progressed significantly and can be branched into several disciplines of life science such as cellular biology, genomics, proteomics, immunology, diagnosis, targeted drug delivery etc[34]. The idea of creating hybrid systems of inorganic nanoparticles with biological moieties emerged out to be a new method to overcome many difficulties in medicines and biosciences. Using nanomaterials, instead of conventional materials, in biological science has increased efficiency while decreasing cost. Thus the hybridization of nanobiotechnologies has laid the foundation for many novel methodologies, which are capable of solving several technical difficulties in bioscience. The idea and innovations of nanobiology can be extended to broadly four categories as follows: interaction between biomolecules and nanoparticle surfaces, biological imaging using nanoparticles,

analytical applications of nanobiology, medical diagnosis and targeted drug delivery and biosynthesis of nanomaterials[35–39].

# **1.2.4 Engineering Science**

A rise in research areas with societal impact has been observed with nanoscience and nanotechnology being one such area especially where nano devices are in focus. After preparing the material for variety of applications, is again much important to apply the engineering on it to fabricate the electronic devices for commercializing application. The electronic devices in all sectors of science are found in flexible, bendable, rollable and stretchable types in integrated devices[40–43]. Such modifications in the device engineering make it more useful in daily life applications like in gadgets, healthcare, aerospace, security and defence with making the devices more flexible, lightweight, non-brittle, more stable. Various other efficient materials (2D nanomaterial) like graphene, MXenes also works as improving the performance of the electronic devices for respective applications[44]. The various engineering of electronic devices comes into picture for various applications like in memory, energy storages, sensing, photovoltaic, solar cells and electrochromic etc[43–46].

Nowadays, electrochromic devices (ECD), a device that changes its optical properties under the influence of an electrical bias, have also found their potential application in electronics and especially in display systems. Current work focuses on such ECDs, which are capable of showing optical modulation under external applied electrical. The material's nanostructure having higher surface area also plays crucial role toward improving the performance and helps to understand the role of nanostructures in device geometry. Apart from the EC device, various others nanostructures have been fabricated for the Field Emission (FE) display, Glucose Sensing, Supercapacitor like applications of engineering application, which will be discussed in later chapters. The future goal of the nanotechnology must be gone through the multifunctional application with the device geometry shows flexible nature, long term stability, low operating voltage etc.

### 1.3 Electrochromic

As the name suggest the word "electrochromic" means the effect of chromism (i.e. color change) perceived in some material by the electric means either due to the effect of voltage or current and the materials' are called electrochromic active material [47,48]. Thus, the electrochromic (EC) phenomenon is a chromic modulation of material characteristics in the visible wavelength range, which can be easily seen by the necked eye and observe either in reflection, transmission and absorption mode[49,50]. The chromic modulation between two or multi color state is a reversible process and is observed due to the reversible redox activity of material under the external bias. Recent research related to electrochromism is being carried out with a focus on fabricating various materials for EC devices for less energy consumption and found in much commercial applications like in smart windows, antiglare mirrors, optoelectronics and paper like display system which has been shown in Figure 1.2 and EC materials are also being applied for protecting the confidential meeting as works like an opaque window at the meeting time only[51,52]. The image in Figure 1.2e is a real picture of meeting room in Microsoft office. Different color appearance of material should always be a main part to understand the mechanism of every ECDs (or electrode)[53-56].

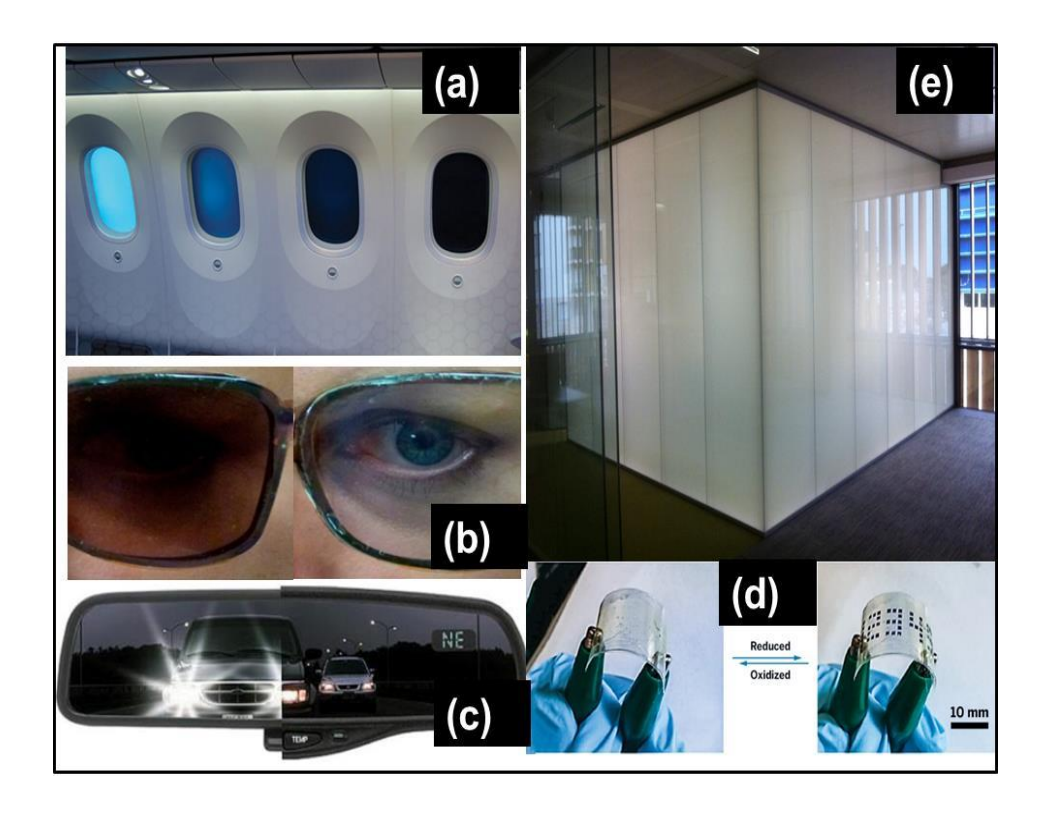


Figure 1.2: Application of electrochromism in (a) aircraft window, (b) specs, (c) car's rear-view mirrors, (d) flexible digital displays and (e) meeting room at Microsoft head office[57].

# 1.3.1 Appearance of Colour

The appearance of the colour can be simply understood by capturing the respective colour wavelength at eye which is coming from the object via reflection or transmission and the sensitivity of eye works nonlinearly with the different wavelength. The absorption of certain wavelength by the material is allowed to transmit or reflect the remaining wavelength in visible spectrum, lead to perceive the overall colour. A colour-wheel is shown here to bring the idea of complementary colour system which is seen by absorbing the intense maximum colour wavelength. Different wavelengths have also been written in respect of given colour and appears one colour by absorbing the opposite (or complementary) wavelength (or colour) intensely. For example, the intense blue color (450 nm-480 nm) of device will appear on absorbing the maximum orange wavelength (600 nm-640 nm) colour but the practical ECDs does not show the intense absorbing wavelength[58]. Colours which perceive

as brilliant and bright have strong narrow absorption band whereas dull colour appearance tends to have the weaker and broader absorption band. The absorption of the different wavelengths (more than two) also leads to perceive the other colour. For example, the Green colour is a result of absorbing the Red and Blue colour simultaneously. Therefore, it can also be understand that Red, Green and Blue color are the complementary color of each other and one appear on absorbing the others[59]. The combination of wavelength coming out of the sample decides the colour of material. The concept of additive primary colors (RGB- Red, green, blue) and subtractive primary color (CMY- Cyan, magenta, yellow) is also used to correlate the color combination in different EC material.

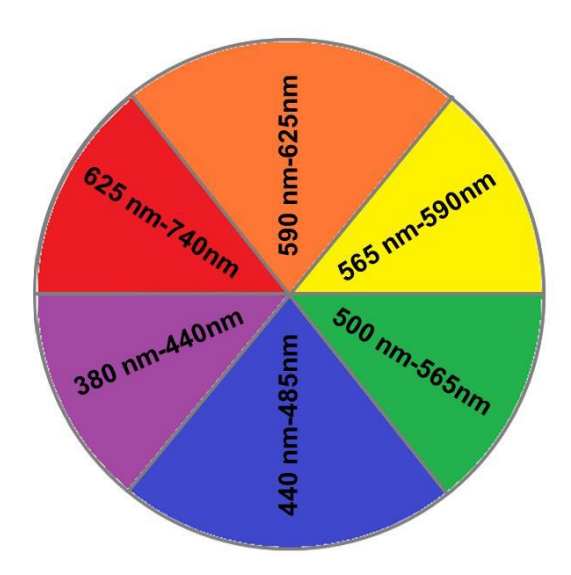


Figure 1.3: Color wheel to check the appearance definite colour with absorbance of others.

## 1.3.2 Type of electrochromic material

Every EC active material exhibit a new optical absorption band with showing the new color state in which the electron transfer mechanism occurs due to reduction (gain of e<sup>-</sup>) or oxidation (loss of e<sup>-</sup>) from the material are known to be n-type and p-type EC material respectively. The complete information of both types of materials must be needed separately to make the solid state device assembly, in which both materials can play as an auxiliary material to allow the redox reaction

very fast. Materials have been characterised into two family 'cathodic' and 'anodic' EC active species based upon their redox polarity of material towards electrochromic property in both organic and inorganic family of materials.

#### 1.3.2.1 Inorganic Electrochromic compounds

The inorganic metal oxide generally shows the intense optical absorption due to the effect of intervalence charge transfer (IVCT) in which electron is excited to a similar or vacant orbital on an adjacent ion or molecule [60,61]. In case of the well-known material tungsten oxide (i.e. WO<sub>3</sub>) shows its pale yellow in colour before electro-reduction process because all the tungsten sites exhibit oxidation states of +VI. Under the negative external biasing, all the W(VI) (reduction) sites from the WO<sub>3</sub> forms W(V) centres and produces the blue color of electrochrome. The partial reduction of WO<sub>3</sub> introduces the fractional amount of negative charge to compensate the charge by the cation insertion (say H<sup>+</sup>) to form the  $H_x W^V_x W^{VI}_{(1-x)} O_3$ . Therefore, the centre W(V) is responsible to generate a photo-effected intervalence charge transfer between the two oxidation site of WO<sub>3</sub>[62,63]. Such intervalence charge transfer is probed by the optical absorption spectroscopy in the UV, visible or near IR regions and can be taken for concluding the chromic modulation in inorganic materials. The intense or broader band optical absorption spectra during the color changing state is a consequence of color appearance of the material with single or mixed wavelength color respectively. The material should be in thin film over the transparent conducting substrate to shows its better chromic modulation for which many synthesis methods are been taken like hydrothermal method, spin coating, electrodeposition, physical (or chemical) vapour deposition, sputtering etc. All of these methods are suitable to prepare thin film of all inorganic (say transition metal oxide) materials in which the electrochromic property is greatly depend on varying the thickness, surface morphology, binding of material to the substrate and appropriate transmission for visible light. These parameters greatly influence the EC behaviour of material and thus changes to the color appearance.

Out of many cathodic or anodic transition metal inorganic EC active oxides, cobalt oxide, Prussian blue and spinel Ni-Co composite material have been chosen for most of the thesis work with taking an initial step for depositing the material using electrodeposition techniques and thus works as a single or double layer hybrid EC device very efficiently, which will be discussed later on.

#### 1.3.2.2 Organic Electrochromic compounds

The other family of EC active material brings the organic molecules which are widely used in the molecular electronics for various applications[63]. The organic material also known for its easy fabrication mechanism through spin coating, drop casting, spray pyrolysis etc. and its breakthrough in flexible light weight electronic devices opens many possibilities in today's modern era. Simultaneous achievements have also been captured from the invention of conducting polymers of thiophene, pyrrole, aniline, and their derivatives into various fields because their p-conjugated electronic structure can be change due to the electrochemical doping which lead to change in band gap and optical contrast of the material [64,65]. All these conducting polymers are widely accepted in the electronic media due to their suitable band gaps and low operating redox potential. The same cathodic and anodic characterisation of EC active material has been applied in organic material, in which polythiophene comes in the category of anodic group. The EC active thiophhene changes its color from natural reddish to perfect transparent to light blue color during the positive scan of voltage under the mechanism of polron and bipoloron species in the thiophene polymer. The same procedure of chromic modulation with different mechanism is allowed for all kind of conductive polymers which shows the optical modulation under the redox reaction.

The non-polymeric EC active materials are also plenty in number in which viologen is one in a class of 4,4 bipyridine compounds exhibits EC property under the reversible redox reaction between the redox state of  $EV^{+2}$  and  $EV^{+}$ . Viologen shows its chromism under the negative bias and hence falls in the category of cathodic EC material. The natural state of viologen in  $EV^{+2}$  appears in transparent color and transform into the

blue state under the negative bias due to the creation of radical EV<sup>+</sup>. ion[58]. Both the chromic states of viologen are found reversible and appear clearly in two color states. This thesis work contains the viologen organic compounds sandwiched with inorganic cobalt oxide to improve the whole EC device performances, which will be discussed later on.

#### 1.3.2.3 Herbal Electrochromic compounds

A new EC material branch has opened just only through the observation from the daily natures and mankind routine, and found that a raw herbal precursor changes its colour due to chemically induced or oxidised. Recently, many researchers are working on taking the extract form the various flowers (say hibiscus) and used to make the EC device[66]. The recent breakthrough in the field of EC material activates the human thinking towards nature's gift.

## 1.3.3 Electrochemistry of EC material

The electrochemistry setup is designed to known the redox activity of the material under the application of external potential[67]. Out of the many measurement, Cyclic Voltammetry (CV) is one the elementary and vital measurement techniques for knowing the idea of material characteristics toward either faradic or capacitive redox reaction which is allowed inside the electrochemical bath[68]. The Electrochemistry not only used for EC application but also applicable as initial characterisation for supercapacitor, sensing, I-V characteristics etc. There a three electrode system is chosen to measure only the materials characteristics, whose different components have been described here briefly.

**Working Electrode (WE):** The material deposited over the conducting transparent Fluorine doped tin oxide (FTO) (Resistivity < 9 ohm-cm) and Indium doped tin Oxide (ITO) (Resistivity 35-40 ohm-cm) coated glass substrate is usually taken as a WE at which the external biasing of voltage or current is applied.

**Reference Electrode (WE):** The Ag/AgCl (or Hg/HgCl) RE generally used in CV experiment and external potential is applied across the reference and working electrode.

**Counter Electrode (CE):** The importance of the CE is to sense the amount of charge extract/inject to the working electrode in terms of current. The current response is taken across the working and counter electrode with respect to each and every applied external potential.

Thus, the observed current response with respect to voltage give the idea of oxidation and reduction of material with releasing an extra hump in the CV profile and the area under the curve also clarifies the amount of charges stored by the materials which can be used to draw the capacitive and faradic nature of material.

#### 1.3.4 Electrochromic device fabrication

After fabricating different redox EC active materials including inorganic, organic, herbal, it is equally much indispensable to fabricate these single material electrode into the device geometry. The device should be in a way that meets all the criteria of commercial purpose. The EC device mainly contains the two electrode system which covers the material and electrolyte both. The EC active material deposited over one transparent FTO/ITO electrode and combined with other bare electrode with inserting the electrolyte between them, is known as single EC active device. The electrolyte is usually taken in the gel (e.g. non conducting polyethylene oxide (PEO)) form in which gel provides a matrix to keep the electrolyte ions mobile. In the double layer device, both the electrode must be coated with EC active material and are combined in device geometry with following the same steps. Therefore in order to fabricate the double layer device it must be noted down that, both the material should be complementary redox active to make the device in active state in each polarity. The fabricated devices in this cross bar geometry, shown Figure 1.4, can be taken for measuring the performance in terms of different parameter which makes this EC device suitable for EC smart window in aircraft, protecting shield, rear view mirror based on their properties and performances.

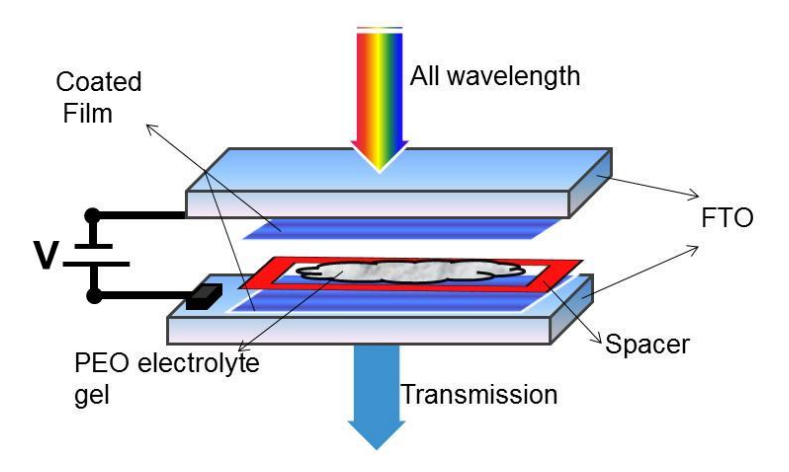


Figure 1.4: Schematic electrochromic device representation.

#### 1.3.5 Electrochromic Device Performance

The device performance is checked using the simultaneous measurement of in-situ optical spectroscopy and chronoamperometric measurement. Both the combined measurement tells the idea about the optical modulation with respect to the amount of charge transfer and can be calculated in different term, which are being described here.

#### 1.3.5.1 Color Contrast ratio (CCr)

The visible optical changes during the chromic modulation of device can be measured mathematically in terms of Color Contrast ratio (CCr). It is measured, when in-situ optical spectroscopy in transmission mode acts on the device/electrode, during colour change operation, at particular wavelength. The net change in the transmission spectra at a particular wavelength during the switching between two chromic states is measured by using the given formula in Eq. 1.1 which directly gives the result of CCr. Higher the CCr means easy to distinguish different colour of device.

$$CCr = \frac{T_f - T_i}{T_i} X 100 , \qquad (1.1)$$

Where,  $T_f$  and  $T_i$  are the transmission of final and initial state during optical changes. The initial state of device means there is no external bias applied to device and device remains its natural color whereas, final state represents the coloured state device under the given potential. The same terminology is also true for absorption spectra in Eq. 1.2 with a

little change in the above Eq., is given below, to calculate the CCr at a particular wavelength.

$$CCr = \frac{A_i - A_f}{A_i} X100 \tag{1.2}$$

where,  $A_i$  and  $A_f$  are absorbance values in initial and final states respectively of the device/electrode.

#### 1.3.5.2 Optical Density

The change in the optical property at a given wavelength leads to change the Optical Density (OD) of the material and therefore is described directly in terms of absorbance and logarithmic of inverse of transmission, is being described using Eq. 1.3.

$$OD = A = log (1/T)$$
 (1.3)

#### 1.3.5.3 Switching time

Switching time is one the vital parameter to measure the real life application of the device. Switching from the one coloured state to another (or bleached state) under the application of external biasing must take less time for calling it a good EC device and thus defined as the net optical change (either in absorption or transmission) should be differ in 90 % between the two colour states at a fix wavelength. The switching is calculated for ON state (say; bleached to coloured state) and OFF state (say; coloured to bleached state) for every device to know the performance of ECD under the given potential. The switch time is also depended upon the thickness of material, electrolyte used, composition of material, conductivity of sample and thus can be calibrated using these parameters.

#### 1.3.5.4 Coloration efficiency ( $\eta_{ec}$ )

The coloration efficiency ( $\eta_{ec}$ ) calculation is main key parameter to know the whole behaviour of EC device using a single parameter. The  $\eta_{ec}$  is defined as the ratio of change in optical density between coloured and bleached state to the charge injected or extracted per unit area of the working electrode at given wavelength and is defined by using Eq. (1.4)

$$\eta_{ec} = \frac{\Delta OD}{Q} \tag{1.4}$$

Where  $\Delta OD = A_i - A_f$ ; is the change in the absorbance value of two different coloured state at initial and final response of EC device and Q is measure of charge density during the switching mechanism of device. The slope of  $\Delta OD$  and Q in respective graph gives the coloration efficiency value and higher the  $\eta ec$  value brings the device more appropriate to be commercial utilization.

#### 1.3.5.5 Stability of Device

To quantify the stability of EC device after calculating the relevant parameter is also much indispensable to check the life of device with keeping the same performance. Many hindrances from the preparation of electrode to the device fabrication in atmospheric conditions can disturb the stability of device for long time, therefore little change in current response and in optical switching variation hints about the stability of device. Thus, every ECD's are investigated by using these steps and can be capable to go for commercial use in various fields.

# 1.4 Multifunction application of Electrochromic materials

The electrochromic material initially is tested using the electrochemistry measurement which tells about the basic features and property of material towards chromic modulation as discussed in previous section 1.3. Different materials can also possess different applications with carrying the EC application and known for its multifunctional applications, are being briefly discussed below. With the incorporation of nanomaterial, much properties enhances greatly toward the various electrochemistry application.

# 1.4.1 Electrochromic memory

The electrochromic material generally possesses at least two color state during the switching response of the device, can be taken as the one memory bit for each color state in an optical memory. This is possible if a given colour (thus the redox state) can be retained after removing the external bias or in open circuit condition[69,70]. Though

technically possible to realize, fabricating a memory bit with desired speed remains a challenge. Another limitation with such memory devices is its small integration density on a single chip

#### 1.4.2 Energy Storage and Sensing

The EC material shows their chromic modulation under the effect of charge intercalation or de-intercalation at the surface of working electrode which therefore, can bring the property to store the charge makes the EC device appropriate for energy storage (or supercapacitor) application too[46,71]. Many transition metal oxides show their multiple oxidation states, which opens a possibility to store the charge in these different oxidation state in the respective material and can also be used as energy storage material. The nanomaterials surface architecture improves such kind of applications greatly where the larger surface area is needed. The chrono-amperometeric response of EC device, where the amount of charge is required for perceiving the chromic modulation, also suggests the charge storing property of the device. Similarly, a linear response of CV graph of the material with respect to scan rate reveals the capacitive nature of material and can also be applicable for the sensing application[72].

## 1.4.3 Heat Shielding

Since the electrochromism of material is totally dependent upon the optical modulation in which the change in absorbance (or transmission) value for the respective wavelength decides the resultant color appearance. If an EC device shows higher absorbance in IR region compared to visible it can be used for heat shield application. Because, a large part of solar radiation is known to be composed of near infrared (IR) radiation, responsible for heating, precisely filtering which may help in utilizing the rest of the cool light without worrying about the heat[73,74]. Specially designed ECDs may prove to be a good option for such a role in addressing the aforesaid problem as these devices are known for modulating their optical properties (transmission, absorption, etc.) on application of electrical bias. Many Inorganic (e.g.WO<sub>3</sub>) and

organic (e.g. P3HT) like material separately and combinedly shows EC heat shielding application with a greater performance.

#### 1.5 Electron Field Emission

Emission of electrons under an applied bias, or the FE is a quantum tunnelling process which highly depends upon the conductivity of material, materials' surface architecture and the nature of electric field[75-83]. This remained an area restricted to the scientific exploration until efficient FE was observed from nanomaterials especially carbon nanotubes. This was followed by various metallic, semiconducting and even insulating nanomaterials for exploration of FE properties for real application in display devices which is yet to become a reality. Though nanostructures of carbon still remain the best field emitter but delay in delivering an actual device opens a scope for searching second line new materials for this purpose. Other nanomaterials have been investigated to enhance the FE by addressing the shortcomings by designing appropriate materials[84–86]. Reasons behind being a poor field emitter include uneven alignment of the nanorods, and too close packing of these nanorods[87]. The uneven alignment does not allow all the rods to experience equal field thus requiring higher fields for participation of all rods whereas the screening effect kills the FE in the latter case. Thus, nanomaterials with high aspect ratio, thinner diameter, sharp edges and well alignment perpendicular to the substrate are expected to be good field emitters for its potential application in microwave devices, X-ray source etc. To improve or to explore the FE application in much electronic devices and for material characterisation tool, invention of new nanomaterials in 1D and 2D geometry are being enthusiastically going in the field of nanotechnology. Beyond the application purpose, it is also much necessary to understand the basic science behind the electron transport mechanism from material to vacuum under the external applied which is completely based on the quantum mechanics.

# 1.5.1 Experimental and quantum mechanical approach

To obtain a measurable current density for device application, appropriate voltage is needed which can be applied in parallel plate geometry as shown schematically in Figure 1.5a along with photograph of actual experimental set-up in Figure 1.5b. Emission of electron from the material's surface may get enhanced by producing the high vacuum and selection of conductive two electrode system after manufacturing the well-established setup for FE, shown in Figure 1.5b inset. Since, Nanostructure based material deposited over conducting FTO (or Silicon substrate), work as cathode plate interfacing with vacuum level builds some individual potential distribution which depends upon the effect of external potential and induced image charge effect. To explain Figure 1.5c in a better way, Necessary information should be conveyed through physical Eq.s. Since, the potential distribution varies with distance linearly throughout the two electrodes under the application of external biasing, which is shown by blue dotted line, called applied potential. On the other hand, image charge potential develops (shown by green dotted line) at the junction of material's surface and vacuum when the electron gets the condition to just leave out from the material and feels a finite force begins to pull this electron by instantly generated force by the material. Since this force is much significant only for smaller distance and gradually tends to saturate with greater distance and completely goes off for higher distance. Thus, Resultant potential profile will be the algebraic summation of these two instantaneously developed potentials, is being representing in Eq. 1.5, and makes the rounded edge triangular barrier potential, through which the electron will tunnel, shown by red bold line in Figure 1.5c[88–90].

This potential profile is named as schottky potential and the work function corresponding to this potential is representing in Eq. 1.5.

$$\phi_{\text{schottky}} = Ex + \frac{e}{16\pi\epsilon_0 x} \tag{1.5}$$

The first term (in RHS) represents to the applied potential and the other one (in RHS) is for the image charge effect. After generating this

potential at the interface of material and vacuum, effective work function and corresponding energy gets depressed from its bulk value, presenting by mathematical Eq. 1.6 &1.7.

$$\phi_{\text{effective}} = \phi_{\text{material}} - \phi_{\text{schottky}}$$
(1.6)

$$e\phi_{effective} = e\phi_{material} - eEx - \frac{e^2}{16\pi\epsilon_0 x}$$
 (1.7)

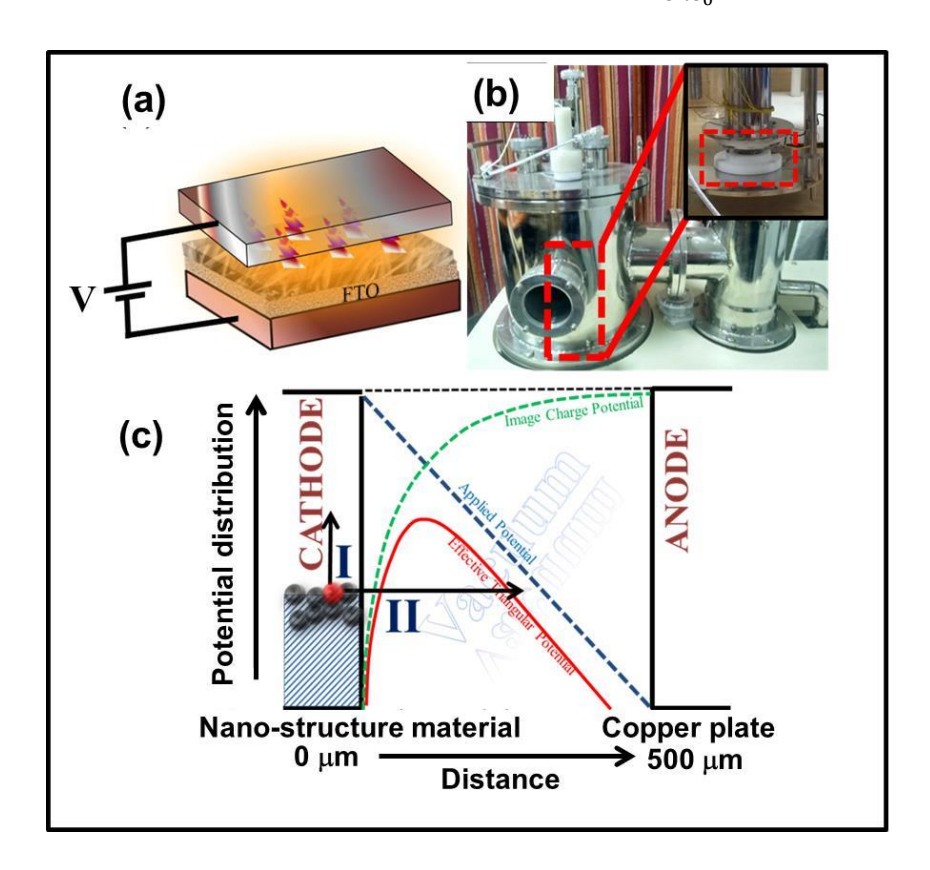


Figure 1.5: (a) Schematic representation of arrangement for electron emission measurement from nanostructure material, (b) actual photograph of field emission measurement setup and the two electrode arrangement made of copper (inset), (c) distribution profile of potential as a function of distance from the nano-structure showing image charge potential (green dotted line), applied potential (blue dotted line) and effective rounded edge triangular barrier (red bold line).

Eq.1.6 is representing the effective work function profile and Eq.1.7 is just conversion in energy format of Eq.1.6 by multiplying by charge of electron. Hence, there comes the advantage in field emission phenomenon after getting the new potential profile. Since, this potential

is providing the less effective height as well as less effective tunneling width; therefore, it has some chance of jumping the electron through path I and tunneling the electron through path II, as mentioned in Figure 1.5c. Hence, the experimentally obtained current profile might be due to the effect of these two processes, which has been described in detail in chapter 6.

#### 1.5.2 Fowler-Nordheim Framework

Field emission display is an important application and works by exploiting electron emission from (nano-) materials through tunneling, a quantum mechanical phenomenon, which highly depend on geometry and microstructures of nanomaterial used. As mentioned above, for optimal use of a nanomaterial, its inherent properties should be known for which an appropriate analytical framework must be laid and used after due validation. For analysis of the FE properties an existing methodology is being used which is based on a modified version of the one proposed by Fowler & Nordheim in the form of an equation commonly known as F–N equation. Fowler & Nordheim has predicted a theory of FE from metallic and semi-metallic nanostructures and devised following Eq. to quantify relationship with the current density (J) and electric field (E):

$$J = A\emptyset^{-1}\beta^{2}E^{2}e^{\frac{-B\emptyset^{\frac{3}{2}}}{\beta E}}$$
 (1.8)

where, A (=  $1.54 \times 10^{-6} \text{ AeV/V}^2$ ) & B (=  $6.83 \times 106 \text{ eV}^{-3/2} \text{ V/mm}$ ) are temperature independent structural parameters and  $\beta$  is field enhancement factor. This F–N equation enables one to find out the quality of FE by defining a "field enhancement factor ( $\beta$ )" calculated from the experimentally observed current density/-electric field curve or J-E curve. For doing so, the F–N equation is modified to be represented as a straight line (with reciprocal of electric field as independent variable) whose slope gives the measure of this factor  $\beta$ . The F-N equation (Eq. 1.9), can be rewritten as following Eq. 1.8 to be

represented as a straight line to obtain the enhancement factor and threshold field:

$$\ln\left(\frac{J}{E^2}\right) = -\frac{B\emptyset^{3/2}}{\beta E} + \ln\left(\frac{A\beta^2}{\emptyset}\right) \tag{1.9}$$

Eq. 1.9 clearly represents a straight line between  $\ln (J/E^2)$  & 1/E. The negative slope and the intercept give measure of enhancement factor ( $\beta$ ) and threshold field respectively. This factor  $\beta$  is the factor by which the applied electric field gets enhanced thus facilitating the tunneling of electrons across the barrier defined by the barrier height and width defined by the work function and the size of the crystallite. It is commonly understood that higher the factor, higher are the chances of tunneling thus that of the FE. Therefore, every nanomaterials are investigated for their good scope of FE current, will be checked using these different parameters, in which turn-on voltage and threshold field value should be low while the field enhancement factor should be quite high.

# 1.6 Objectives

#### Main objectives of the presented work are as follows

- Designing different nanostructures with appropriate techniques.
- To understand electrochemistry on solid state thin film of nanomaterial to know the redox behavior of material for different applications.
- To use redox activity of electrochromic material to explore device designing by taking two complementary electrode of opposite polarity to improve the overall performance.
- To use electrochemically deposited electrode in fabrication of solid state electrochromic device and explore the possibility of an "all-inorganic" electrochromic device.
- To fabricate inorganic-organic solid state electrochromic device to improve device performance.

- Multifunction application of nanomaterial showing two applications in electrochromic and glucose sensing.
- To study field emission properties of nanomaterials' thin film with developing of a new framework for its analysis.

# 1.7 Organisation of thesis

Above-mentioned studies (detailed results and discussion with experimental methodologies) have been compiled in the thesis by adopting the following chapter-wise plan:

- Chapter 1 (Current chapter): Gives the introduction of the relevant topics related to the thesis work and defines the objectives of the thesis.
- Chapter 2: Deals with the details of experimental methodology used for the experimental work carried out along with details of various experimental parameters. It also summarizes details of various equipment's models used for characterization.
- Chapter 3: It presents the work related to the fabrication and characterization of inorganic transition metal oxides and their electrochemistry to show their electrochromic performances. Utilization of material for other applications has been suggested in this chapter with detailed study and mechanism.
- Chapter 4: It deals with the electrochromic layered display of inorganic/organic and all-inorganic material and their improved performances over the single layered isolated electrochromic display.
- Chapter 5: It describes a fabrication of binary nano composite of Ni and Co for improving the electrochromic performance and its bifunctional role for Glucose sensing application
- **Chapter 6:** Field emission properties of nanomaterials oxide and its analysis within the known framework have been described in

- this chapter. It also explains a new model to understand the FE properties and compared with the existing mothed.
- Chapter 7: It lists all the conclusions drawn based on research work reported above. This also includes future scope of works that may be carried out to enhance the understanding in the field and to fabricate electrochromic devices with other multifunctional role for commercial applications.

# Chapter 2

# **Experimental Details**

This chapter, divided into two different parts (sample preparation and measurements), sums up the methodology used for fabrication of (nanomaterials, electrodes, devices etc.) and various experiments done for characterization and applications. Various nanomaterials, in powder and thin film forms, have been prepared using a bottom-up approach via different techniques to achieve the desired architecture of nanostructures. The prepared samples have been characterized using diffraction, microscopy and spectroscopy using Xray Diffraction (XRD), X-ray photoelectron spectroscopy (XPS), Scanning electron microscopy (SEM), Atomic Force Microscopy (AFM), Transmission Electron Microscopy (TEM), Raman Ultraviolet-Visible spectroscopy (UV-Vis), spectroscopy, etc., Additionally, in-situ optical and Raman studies have also been performed for electrochemical study. Information of electrochemistry using the different technique like CV, chronoamperometry and impedance spectroscopy have been briefly introduced here including the details of the used machines.

# 2.1 Material synthesis process

Nanomaterials are synthesise using two different approaches, Top down and bottom-up[91–100]. In the first one, the nanostructures are prepared by decreasing the size of material starting from its bulk counterpart and in the latter nanostructures are grown to a desired size starting from the smallest constituent like atoms/molecules as discussed below.

# 2.1.1 Hydrothermal technique

The term 'Hydrothermal' is made up from two isolated terms 'hydro' and 'thermal' and entails about the preparation of nanocrystal structure through chemical reactions by means of supplying thermal heat to the aqueous solvent kept under sealed environment. Instead of an aqueous solvent, many other solvents (like organic, salt, etc.) can also be used through the same procedure and named as 'solvothermal' synthesis process. The discovery of hydrothermal process started from the first report given by Karl Emil von Schafhäutl in 1845 with the invention of growing microscopic quartz crystals in a pressure cooker. It implies that a high temperature and pressure simultaneously grow nano-/microcrystals[101]. Hydrothermal process is an easy and efficient approach for getting crystals in powder as well as in thin film forms using the same deposition paramters[102]. It contains a teflon beaker which is inserted under a tightly sealed stainless steel case and kept inside the oven at the maximum temperature limit (constraints of auto clave) of ~200°C. This external temperature creates high pressure inside the beaker which also plays a major role for growing the nanostructure. Two major thermodynamic variables. temperature and pressure, simultaneously act on the samples to grow (nano)crystals.

Crystals may be formed in various architectures for which various external parameters are responsible. Precursor concentration, additives, pH of solution, surfactant, nature of solvent, etc. are the factors that control the architecture of the nanostructures. Initially, the precursor solution is gradually stirred at ~200 rpm (typical value) for minimum 30 minute to obtain a complete homogenous mixture of precursors. The solution is kept inside the teflon bath after preparing the homogenous

mixture of precursor salt and desired solvent and then sealed in the stainless steel chamber for further heat treatment in the oven. External control parameters such as temperature, time and rate of heating/cooling etc. can also change the morphology of the material to its nano form as the internal pressure changes due to changes in the external parameters. These all controlling factors are responsible to grow different nanostructures having different shapes and sizes.

Different inorganic nanostructures, studied in the current thesis, have been prepared using this hydrothermal method for different purposes and applications. Nanostructures of NiO, TiO<sub>2</sub>, Co<sub>3</sub>O<sub>4</sub>, NiCo<sub>2</sub>O<sub>4</sub> in powder and thin film forms have been grown and studied[46,103,104]. The thin films have been grown on a solid (like FTO/ITO) as well as flexible (carbon cloth CC) substrates. For this purpose, different substrates were kept in teflon holder with conductive side facing downward and then put into the teflon beaker. Thus, a very thin/thick film (depends upon the controlling parameter) is found to deposit over the substrate. The obtained film further passes through the rinsing (several time with distilled waterr) and drying process for removing the surface impurities. A schematic diagram in Figure 2.1 shows a typical hydrothermal setup.

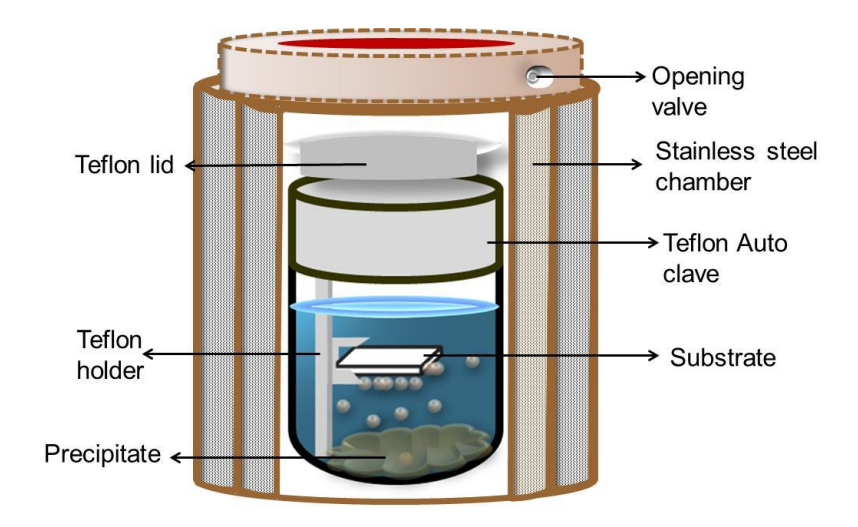


Figure 2.1: Schematic diagram showing a typical hydrothermal setup.

**Model used:** Stainless steel chamber and 50 ml capacity of Teflon beaker

# 2.1.2 Electrodeposition technique

Unlike various other techniques, this technique has its unique advantages for the deposition of thin film over a conducting substrate. As the name suggests 'electrodeposition' means due to the flow of electric charge, thin film grows at the electrode/electrolyte interface of the substrate[105]. Three electrode system in electrochemistry workstation is chosen to flow the charge using external power source. The threeelectrode system in electrochemistry is chosen to minimize unwanted obstruction under the effect of the external biasing (compare to two electrode system) during the working condition of electrode and electrolyte. Three electrodes consist of WE, RE, and CE as mention in Figure 2.2 and are connected with each other through conducting electrolyte medium in an electrochemical cell which contains necessary precursors for deposition[106-108]. An conducting electrode (e.g. ITO/FTO), on which film is desired, is used as the WE. The other two electrodes RE and CE consist of Ag/AgCl and Pt-wire electrodes respectively. Different morphologies can be obtained by appropriately choosing the control parameters like concentration of electrolyte, input voltage/current and deposition time. However, this technique has a very less variety of morphologies variation in comparison with hydrothermal method. Though, electrodeposition method is much popular due to its unique advantages like a homogeneity of film, strong adhesion to the substrate, and more life, which affects some applications deeply. Strong adhered film leads to better stability of the device which fabricated using them. The improved stability is a consequence of better bonding of material to the substrate's atom formed when deposited using an external bias.

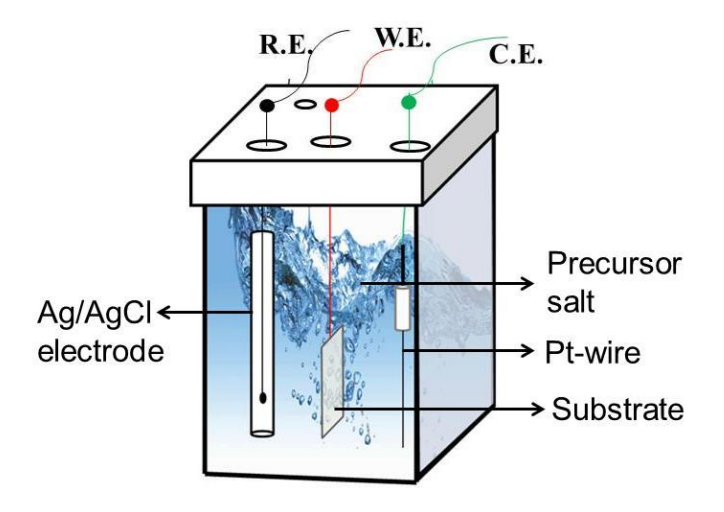


Figure 2.2: Schematic representation of an electrochemical cell used for electrodeposition using three electrode systems.

**Model used:** Keithley<sup>TM</sup> 2450 SMU electrochemical work station.

## 2.1.3 Spin coating and Drop casting

Spin coating and drop casting techniques are methods to obtain a thin solid film from the same material's liquid state and thus depends upon its initial state and nature of the substrate. In spin coating technique, small amount of material put on the substrate followed by spinning of that substrate, as shown in Figure 2.3. A rotating spinner carries a substrate, which accelerates at high speed and experience a centrifugal force at each atom of material which spreads to form a film. The spinning speed and concentration of solution are variable parameters to help in controlling the film thickness[109].

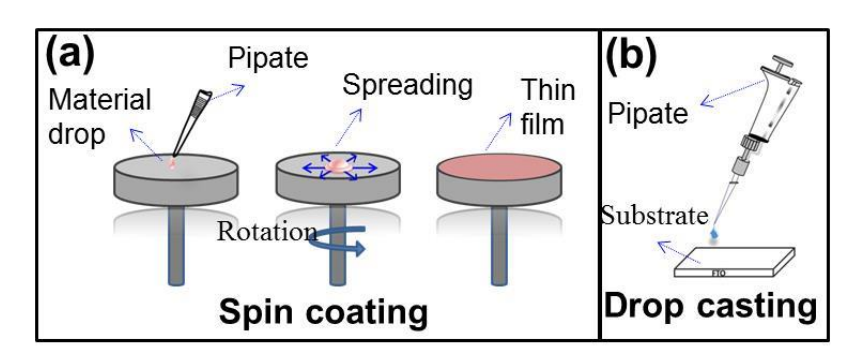


Figure 2.3: Schematic illustration of Spin coating (a) and Drop casting (b) techniques

Drop casting method is a smaller version of spin coating technique, in which preparation of material follows the same route as that of spin coating with same parameter like concentration, nature of solvent, etc. Materials with these parameters are put on the substrate and the solvent is allowed to evaporate, preferably in vacuum (Figure 2.3b). Both these methods generally used for preparing the thin film of organic/conducting polymer materials and have been used for depositing films during ECDs fabrication.

Model used: Apex Instruments, India

# 2.2 Characterization Techniques

Prepared samples are characterized using an appropriate technique to understand its properties. This is required to check the purity of prepared samples as well as as a part of optimization process. Different microscopic, diffraction, electrochemical and spectroscopic techniques have been used in the current thesis. Brief description of their basic working principle have been discussed below.

# 2.2.1 Scanning Electron Microscopy

Scanning Electron Microscopy (SEM) is a technique to study surface morphology of any material using high energy electron beam as a source. The whole set up is shown as a schematic in Figure 2.4. When the specimen is irradiated by these energetic electrons, different electron as well as photon signals are released from the material. These two emitted signals contains backscattered electron, (atomic number and topographic information), secondary electron, (topographic information), electrons (surface sensitive compositional information), augur cathodoluminescence (electrical information) and X-rays (through thickness and compositional information) and these signals are used to get different information about the specimen. Secondary electron, emitted after interaction between the specimen and incident electron, are used to get the surface morphology. Secondary electrons are emitted from the specimen surface due to inelastic scattering from the valance electron, and carries energy less than 50 eV. Electronic composition information of sample (i.e. about to Z) is collected through the elastic scattering which is produced backscattered electron having energy generally greater than 50 eV. There are many components, in an SEM, from the generation of electron beam to the detection of scattered/emitted electron or photons as discussed below.

#### 2.2.1.1 Electron gun

A SEM instrument which is having FE electron gun produces a high resolution image than others. For this, a tungsten wire works as a cathode in which a single crystal of tungsten is used. A curvature of 100 nm is given to the tip of this tungsten crystal, named as emitter. High potential is applied to that crystal which is responsible to eject the electron beam from the gun. The whole arrangement of electron gun is kept at high pressure about 10<sup>-8</sup> Pa.

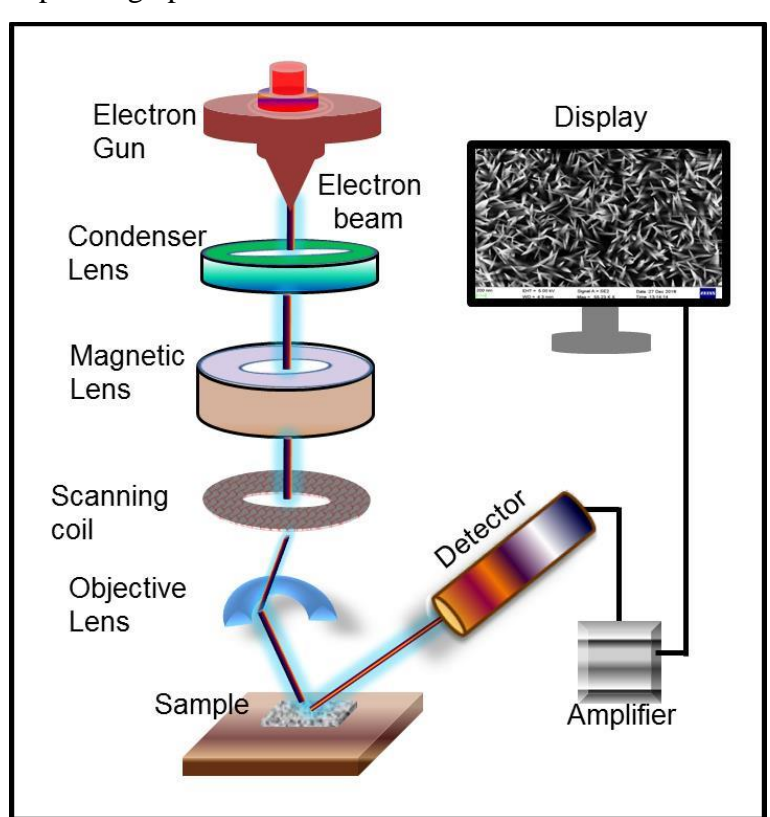


Figure 2.4: Schematic illustration of a FE scanning electron microscope.

#### 2.2.1.2 Condenser lens

Lenses are used below the electron gun for adjusting the diameter of electron beam. Strength of the condenser lens decides the electron beam will be narrower or broader under the application of high and weak field respectively. This electron beam passes through a small hole on the aperture plate, which is kept in between the condenser lense and objective lenses.

## 2.2.1.3 Objective lens

This is a crucial part of the instrument and used for focusing the electron beam at the final stage and determines the final diameter of electron beam which will be available to interact with the sample surface.

#### 2.2.1.4 Scanning coils

Travelling electron beam has a charge of electron and can be deflect with the effect of magnetic field. The field is produced and varied by passing the variable current in the coil and hence the electron beam passes through the scanning coil may sweep over the samples. Sweeping the electron beam allows one to scan the sample in broader region. Higher the scanning speed results to lesser resolution and with greater noise.

#### **2.2.1.5 Detector**

There are many detectors available inside the chamber to detect various emissions, discussed above. The detector captures the SE and BSE coming at different angles from the sample with different velocity and density. These all parameters collect electron at corona of detector followed by striking to the fluorescent screen. Produced photon from the screen is amplified by an attached transducer and given to the display as a video signal. A monitor is synchronized with the scan speed and detector which display the surface image of sample even at nanoscale.

Model used: FESEM, Supra55 Zeies.[110]

#### 2.2.2 Transmission Electron Microscope

A transmission electron microscope (TEM) works on the principle similar to that of an optical microscope and both can be explained in conjugation. Optical microscope contains glass lenses for transmitting light to produce the image. The resolution varies in the case of light by varying the focal length of the lenses with changing the whole lens manually. With bringing the greater improvement in magnification and

to collect some more information of material's structure at the atomic scale, the first TEM instrument was discovered by Max Kroll and Ernst Ruska in 1931.

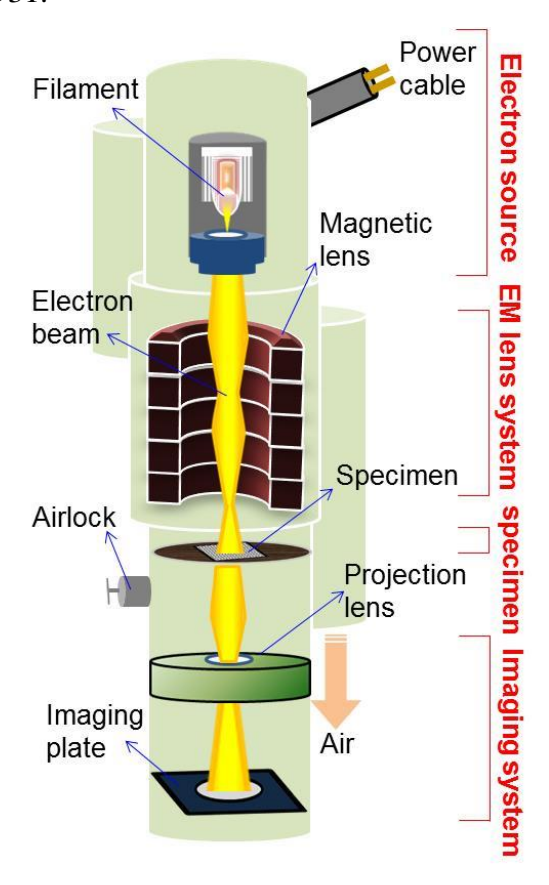


Figure 2.5: Schematic illustration of transmission electron microscope.

A TEM instrument consists of high energetic electron beam which is transmitted through the thin film of sample kept over a copper grid and image forms after the interaction of beam with specimen. The electron beams along with other components are placed inside the high vacuum to prevent the deflection of the electrons from the presence of gaseous particles inside the chamber. Main components of a TEM includes electron gun, magnetic lenses, sample holder and detector unit as shown in Figure 2.5. A field electron gun, typically works at 200 kV accelerating voltage, is used to emit the electrons with higher energy and can easily penetrate appropriately prepared sample. Focus of electron beam and the magnification of image can be tuned by varying the current of electromagnetic lenses. The fluorescent screen is attached to obtain the projection of image which delivers photons on irradiation by

the electron beam. A charge coupled device (CCD) detector camera is placed beneath the florescent screen to capture the radiated photons to display into the computerized digital image of sample.

**Model used:** High-resolution transmission electron microscope (HRTEM 200 KV FEI TECNAI G220 microscope)[111]

# 2.2.3 Atomic force microscopy

Apart from the other techniques to obtain morphologies with high magnification, an atomic force microscopy (AFM) technique also falls in this category and has been used in this thesis work. A sharp tip probes the surface architecture by scanning of the sample and displays the image of surface topography with the tremendously high magnification about 1000k X. The AFM is also used to find the three dimensional image which can provide the particle size or depth of holes (pits) with the measured parameter along the vertical dimension of surface structures. Other than imaging, AFM is also used to find thickness, I-V characteristics at atomic levels. Main components of an AFM with the variation of force at atomic distance of tip-surrface interaction in different operating modes is being briefly described as follows with the help schematic illustration in Figure 2.6.

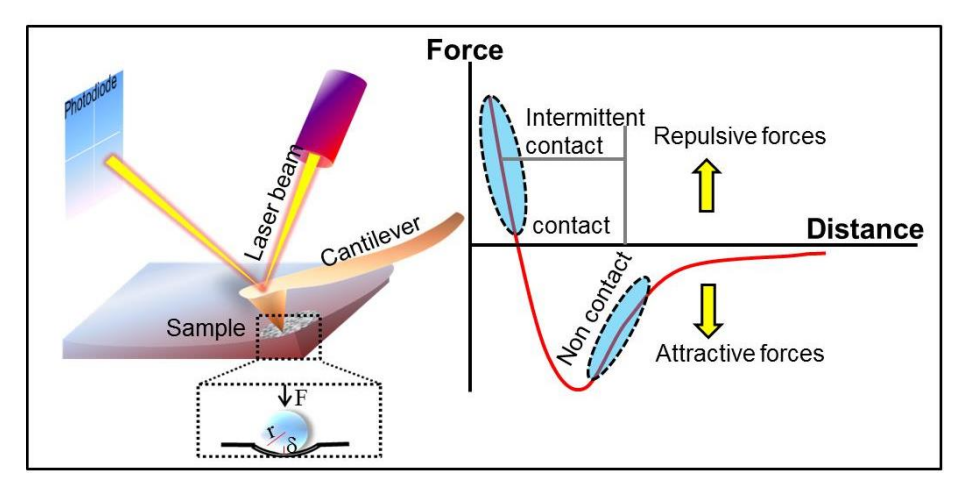


Figure 2.6: Schematic illustration of atomic force microscopy with the different operating contact mode.

#### 2.2.3.1 Cantilever

Cantilever is the probe of an AFM system which contains a fine tip for creating the contact to the surface of sample and detects the force between the tip and the surface. Once the cantilever tip approaches the samples surface, it can feel attractive or repulsive force from the sample in non-contact and contact mode respectively with following the Lenard zone potential profile between the tip and atoms on the surface. If the force is monitored, distance between the tip and surface can be known and thus the morphology can be known by imaging this force profile.

#### 2.2.3.2 Detection

The movement of cantilever in monitored using the deflection of laser beam falling on the cantilever (Figure 2.6). The reflection of laser beam takes place from the flat top portion of cantilever. To trace the reflected laser beam in different position, a position-sensitive photo diode (PSPD) is attached and thus finally provides the change in the cantilever's position. This change in position provides the accurate topography of samples and can also be used in imaging process.

**Model used:** Park Systems NX10.[112]

#### 2.2.4 X-ray diffraction (XRD)

X-Rays are electromagnetic radiation having shorter wavelengths, typically of the order of 1Å, and diffracts when interact with the crystals where the lattice planes acts as diffraction element. In crystallography, XRD is a main characterisation technique to get the phase/purity of samples. A brief mechanism of XRD from a sample is shown in Figure 2.7 and the same is being described here.

#### 2.2.4.1 Generation of X-ray

When a metal target is hit by high energy charged particles (say by stream of electron), make a cause of generating X-rays. On striking the target, electrons lose their kinetic energy to give electromagnetic radiation, called continuous X-ray (white radiation). Alternatively, the high energy electrons knock out the core electron from an atom of target material. Higher shell electron fills the vacancies on lower shell and

emits the electromagnetic radiation corresponds to the transition energy levels' difference, called characteristic (monochromatic) X-ray. These X-ray consist of high energy  $K_{\alpha}$  and  $K_{\beta}$  radiations having wavelength near about 1.54 Å , a typical value for the copper target. The most widely used target material for X-ray generation is copper, which fulfils the engineering as well as crystallographic conditions.

#### 2.2.4.2 Diffraction pattern

The X-rays coming from the source interact with the electron cloud of atom of material placed at sample holder over the goniometer. All atoms behave as diffraction centre and the crystal as a whole behave as a grating to diffract X-rays. A diffraction pattern is formed by following the Bragg's diffraction condition (Eq. 2.1).

$$2d \sin\theta = n\lambda \tag{2.1}$$
  
i.e. 
$$\frac{n\lambda}{2d} \le 1$$

where,  $\lambda$ , d and  $\theta$  are wavelength, interplaner spacing and diffraction angle respectively (Figure 2.7).

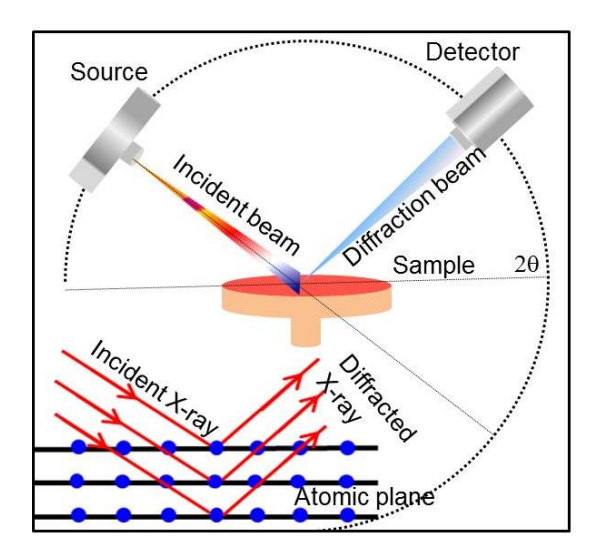


Figure 2.7: Schematic illustration of an X-ray diffractometer and diffraction from atomic planes.

#### **2.2.4.3 Detector**

The source, sample stage and detector is kept in a spherical geometry (called Ewald sphere), in which both source and detector can vary

between  $0^{\circ}$  to  $90^{\circ}$ . All the constructive interference signals coming from the sample is detected by the detector and plotted as a function of diffraction angle (20). This diffraction pattern contains information about different miller indices, corresponding to a lattice plane and thus used to draw the information about the sample phase purity, interatomic spacing, bond length/angle etc.

Model used: Rigaku SmartLab[113]

#### 2.2.5 Raman Spectroscopy

When a monochromatic visible light exposes to any sample, light get absorbed, reflected or transmitted. In addition, ~ 1% (or less) light also gets scattered and contains frequencies equal to or less/more than the incident light. Light which has same frequency as that of the incident light is called Rayleigh component and those scattered light having different frequency are called Raman component. Incident light interacts the sample leading to different electronic and vibronic transitions. If the electronic excitation and de-excitaion occurs at the sample level under illumination the same frequency radiation as that of the incident one will be present post scattering to yield high intense Rayleigh lines. On the other hand, Raman lines, having different frequencies as that of incident light, are further categorised into Anti-stokes and Stokes lines corresponding to higher and lower frequency components respectively. The amount by which the shift is observed depends on the vibrational energy levels and thus the Raman scattering contains this information about the molecule/material. Though a weak process, Raman spectroscopy has now been used as a tool for characterization in almost all areas of research. Various components of a typical Raman spectrometer, schematically represented in Figure 2.8, is being discussed below.

#### 2.2.5.1 Excitation Source

A high intense monochromatic laser beam is used to illuminate the samples for measuring the Raman bands. Appropriate laser source is chosen based on the nature of samples. Most commonly used lasers include argon laser (514 nm and 488nm), He-Ne laser (633 nm), diode lasers (532 nm, 785nm, 976 nm etc.) with an option of variation in power.

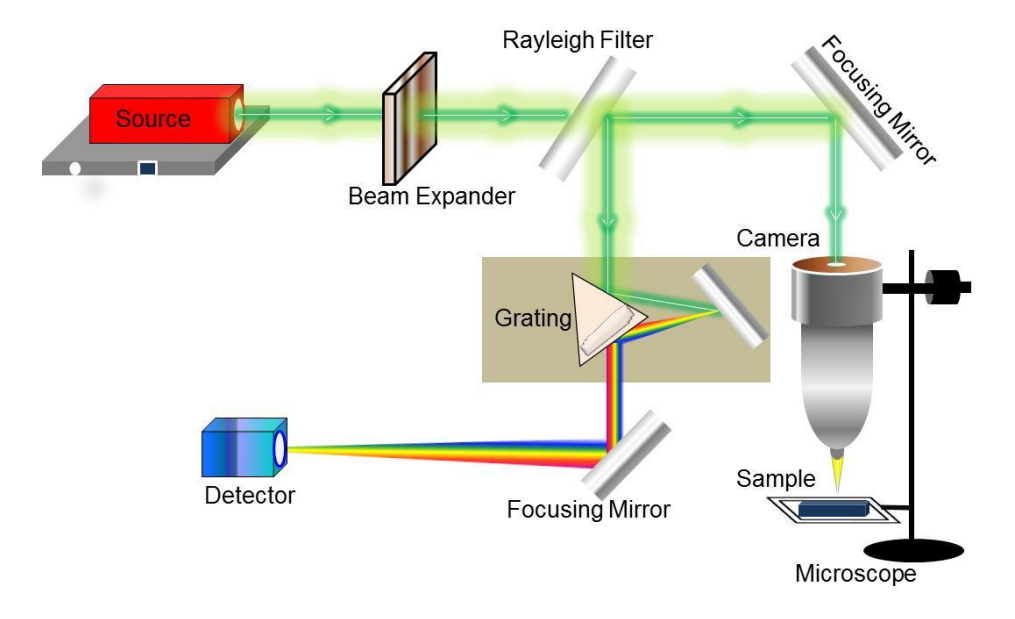


Figure 2.8: Schematic illustration of a typical Raman spectrometer.

#### 2.2.5.2 Optics of spectrometer

A Raman spectrometer is an assembly of many optical components from the laser source to the signal detection. There are many channels through which excitation and scattered light passes. Brief descriptions of these optical components are as follows:

**Microscope:** Optical lenses having different magnification and numerical aperture are used for focusing the laser on the samples at different area and high magnification exposes high resolution for lenses. The backscattered light comes from that selected area of samples and collected through the same optical lens for further operation.

**Grating:** Grating is a collection of a number of line spacing or grooves from which light get dispersed and the groove density decides the resolution. Higher resolution obtained through high dispersion amount by compromising the reduced intensity.

**Filter:** To cut and to pass the desired scattering wavelength, optical filters, like Rayleigh, notch, are used in Raman spectrometer. Since the spectrometer works at the backscattering mode, so Rayleigh filter is used

to remove the Rayleigh part from the scattering light and thus all Raman band are passed. Notch filters are used to obtain anti-stokes Raman line in addition to the Stokes one.

#### **2.2.5.3 Detector**

Currently, Raman spectrometers are designed by using CCD detectors due to its less signal to noise ratio and very fast response time i.e. high quantum efficiency. Scattered light from the sample projects onto the small light-sensitive pixels of CCD which finally provides the related signal intensity at different position (called Raman shift). A CCD is a silicon-based multi-channel array detector which works at about -70°C temperature with Peltier system.

Model used: Horiba LabRam Jobin Mirco-Raman spectrometer[114]

#### 2.2.6 X-ray photoelectron spectroscopy

X-ray photoelectron spectroscopy (XPS) is one of the best techniques to find the constitutes present in a sample. This is done by irradiating the sample using soft X-ray with limited penetrating power which interacts with the atoms presents on the sample's surface. The photoelectrons eject from the surface with different kinetic energy which is related to the binding energy and work function of each atom. Since each element has a different value of binding energy, elements can be easily detected by XPS measurement with high accuracy using the XPS set up, shown in Figure 2.9 described below.

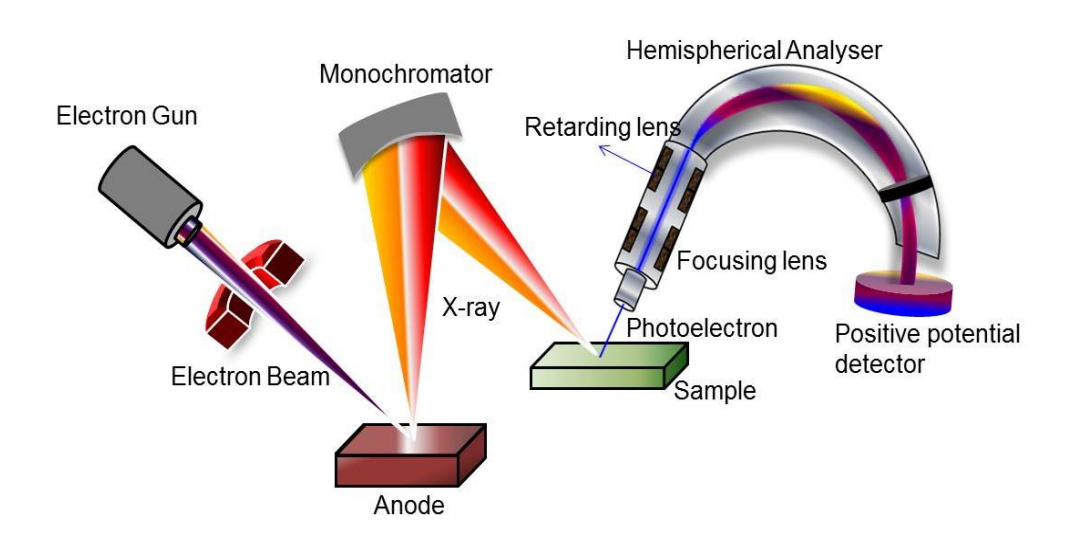


Figure 2.9: Schematic illustration of X-ray photo electron spectroscopy

#### 2.2.6.1 Electron gun

The said XPS system is equipped with Al K $\alpha$  (1486.6 eV) X-ray source. The whole system is kept under very low working pressure of 5 x  $10^{-9}$  Torr with maintaining the pass energy 20 eV to achieve energy resolution of 0.85 eV. The samples are cleaned using the in-built argon ion sputtering and after that it interacts with the X-ray beam.

#### 2.2.6.2 Anode

Often, two alternative common anode materials of Mg and Al are taken for the X-ray generation of sufficiently high energy. The characteristic Mg K' radiation at 1253.6 eV and the Al K' radiation at 1486.6 eV possess sufficiently high energies for core level excitation as well as a sufficiently low line width (below 1 eV) to yield XPS spectra with fairly good resolution. Usually source operates from 500 W to 1kW power at 5-15 keV anode voltage for generating the efficient irradiation.

#### 2.2.6.3 Monochromator

An XPS system consists of a monochromator made up of a bent quartz crystal which picks a fine line from the ordinary emission. The advanatage of monochromator in XPS system is to remove the Bremsstrahlung background with satellite peaks and to improve the energy resolution in final spectra.

#### 2.2.6.4 Hemispherical analyser

Two concentric hemispherical analyzers simultaneously work in any XPS system which is used for areal transmission and superior energy resolution. These two analyzers are kept at opposite biasing in which inner one is at positive potential and the outer one is kept at negative potential. An input lens is kept inside the hemispherical analyzers which defines the area to be analyzed. The input lens provides retardation to electron and thus reduces their energy before entering the analyzer. This reduced energy, called pass energy, indicates a lower absolute energy resolution. Therefore, angle resolved XPS occurs without tilting the sample at all.

#### 2.2.6.5 Positive potential detector

The hemispherical analyser is energy dispersive systems, which can used simultaneously to detect electrons arriving at different locations in the dispersion plane. Therefore, parallel multichannel detection of a certain energy range (usually about 10% of the pass energy) enabled in the detector. In some XPS system in a variety of ways, for example, by using a channel plate for amplifying the electron current, resistive plate as a position-sensitive and phosphorescence screen used for the mapping.

**Model used:** A synchrotron source with a double-crystal monochromator [Si(111), with an excitation 155 energy of 4.4 keV] in Beamline 14.

#### 2.2.7 UV-Vis Spectroscopy

Basic optical properties (absorption, transmission) of samples are probed using a UV-Vis spectroscopy which probes electronic structure of a sample. A Xenon lamp (or a combination of Tungston and Duterium lamps), source of visible light, is used in a typical UV-Vis spectrometer (Figure 2.10) which disperse into different monochromatic wavelengths after passing through the grating. Different wavelengths individually interact with sample and corresponding electronic transitions and attenuated signal received thereupon is used to get information about various electronic properties of that sample. This electronic transition can be captured through two techniques, known as Diffused reflectance spectroscopy (DRS), Absorption/Transmission spectroscopy.

#### 2.2.7.1 Diffused reflectance spectroscopy

Once the white light with different wavelength interact with sample, some of light gets absorbed by the material and rest light may get reflected. The reflected light, if comes from the diffused surface (like powder samples or thicker samples), is collected from the integrated sphere. By looking at the variation of (diffused) reflected light

component as a function of the energy the band gap can be obtained using the Kubelka-munk relation (Eq. 2.2).

$$[F(R) * hv]^{1/n} = C[hv - E_g]$$
 (2.1)

where, F(R) is Kubelka-munk function and hv is energy corresponding to different wavelength and C is proportional constant. The intercept of the curve represented by Eq. 2.2 on the hv axis gives the band gap value for both indirect band material (n=1/2) or direct band material (n=2).

#### 2.2.7.2 Absorption/Transmission spectroscopy

Absorbance/transmission mode of this spectroscopy can be used only for the thin film and liquid samples. The procedure of this mode is same as that of the reflectance mode but the detector captures the light in terms of absorbance or transmission, which can be further modified into the absorption coefficient ( $\alpha$ ) to calculate the band gap using the same Taucplot relation with Eq. 2.3 .

$$(\alpha * hn)^{1/n} = C(hn - E_g)$$
 (2.3)

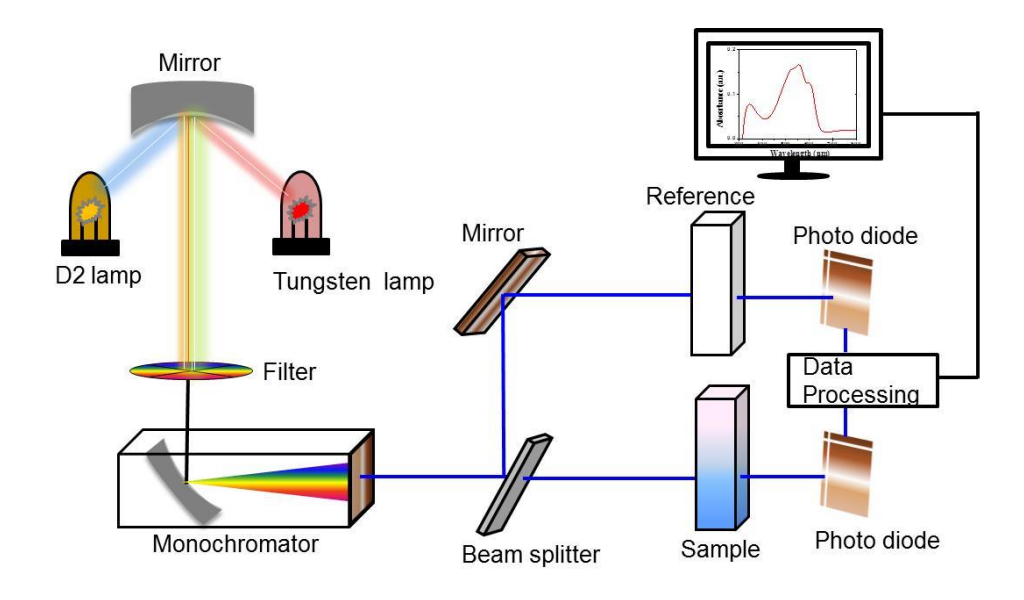


**Figure 2.10**: Schematic illustration of UV-Visible spectrospcopy in absorption/transmission mode.

**Model used:** Perkin Elmer (Lambda-365, Lambda-750), Agilent (Cary-60)[115,116]

#### 2.3 Electrochemical measurement

Electrochemistry is one of the best techniques to know about the electron transport property of material through ionic electrolyte medium during electrochemical measurement. Electrochemical measurement typically consists of three electrode based system which is used for minimizing the resistive effect other than material alone, as discussed in section 2.1.2. Three electrodes mainly consists of WE, RE(calomel or Ag/AgCl) and CE(Pt-wire) which diverts the path of current and voltage so that net resistive effect decreases. For creating the ionic electrolyte, ionic solution like KOH, NaOH, KCl etc. are made up at its minimum concentration so that the pH of electrolyte does not affect the material's property. There are many ways to provide input and getting the corresponding output with the help of galvanostatic and potentiostatic methods as discussed below.

#### 2.3.1 Linear Sweep Voltammetry

A range of fixed potential is applied in Linear Sweep Voltammetry (LSV) function across the RE and WE. Current, corresponding to each applied voltage is measured to get an I-V curve. Characteristics of the LSV depend upon following factors:

- ➤ Electron transfer reaction rate in electrolyte.
- Chemical reactivity of material to the electroactive species.
- ➤ Voltage scan rate

#### 2.3.2 Cyclic Voltammetry

Cyclic Voltammetry (CV) similar to LSV, follows the same procedure with delivering small constant steps of potential in wide potential window. Additionally, there is minimum three potential terminal in which applied potential vary with a given scan rate. Initially, a potential induces flow of current through cathodic path (say  $V_1$  to  $V_2$ ) and after  $V_2$ , it comes back through anodic path (say  $V_2$  to  $V_1$ ). As a result, the

given potential window completes a cycle. The advantage of cyclic scan from  $V1 \rightarrow V2 \rightarrow V1$  is to find the oxidation as well as reduction behaviour of material in a single cycle, i.e. to know the redox reaction of material in a single potential window. Material having only the oxidation property does not show any peak under anodic scan and is also valid for the reduction process. A low resistive electrolyte is generally used to enable easy flow of current.

Model used: Keithley 2450 SMU[117]

#### 2.3.3 Chronopotentiometry

Choronopotentiometry means the potential varies with time once the input current remains constant for that whole duration of experiment and comes in the category of galvanostatic method. The constant current is provided to WE with respect to CE and corresponding potential is measured between RE and WE. To balance the applied constant current, redox species diffuse at the WE until the diffusion of all redox species reaches its limiting values. A major application of chronopotentiometry is to examine charging/discharging properties of electrodes for battery/capacitor like applications.

#### 2.3.4 Chronoamperometry

Chronoamperometry technique is used for getting the current response as a function of time for a given applied potential. A faradic reaction takes place at the surface of electrode and allows the current to flow. This technique has been used for sensing application in the current thesis.

#### 2.3.5 Nyquist plot

During electrochemical measurements, some resistance is involved originating from many routes during any potentiostatic or galvanostatic measurements. To find the exact resistance offered by the electrode to the electrolyte, individually or in contact, is measured by Nyquist plot. A long range of frequency from 20 Hz to 30 MHz is used to find the impedance (Z) and obtain different semi circles between Im(Z) and Re(Z). The diameter of these semicircles hints to the effective impedance of different parts of WE/ electrolyte interface. The semicircle behaviour

obtained at low and high frequency ranges give an idea about the impedance offered by the electrode/material interface and material/electrolyte interface from the diameter of the these separate semicircles. Nyquist plot also helps to find any new material towards its capacitive behaviour from the vertical line at the high frequency which is a signature of high impedance for the frequency signal likely happens in capacitor.

#### 2.4 Sample preparation recipes

Following recipes have been used to prepare different samples and devices.

#### 2.4.1 Synthesis of NiO nanopetals

Nickel oxide (NiO) NPs NPs have been prepared using abovementioned hydrothermal method (section 2.1.1) on conducting ITO coated glass substrate. Ingredients to form NPs are Ni(NO<sub>3</sub>)<sub>2</sub>.6H<sub>2</sub>O, and K<sub>2</sub>S<sub>2</sub>O<sub>8</sub>, NH<sub>4</sub>OH taken in appropriate quantities. Different concentrations of Ni(NO<sub>3</sub>)<sub>2</sub>.6H<sub>2</sub>O of 60 mM, 80 mM and 100 mM has been taken in aqueous solution. The amount of K<sub>2</sub>S<sub>2</sub>O<sub>8</sub>, NH<sub>4</sub>OH was kept constant with the value 0.06 g and 1.2 ml respectively in 30 ml distilled water (DI). With a proper arrangement, the ITO substrate were kept facing downward towards the bottom of the autoclave. Chemical reaction was carried out in an electrical oven at 150°C for three different concentrations for 5 h continuously. After chemical reaction took place inside the autoclave, all samples were rinsed by DI water and annealed at 250°C for 2h. Samples, which have concentration of Nickel nitrate 60 mM, 80 mM, 100 mM has been labelled by S1, S2, and S3 (these sample labelling is based upon their application and characterisation for FE application in chapter 6) and well aligned NPs observed with different thickness and density[103].

#### 2.4.2 Synthesis of TiO2 Nanorod

Like NiO NPs, hydrothermal synthesis process was carried out to prepare well aligned TiO<sub>2</sub> Nanorod (TNR) on conducting FTO coated

glass substrate. For the homogeneous alignment of TNR, 300 ml titanium butoxide, 10 ml hydrochloric acid (HCl) stirred in 10 ml deionized water, was used. A transparent solution was obtained after continuous stirring for one hour signify its homogeneous nature. The FTO substrate was cleaned for 10 min in ultrasonic bath in the presence of isopropanol, methanol, and acetone in equal amounts. For deposition of film, the solution was transferred into a teflon bath in which FTO was placed facing downwards with proper arrangement for 5 h. After cooling and taking out the sample, it is rinsed with DI water several times to remove the impurity. Finally, to improve the crystallinity, thermal annealing was carried out for 3h at 250°C following the abovementioned deposition step and result the vertically aligned TNR obtained[104].

#### 2.4.3 Synthesis of NiCo<sub>2</sub>O<sub>4</sub> nanoneedle

A simple and convenient hydrothermal method has been used for deposition of nickel cobalt oxide on two different substrates for further characterization and application. For this purpose, an aqueous solution of Ni(NO<sub>3</sub>)<sub>2</sub> and Co(NO<sub>3</sub>)<sub>2</sub> in 1:2 molar concentration was used as precursor to obtain spinal crystal structure of Ni and Co atoms in oxide form. The homogenous light pink colour solution obtained after vigorous stirring of Ni and Co precursors in 30 ml DI water and further treated by gradually adding 0.25 g urea. After the complete mixing of all ingredients, solution has been kept in Teflon bath for further heating treatment via hydrothermal method. To deposit the film of same constituents, conducting CC and FTO coated glass substrates were placed inside the Teflon bath with special arrangement. The autoclave, consisting of the above Teflon bath, was then kept in oven at 120°C (for 12 hr) for deposition to take pace followed by cooling under ambient condition. The as-deposited film was rinsed and dried at 100°C for 10 hr. These nanostructures align vertically over the planner FTO coated glass substrate and three dimensional vertical growths occurs over curved CC[118].

#### 2.4.4 Synthesis of nano-Co<sub>3</sub>O<sub>4</sub>

An electrodeposition method in constant current mode, with customized recipe, has been used for preparing nano cobalt oxide film which is tightly bound to the conducting FTO coated glass (used as substrate) due to the crystal matching between the two. For this deposition, Co(NO<sub>3</sub>)<sub>2</sub> was taken in a desired amount with small amount of NaNO<sub>3</sub> in 20 ml distilled water. A good nucleation, for achieving the desired film quality, followed by growth occurred on applying a constant current of 0.3 mA for three hours in a three electrode system in an electrochemical cell. An electrochemical workstation with Ag/AgCl (reference), Pt wire (counter) and FTO substrate (working) electrodes is designed for the electrodeposition technique. The as-deposited film was given heat treatment at 60°C for one hour to remove any contamination from the surface and finally nano bubble like morphologies obtained for Co<sub>3</sub>O<sub>4</sub> structure[106,107].

#### 2.4.5 Synthesis of nano-Prussian Blue film

There are two main steps to deposit the Prussian Blue coordination compound over the conducting FTO substrate using electrodeposition technique in constant current mode. A solution of 0.01 M  $K_3$ [Fe(CN)<sub>6</sub>], 0.01 M FeCl<sub>3</sub> and 0.05 M KCl is taken in three electrode system, where Ag/AgCl as reference electrode, Platinum wire as CEand FTO coated glass as WE were used. Deposition of PB film on FTO substrate was carried out under a current density of -50  $\mu$ A/cm<sup>2</sup> for 300 seconds. Then, as deposited Prussian blue films were washed with DI water and annealed at 50°C for 60 minutes[108].

#### 2.4.6 Preparation of Ethylene Viologen (EV) gel

Following steps were used to prepare EV gel in polyethylene oxide matrix.

- Ethyl Viologen dibromide of 0.3 wt % dissolved in methanol and stirred for 10 minute to make a homogeneous mixture.
- ➤ Polyethylene oxide (PEO) of 4 wt % has been mixed in acetonitrile and stirred in vortex for 1 hr.

After preparing above two solutions, EV solution is mixed with the PEO gel in 2:3 ratio and drop-casted over the desired substrates (EC electrodes in the present case).

### Chapter 3

# **Inorganic Nanomaterials for EC Electrodes**

This chapter presents electrochromism exhibited by inorganic nanostructures of transition metal oxide (TMO) electrodes. Optical modulation under an applied bias have been studied from nanostructured thin films of Prussian blue, NiO, TiO<sub>2</sub> and Co<sub>3</sub>O<sub>4</sub> deposited using hydrothermal and electrodeposition methods<sup>1,2</sup>. These nanostructures in different nanoarchitectures (NPs, nanorods etc) have been prepared and adequately characterized. Material characteristics and EC properties have been studied in detail along with establishing the color changing mechanism. Possible application in a solid state ECDs have been discussed<sup>34</sup> as demonstrated in other chapters.

<sup>&</sup>lt;sup>1</sup> Devesh K Pathak et al, Superlattices and Microstructures 125 (2019), 138-143

<sup>&</sup>lt;sup>2</sup> Devesh K Pathak et al, Superlattices and Microstructures 126 (2019), 1-7

<sup>&</sup>lt;sup>3</sup>Devesh K Pathak et al, Appl. Phys. Lett. 116,(2020) 141901

<sup>&</sup>lt;sup>4</sup> Devesh K Pathak et al, ACS Appl. Electron. Mater. 2, 6, (2020) 1768–1773

#### 3.1 Transition metal oxide: Inorganic EC material

#### 3.1.1 Background study

EC inorganics materials' belong to the transition metal oxides family and exhibit color modulation phenomenon due to the IVCT process when biased[51,119–122]. The electron transportation in IVCT is driven by the existence of material in different oxidation states. The IVCT process thus affects the absorption properties of material which in turn affects the appearance of the material under different bias conditions. Therefore, an intense band (or dip) of absorption (or transmission) appears during the electron transfer process under the illumination of UV-Visible light when the material is under an appropriate external applied voltage. This applied voltage creates the charge-balancing counter flow of electron in the whole circuit to result in a variation of electron density in the EC material and hence a modulation on their optical properties can be seen using absorption spectroscopy. The applied voltage is in order of few volts (mainly less than 2 V) to initiate the electron interaction reaction for changing the optical spectrum in nanomaterials. In many cases, more charge transfer is required to obtain an appreciable change in spectrum thus a higher operating voltages are needed which is not desirable from application point of view. Therefore, there should be an optimization of the material for getting an improved ECDs/electrode[123–125].

#### 3.1.2 Redox polarity dependent Electrochromic

Prior to exploring the application in actual device, material's EC behavior is tested by a voltage sweep preferably in an electrochemical cell. For this, the material is deposited in solid thin film phase over conducting transparent (ITO/FTO in the present work) substrate. Under the voltage sweep, the molecule gets dynamically oxidized or reduced from its neutral form and associated optical modulation is seen as color change. Table 3.1 is containing the lists of different inorganic EC materials which show their chromic modulation under anodic or

cathodic scan and thus characterized based upon their polarity[61,126], shown in table 3.1.

Table 3.1: List of commonly used inorganic EC materials.

Polarity group	EC material	Color	
		Neutral	Colored
		State	State
Cathodic	TiO <sub>2</sub>	White	Dark Blue
	Nb <sub>2</sub> O <sub>5</sub>	Yellow	Dark Grey
	MoO <sub>3</sub>	Transparent	Blue
	Ta <sub>2</sub> O <sub>5</sub>	Transparent	Deep Blue
	WO <sub>3</sub>	Light Yellow	Blue
	$V_2O_5$	Yellow	Green
	MnO <sub>2</sub>	Brown	Pale Yellow
Anodic	Co <sub>3</sub> O <sub>4</sub>	Yellow	Brown
	NiO	White	Brown
	RhO <sub>2</sub>	Yellow	Green
	$V_2O_5$	Yellow	Green/Grey

It is interesting to note that  $V_2O_5$  shows electrochromism under positive as well as negative bias which enables it to be an EC active material as well[127]. The list in table 3.1 is not exclusive and there exist many binary- and ternary mixed oxides as well as oxyfluorides. All of the above transition metal oxide shows thier chromic modulation from one color state to the other at a given external potential and revert back to original color state following the reversible redox reaction route. As discussed earlier (section 1.3), modern inorganic EC materials' family is occupied mainly by (transition) metal oxides in thin film or nanomaterial form. Thus the fabrication technique to get an optimal thin film or nanostructured form becomes equally important especially when actual applications are targeted.

As mentioned earlier, (chapter 2) in an attempt to design an ECDs, an active electrode is first prepared using an appropriate material (organic or inorganic). This electrode is later used in a device along with other components of the device. The prototype device designing is technically same for all EC materials but the working mechanism might be different. The metal oxide in the EC electrode, might have mixed conduction for ions and electrons, and the introduction of ions from an adjacent electrode/electrolyte need to support from the CE for charge-balancing counter flow of electrons. The electron in the film will remain to be there as long as the ion resides there, thus the material changes its optical properties with the persistence change in visible color. The noticeable change in color also depends upon the EC material with the injection of electron. Therefore, to make the device or to test the single EC electrode, there must be a counter supporting electrode that will support the injecting/extracting of the electron from the active material easily and significantly. The pt-wire, conducting transparent material (FTO/ITO) etc. like electrode can be used as an auxiliary electrode for optical modulation. Some TMO nanomaterials have been prepared and their EC properties have been studied as discussed below.

#### 3.2 Nickel oxide

As mentioned above (table 3.1), NiO shows its chromic modulation under a positive bias and reversibly change its appearance from transparent to black/brown colour. Coming from an inorganic family, it is a robust material but needs higher operation voltages thus compromising the efficiency. An attempt has been taken to prepare NiO nanostructures to address this issue so that a power efficient ECDs can be designed.

#### 3.2.1 Characterisation of prepared NiO film

The NiO thin film has been prepared using hydrothermal method using the recipe presented in chapter 2 (section 2.4.1). The prepared sample has been taken initially for the XRD analysis to check the crystal structure of prepared NiO phase with high purity. The XRD data (Figure

3.1a) proves the deposition of pure NiO crystal structure film deposited over the substrate as the data completely matches with JCPDS no 73-1519[128]. Further to confirm, Raman spectroscopy has been performed using 633 nm excitation wavelength source (Figure 3.1b shows various Raman modes of NiO at 515 cm<sup>-1</sup> (LO) and 1120 cm<sup>-1</sup> (2LO) which completely matches with earlier reports. In consonance, Raman and XRD, confirm the deposition of NiO phase on ITO substrate (NiO@ITO) for further studies[129].

The deposited NiO@ITO film is transparent (~70-90%) in the visible window as can be appreciated from the transmission (absorption) spectrum in Figure 3.1c (inset). The band gap of NiO@ITO has been estimated using DRS which comes out to be ~ 3.9 eV (Figure 3.1d. This high band gap value compared to bulk NiO (3.5eV) hints at the formation of nanostructure in the sample[130]. To confirm the same and to further understand the morphology, SEM measurement was performed which reveals nanopetal like geometry with sharp edges and possesses greater porosity (Figure 3.1e). These sharp edges of NPs can be capable of acquiring high charge density at the edge and may prove to be good field emitters for FE display applications. The same has been studied and reported in chapter 6. The enlarged top view of nanopetal's in Figure 3.1f is giving a consequence of the formation of nanostructures at 200 nm scale. The homogenous deposition of nanopetal like structure in X-Y plane and along the Z-height makes it favorable for any application. Single nanopetal has been examined using TEM (Figure 3.1g) which gives a solid evidence of the presence of nanostructure film. Selective area electron diffraction (SAED) pattern of NiO NPs geometry in Figure 3.1h shows the discrete diffraction fringes which always lead to the formation of polycrystalline material. The polycrystalline NiO NPs material is all set to be tested for electrochemical properties so that its application as EC electrode can be explored.

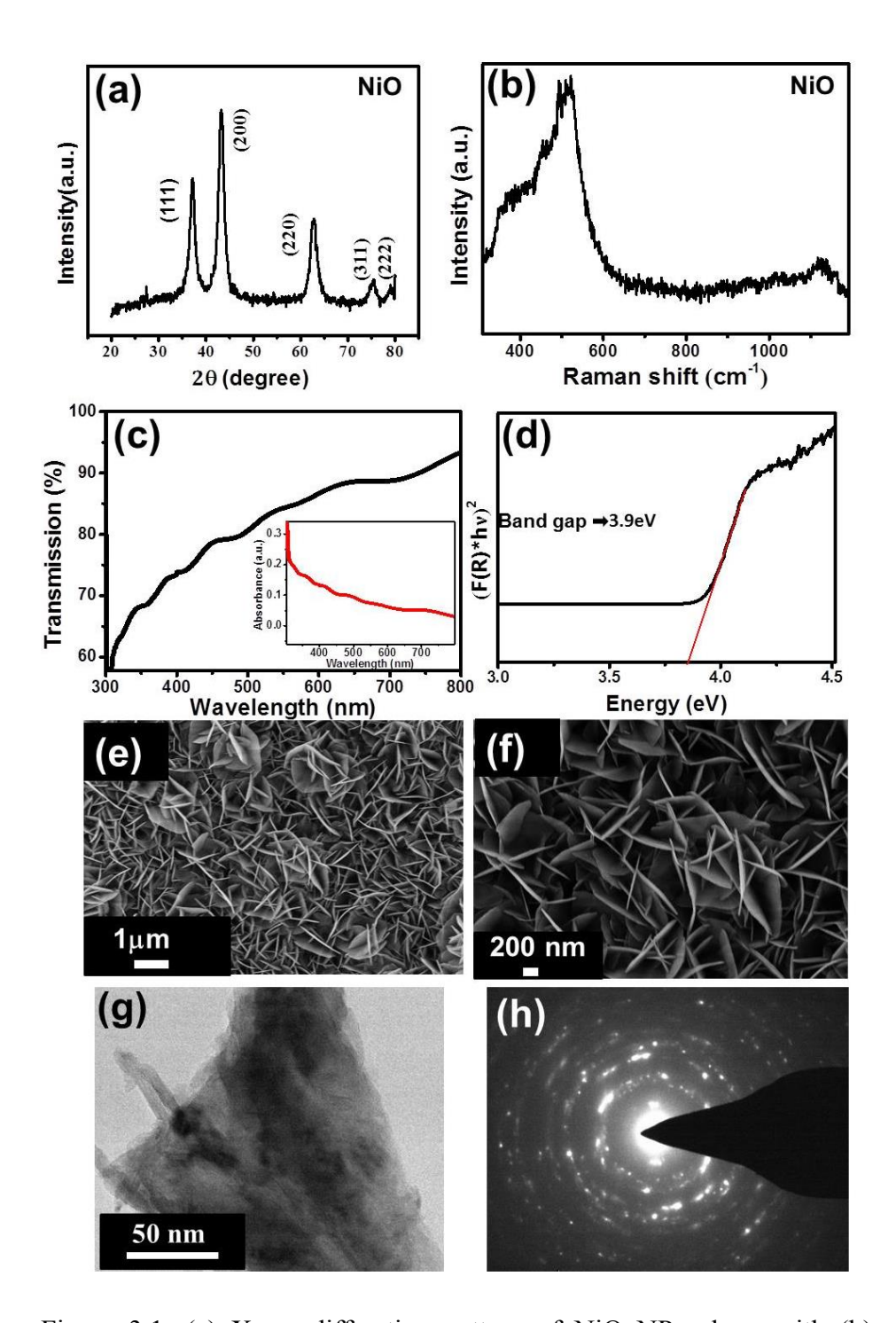


Figure 3.1: (a) X-ray diffraction pattern of NiO NPs along with (b) Raman Spectrum, (c) Transmission and absorption (inset), (d) diffused reflectance spectroscopy(e) top view-SEM, (f) Zoomed view at 200 nm scale, (g) TEM and (h) corresponding SAED pattern.

#### 3.2.2 Electrochemistry of Nickel oxide

Electrochemical properties of NiO@ITO have been measured using CV (CV) in a 1M KOH (aqueous) medium using three electrode systems in which the NiO@ITO electrode was used as WE. The CV measurement in the potential window from -0.2V to +0.4 V at the constant scan rate of 50 mV/sec displays the effect of chromic modulation under the positive scan (Figure 3.2a)[72]. The electrochromism of NiO transforms its natural transparent state to dark color at an applied voltage of 0.3V as clear from the corresponding photograph shown in Figure 3.2a. In other words, NiO NPs can form a suitable anodic EC material for EC switching between transparent and dark brown color.

The electrochromism of NiO follows the following reaction (3.1) taking place as a result of ion intercalation/de-intercalation at the electrode through the electrolyte ion (say OH in KOH electrolyte). The conversion of NiO to Ni(OH)<sub>2</sub> under the oxidation process at 0.3 V is responsible to change the oxidation state of Ni from +2 to +3 and revert back to the original state under the cathodic scan of quasi-stable Ni(OH)<sub>2</sub>. The change in oxidation state accompanies the corresponding optical absorption change and the same is perceived as a chromic modulation (Figure 3.2a).

$$NiO + OH^- \leftrightarrow NiOOH + e^- \tag{3.1}$$

The two colored states (coloration and bleaching state) of NiO@ITO electrode can be appreciated using their bias dependent change in absorption spectra (Figure 3.2b). The red curve (the bleached state) of NiO@ITO electrode shows less absorption (more transparent) in the visible range and transforms suddenly to the higher absorption (less transparent) value for colored state of electrode (the black curve, Figure 3.2b). The overall increment in the absorption for colored state in the visible range of wavelength is a sign of good contrast between these two chromic states. Wrapping the current discussion, the hydrothermally grown NiO-NPs appears to be a potential candidate to be sued as an anodic EC active electrode with good CC in the inorganic materials'

family. The morphology also suggests its potential application in FE displays to be discussed later on.

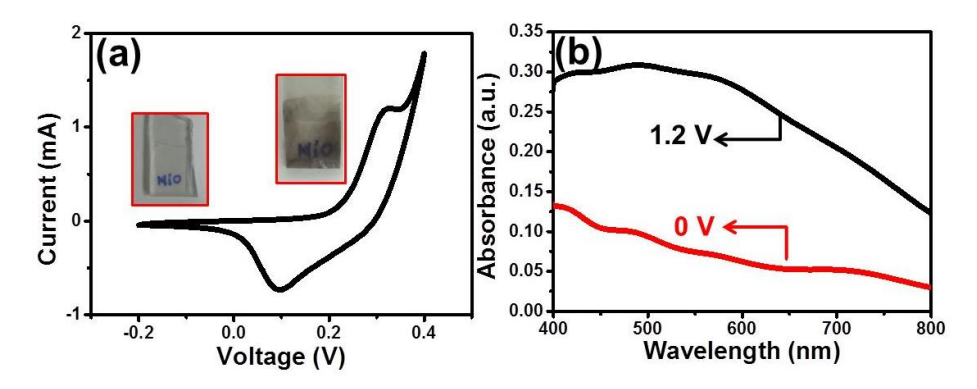


**Figure 3.2:** (a) CV of NiO@ITO in 1M KOH (aq) electrolyte with two chromic state and (b) Optical absorption of colored (brown) and bleached (transparent) state of NiO@ITO electrode under two different bias states.

#### 3.3 Titanium oxide nanostructures

Nanostructured TiO<sub>2</sub> thin film is another known material for EC active species and shows its electrochromism (poor) in the negative potential making it a cathodic EC material. It shows its chromic modulation due to the charge insertion/extraction mechanism. Basic characteristic of a hydrothermally grown TiO<sub>2</sub> electrode on FTO has been studied here for different applications as EC and FE electrodes[131].

#### 3.3.1 Characterisation of Titanium oxide

Hydrothermal method has been used to deposit the TiO<sub>2</sub> nanostructure over a conducting FTO coated glass substrate using the recipe described earlier (section 2.4.2). The phase purity of prepared film is started from the XRD data (Figure 3.3a) recorded at a glancing angle 2°. Figure 3.3a is showing diffraction peaks corresponding to different lattice planes which completely match with the rutile phase of TiO<sub>2</sub>. There are no other peaks arising which confirm the phase purity of sample. Further Raman spectrum recorded using 633 nm excitation also confirms that four Raman active modes observed at 144cm<sup>-1</sup>, 234cm<sup>-1</sup>, 448cm<sup>-1</sup> and 612 cm<sup>-1</sup> belong to the TiO<sub>2</sub> rutile crystal structure (Figure 3.3b). Raman

and XRD data, in consonance, confirm that the obtained film is of TiO<sub>2</sub> without any impurity[132,133].

The prepared film appears translucent white to understand it more quantitatively percentage transmission of the prepared electrode has been measured using UV-Vis spectroscopy (Figure 3.3c). Upto maximum 30 % transmission of visible light through it is observed which means that it absorbs largely the visible light (inset, Figure 3.3c). The whitish TiO<sub>2</sub> film has been taken for the band gap estimation (using Kubelka-Munk relation through Tauc-plot) by taking the DRS setup data (Figure 3.3d). The intercept of the (F(R).hv)<sup>2</sup> v/s hv curve, on hv axis[134], gives the value of band gap which is coming around 3.19 eV, higher than the bulk TiO<sub>2</sub> (3.0eV). This higher value of band gap is likely due to the formation of quantum effect, the band gap enhancement on moving toward the nano scale from bulk. Presence of smaller nanostructures has been confirmed using electron microscopy as discussed below[135,136].

The morphology of the prepared sample shows that Titanium oxide nanorods (TNR) have been deposited on FTO coated glass substrate (TiO<sub>2</sub>@FTO) as revealed by SEM. The SEM image (Figure 3.3e) shows a homogeneously packed dense TNR and seems to have grown vertically on the substrate. To ensure homogeneous vertically aligned deposition of nanorods, the substrate was placed parallel to the bottom surface of autoclave inside the teflon bath. Other parameters affecting the uniform deposition on the FTO substrate include stirring time, deposition temperature, annealing temperature/process etc. Information about the height of TNR has been obtained by taking the cross-sectional SEM image. Figure 3.3f clearly shows that the nanorods of TNR having height of about 2µm are by-and-large aligned. Crystallinity of these individual TNR has been checked using HRTEM (Figure 3.3g) which shows rods of ~ 10nm with two facets of the rod visible in the current frame. Inset of Figure 3.3g shows the surface plot, obtained using ImageJ<sup>TM</sup>, showing approximately seven lattice fringes in about 2nm.

The TNRs have even sides and rough top surface with single crystalline rutile phase grown in the (001) direction with the fringe width of  $\sim 3$  Å.

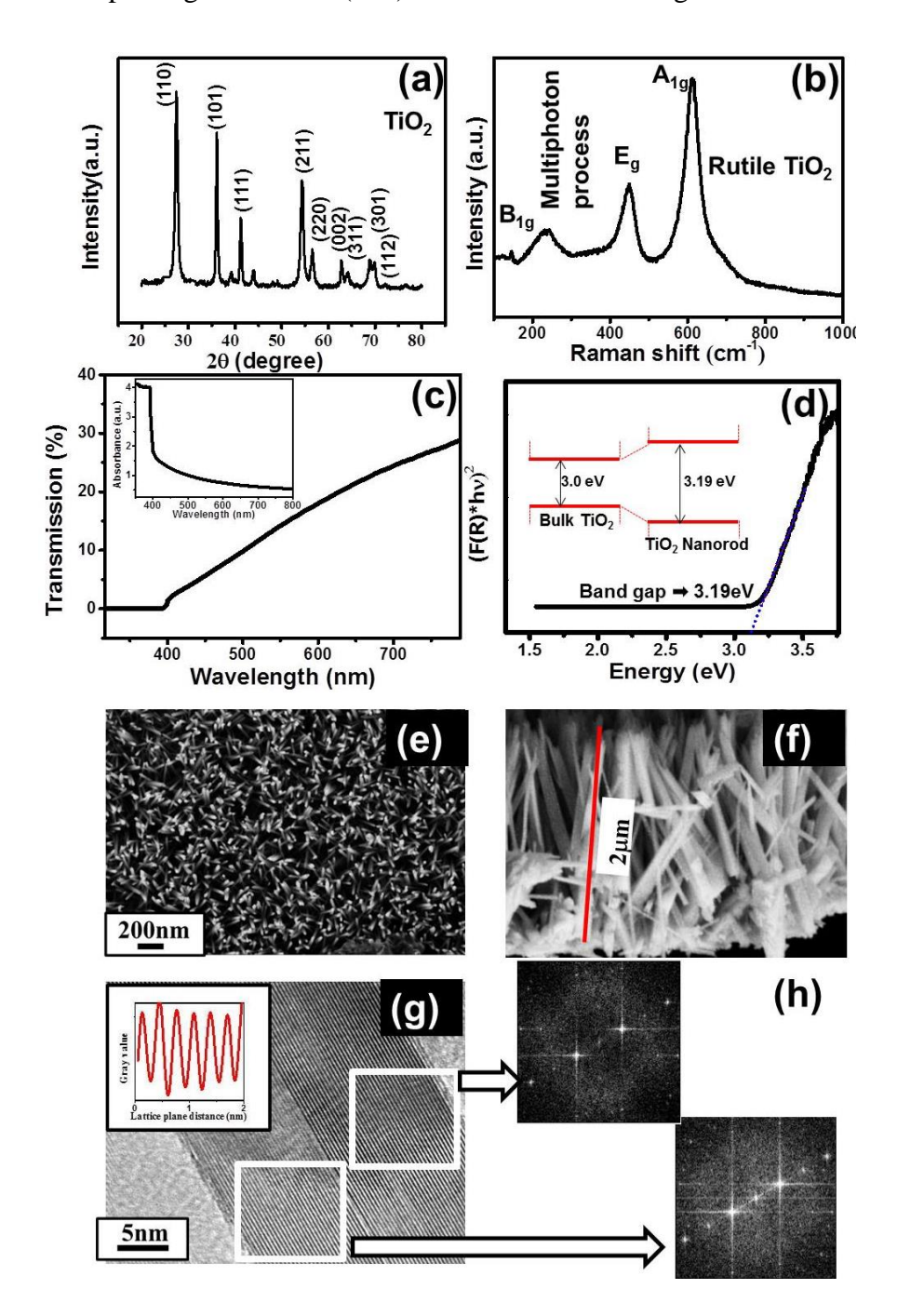


Figure 3.3: Basic characterization of the hydrothermally deposited TiO2 using (a) XRD, (b) Raman spectroscopy, (c) Transmission and absorption (inset) spectroscopy, (d) DRS, (e) top view SEM and 9f) cross-sectional SEM, (g) HRTEM image showing lattice planes and its line profile (inset) and (h) Fast Fourier Transform pattern obtained using ImageJ.

Uniform lattice parameters illustrate the growth of these nanorods in a single plane, which can clearly be confirmed from the fast fourier transform (FFT) image shown in Figure 3.3h (obtained using ImageJ<sup>TM</sup>) consisting of spots well-aligned in a single line perpendicular to the wires' alignment in real space. Overall, basic characterization confirms that the TiO<sub>2</sub>@FTO in nanorod geometry having high aspect ratio have been deposited and can be further taken for checking the applications like EC, sensing, supercapacitors etc. Electrochemical studies of the TiO<sub>2</sub>@FTO sample have been carried out and discussed below for possible application as an EC electrode. Such nanoneddles can also be useful for other application like FEas has been discussed in chapter 6.

#### 3.3.2 Electrochemical activity of TiO<sub>2</sub>@FTO

The electrochemical measurement[137] has been performed in three-electrode systems through and the CV is recorded in an electrolyte of 0.1M LiClO<sub>4</sub> in acetonitrile. The TiO<sub>2</sub>@FTO electrode, when used as WE, shows its color modulation from whitish color to dark blue color when scanning from -1.8V to 0.5V which also accompanies redox peaks (Figure 3.4a). Changing oxidation state leads to change in the optical modulation in visible range and hence perceives the chromic effect. The transformation of the natural white color to dark blue color is due to the Li<sup>+</sup> ion insertion into the electrode followed by the given reaction (Eq. 3.2).

$$TiO_2 + xLi^+ + xe^- \leftrightarrow Li_x TiO_2$$
 (3.2)

Since, this above reaction shows its redox (or reversible) behavior under the positive and negative biasing and hence both EC states display the reversible nature too.[61] The CV measurement in Figure 3.4a is showing the reversible behavior of TNR electrode in the given potential window at a scan rate of 100mV/sec. Corresponding photograph of the electrode showing the two chromic states have been shown in the background of the CV graph in Figure 3.4a. The TNR electrode changes its chromic modulation to the dark blue color at the negative voltage and returns to its natural white color at the positive voltage and hence comes

in the category of cathodic EC active material. To quantitatively appreciate the color modulation, in-situ bias dependent absorption spectra have been recorded and corresponding CCr has been measured (Figure 3.4b). The inset of Figure 3.4b is showing the absorbance in the visible spectrum. The optical absorption of these two chromic states in the visible range (red and black curve of Figure 3.4b) displays only 29 % optical color which is poor. Improving such a limited optical contrast in an inorganic material remains a challenge in material like materials TiO<sub>2</sub>, ZnO etc. where the smooth, uniform, stable thin film with much higher transparency is required to obtain better EC performances. It is important to mention that TiO<sub>2</sub>, even in nanostructured form, shows poor EC modulation. To explore the possibility of other inorganic nanomaterials for better EC modulation Co<sub>3</sub>O<sub>4</sub> obtained using electrodeposition technique has been tested for this purpose. This is attempted so that the robust nature of inorganic materials can be exploited if other bottlenecks like high power requirements etc. are addressed. A successful attempt in this direction has been reported below in detail.

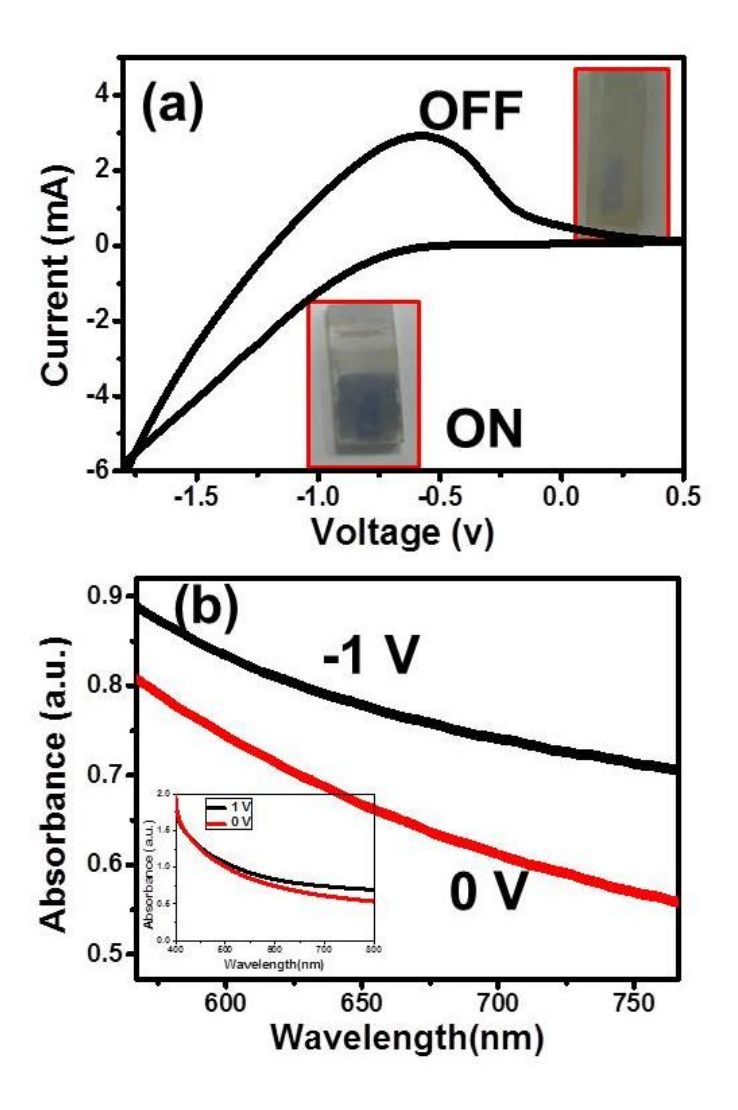


Figure 3.4: (a) CV of EC active TNR showing cathodic nature along with its whitish and bluish chromic states (actual image in background) and (b) optical absorption for colored (black curve) and bleached state (red curve) of TNR (zoomed portion in inset).

#### 3.4 Cobalt oxide

Bulk cobalt oxide is known for anodic type inorganic EC behavior. Though a robust material it does not find a place in practical EC application due to its poor performance and need of high biases. In an attempt to improve the EC performances, electrodeposition techniques have been used to obtain nanostructures of  $\text{Co}_3\text{O}_4$  on an FTO  $(\text{Co}_3\text{O}_4\text{@FTO})$  electrode in thin film form. Detailed EC performance of  $\text{Co}_3\text{O}_4\text{@FTO}$  in electrode and in a solid state device has been

investigated and very encouraging results have been obtained as discussed below.

#### 3.4.1 Characterisation of Cobalt oxide

Since, all the inorganic materials are tedious to handle for EC application and cobalt oxide too is not an exception[138]. To address these difficulties some modifications in the deposition steps, such as concentration/thickness variation, deposition techniques etc. are carried out so that different nano structure architecture can be obtained. An electrodeposition technique with controlled current has been chosen here to deposit nano-cobalt oxide over the conducting FTO coated glass substrate as per the recipe described in section 2.4.4 (chapter 2).

Constant current controlled deposition of cobalt atoms is expected to show better morphological coverage and packing. The image in Figure 3.5a of deposited thin film shows the homogenous deposition of film with very high dense microstructures. High dense film helps to make the better EC switching under the less applied voltage. Three dimension surface plot of SEM image calculated through Image J<sup>TM</sup> software kept in the inset of Figure 3.5a also reflects the high density structure formed over the substrate using chronopotentiometric deposition technique. The SEM image shows some cracks between the different grain like geometry which could cause trouble to create a smooth contact surface at the electrode-solid electrolyte interface when used in device. For better clarity on this and to know how significant these cracks are, AFM measurement on the same sample has been done (Figure 3.5b). The two images (SEM and AFM) do not show much difference in the morphology and roughness of the prepared film. The films deposited using electrodeposition technique are much adhesive to the electrode with large homogeneous surface.

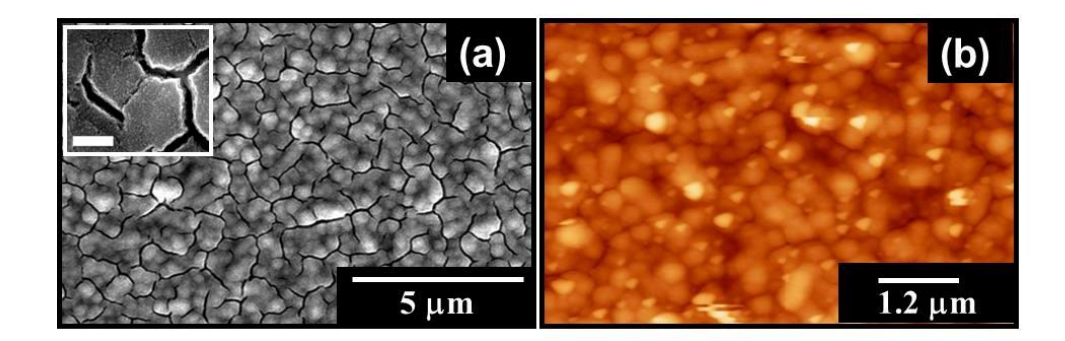


Figure 3.5: Surface morphology of electrodeposited film as observed using (a) SEM with inset showing surface profile obtained using Image J and (b) on fluorine doped tin oxide (FTO) electrode as seen using (a) SEM showing cracks (inset, scale bar: 200 nm) and (b) AFM.

Besides the morphology of electro-deposited material, it is also important to establish whether the intended film, i.e, of Co<sub>3</sub>O<sub>4</sub>, has been deposited. Some basic structural characterizations (Figure 3.6) for this purpose have been carried out which confirms the successful deposition of cobalt oxide. The XRD measurement in Bragg Brentano ( $\theta$ -2 $\theta$ ) mode has been carried out (Figure 3.6a) to confirm the deposition of cobalt oxide phase which is evident from the prominent peak of (111) plane at around 18.5° corresponding to Co<sub>3</sub>O<sub>4</sub> phase, labelled by '\*' (Figure 3.6a) as per the JCPDS no 89-1970[139]. The unmarked peaks correspond to the FTO substrate. The presence of one plane in the deposited area results from the homogeneous delineation of the Co<sub>3</sub>O<sub>4</sub> film as a result of the constant current. Additionally, a Raman spectrum in Figure 3.6b is performed to identify the vibrational modes present and is found to be in agreement with the XRD results. Various Raman peaks have been identified as those from different modes of Co and O atoms present at octahedral and tetrahedral position[140] of unit cell as found at 195 cm<sup>-1</sup>  $(F_{2g})$ , 482 cm<sup>-1</sup>  $(E_g)$ , 527 cm<sup>-1</sup>  $(F_{2g})$ , 622 cm<sup>-1</sup>  $(F_{2g})$  and 691 cm<sup>-1</sup>  $(A_{1g})$ . To further explore and understand the chemical constituents, XPS was recorded in full scan (Figure 3.6c), which affirms of Co (2p) atom, O (1s) and C (1s) and further goes for processing of individual data using standard XPS peak fitting (Figure 3.6d). Spin orbit doublet of 2p state of Cobalt, having two-fold degeneracy, goes for further splitting in 2p<sub>3/2</sub> and  $2p_{1/2}$  assigned by binding energy 782 eV and 797 eV (Figure 3.6d). The two different assigned peaks of Co (2p) contributed by the tetrahedral Co<sup>+2</sup> and octahedral Co<sup>+3</sup> of Co<sub>3</sub>O<sub>4</sub> profile. The satellite peak towards high energy sides from both sharper peaks and binding energy difference (~ 15.5 eV) of Co (2p) promises the co-existence of Co(II) and Co(III) in the material surface[141,142]. Thus, XPS result was also consistent with the XRD and Raman results which along with morphological study confirm that uniform and dense film of Co<sub>3</sub>O<sub>4</sub> has been synthesized using constant current electrochemical deposition.

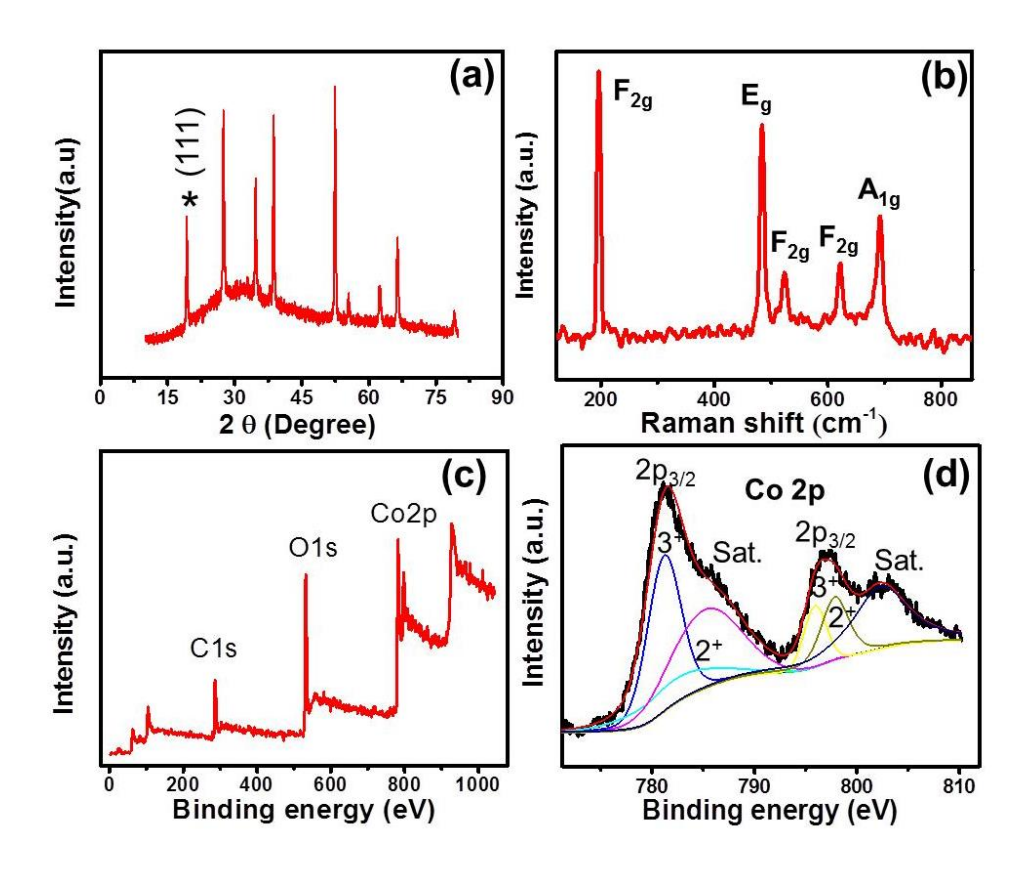


Figure 3.6: (a) X-ray diffraction pattern showing  $Co_3O_4$  peak (\*) and FTO peaks (unmarked), (b) Raman spectrum and (c, d) XPS from  $Co_3O_4$  film.

## 3.4.2 Spectroelectrochemistry of Cobalt oxide and Efficient Elctrochromism

The fabricated Co<sub>3</sub>O<sub>4</sub> film on FTO coated glass has been intended for EC application as an electrode and in a solid state device which has been tested using CV measurement (Figure 3.7a). This electrochemical

measurement has been performed in three-electrode arrangement using 0.1 M KOH (aqueous) electrolyte which contains Ag/AgCl (RE), Pt-wire (CE) and  $Co_3O_4$ @FTO as the WE.

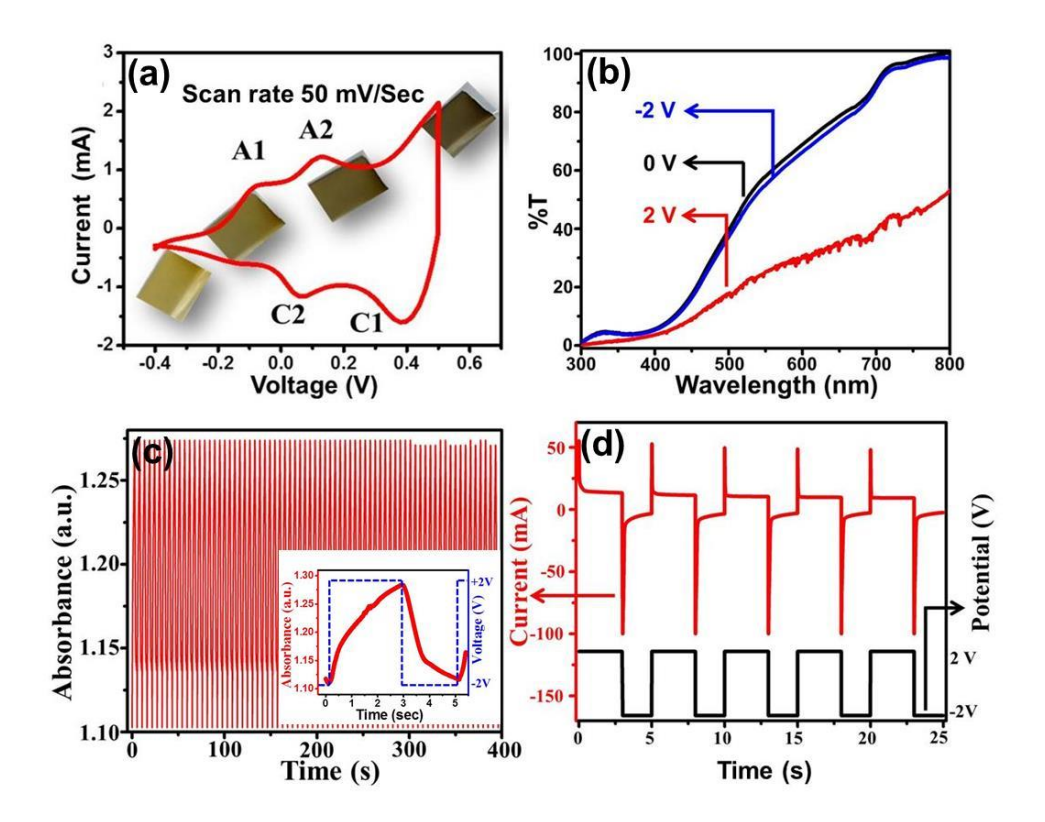


Figure 3.7: (a) Cyclic voltammogram from  $Co_3O_4$  film in 0.1M KOH electrolyte and the actual image of the electrode in the background corresponding to the applied bias, (b) bias dependent in-situ absorption spectra in an electrochemical cell, (c) absorption kinetics of  $Co_3O_4$  electrode in the same electrochemical cell having switching between  $\pm 2V$  (with one response in inset) along with its chronoamperometric response with respect to single applied voltage pulse (d).

A cyclic potential sweep applied from -0.4 V to 0.5V across the WE and RE at constant scan rate of 50 mV/s and corresponding current from the dipped area of WE was measured due to intercalation and deintercalation of  $OH^-$  ion. The CV curve (Figure 3.7a) clearly shows two pairs of redox peaks marked as (C1,C2) and (A1, A2). During the anodic scan from -0.4 V to 0.5 V, the CV curve shows two oxidation peaks of  $Co_3O_4$  named A1 and A2 at -0.08V and +0.12 V most likely due to the following redox activity.

First Anodic Peak (A1): 
$$Co_3O_4 + OH^- + H_2O \rightarrow 3CoOOH + e^- (3.3)$$

Second Anodic Peak (A2): 
$$CoOOH + OH^- \rightarrow CoO_2 + H_2O + e^-$$
 (3.4)

On the other hand, in cathodic scan, two cathodic peaks named C1 and C2 corresponding to reduction of material at two different potential 0.39V and 0.05 V is observed as a result of following redox activity:

First Cathodic Peak (C1): 
$$CoO_2 + H_2O + e^- \rightarrow CoOOH + OH^-$$
 (3.5)  
Second Cathodic Peak (C2):  $3CoOOH + e^- \rightarrow Co_3O_4 + OH^- + H_2O$  (3.6)

Two interesting observations from the abovementioned reactions are the color change and reversibility. The gradual color change from transparent yellowish to dark brown color is perceived during the oxidation of Co<sub>3</sub>O<sub>4</sub> and shown in Figure 3.7a, along with the CV cycle, and is reversible in nature, making it appropriate for device applications. During this redox reaction inside the electrochemical cell, the charge intercalation-deintercalation leads to the bleached and colored state of Co<sub>3</sub>O<sub>4</sub> between a yellowish transparent and dark brown color due to the oxidation and reduction process, as shown in the actual images of the electrode in the background of Figure 3.7a. The bias-dependent color change, during the CV cycle, has been verified by carrying out in-situ spectroelectrochemistry (Figure 3.7b) in two-electrode system in an electrochemical cell. During the oxidation and reduction process, cobalt changes its oxidation state and hence shows its EC property on transmitting the different wavelengths. Figure 3.7b shows the in-situ bias dependent transmission spectra at three different potentials 0, 2 and -2 V to quantify the reversibility of color switching. The two spectra at 0 and at -2 V perfectly match with each other, which reveal the reversible nature of the electrode. The observed appearance of the electrode can be correlated with the corresponding optical spectra (Figure 3.7b) as follows. When biased, the transmission corresponding to wavelengths beyond 500 nm decreases, making it a less-transparent (in the visible spectral range) film. Transmission spectra under the oxidation of Co<sub>3</sub>O<sub>4</sub>

at +2 V are suppressed for all wavelengths in the visible region (red curve of Figure 3.7b) and thus are perceived as dark brown in color which is reverted back to the natural transparence yellowish color under bias reversal (at 2 V). Furthermore, kinetics of in situ absorption for the 425 nm wavelength along with the applied square voltage pulse of 2V is shown in Figure 3.7c. A closer analysis of one of the cycles, shown in inset of Figure 3.7c reveals that it takes less than 2 s for the color change of the electrode at a 2 V bias which is very good in the family of metal oxides. The stability was checked for 80 such cycles and shows good cyclibility. The current response of the electrode to the applied voltage pulse for five cycles is shown in Figure 3.7d to check the current stability of the EC electrode. A negligible change in current on switching between two EC states suggests a good cyclic response within the abovementioned potential range. Moreover, its redox activity suggests that it take only 2 V bias and is electronically active too. This makes it a good candidate for integrating it with an appropriate electrode for designing a power-efficient EC solid-state device with improved coloration efficiency. In other words, a smaller voltage is required to switch and maintain a given chromic state of the electrode in the device. A good quality dense film prepared by the current controlled electrochemical synthesis helps in achieving an overall improved EC performance of the electrode. The electrode indeed can be integrated to make a solid state ECDs as has been reported in chapter 4.

#### 3.5 Prussian blue

Prussian blue (PB) is a co-ordination network compound (CNC), used for various applications like sensors etc. is also known for its EC properties[124]. It is an electrochemically active material but not a very good material for EC applications due to its poor optical modulation. There are certain qualities of PB that still make it a potential material of interests which include its capability to exhibit three EC states namely in blue (Prussian blue), light green upon oxidation (Berlin green) and transparent on reduction (Prussian White)[143,144]. This property can be of potential application only if other bottlenecks can be removed

which are related to limited stability and poor CC. One such attempt has been taken successfully by combining it with other suitable CE has been discussed in chapter 4. Prior to that basic electrochemical and EC properties have been studied along with routine characterization here.

#### 3.5.1 Characterisation of Prussian blue solid thin film

Electrodeposition technique has been used to deposit PB film on an FTO electrode by a recipe described in section2.4.5 (chapter 2). The blue-colored film was then analyzed using SEM and Raman spectroscopy techniques to ensure the structure. The SEM image (Figure 3.8a) shows a homogeneous deposition of film over FTO electrode which is good for EC application as it can make better contact with the electrolyte. Further to characterize the material for knowing its material composition and property, Raman spectroscopy has been carried out using 633 nm excitation (Figure 3.8b). The Raman spectrum of PB is showing peaks at 253 cm<sup>-1</sup>, 500 cm<sup>-1</sup> and 2125 cm<sup>-1</sup> which is in agreement with reported modes of PB (marked as \*)[145].On successful preparation of PB@FTO electrode, its EC properties have been studied as discussed below.

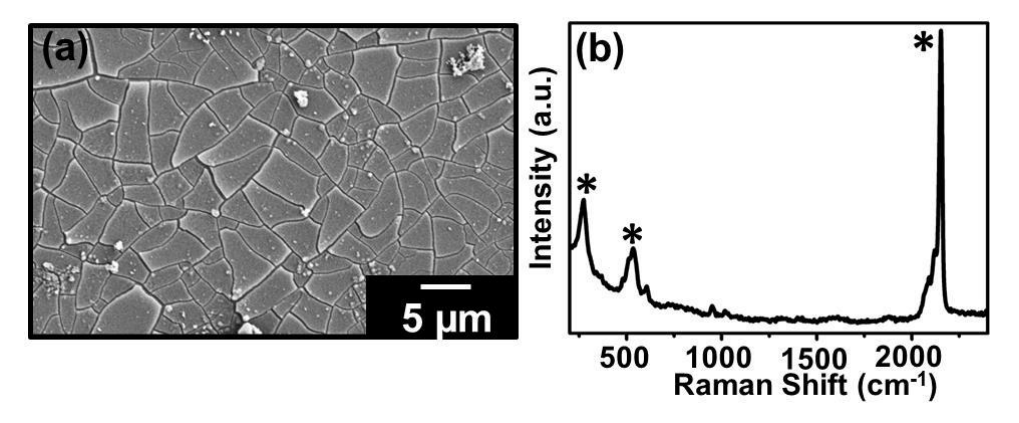


Figure 3.8: (a) SEM image and (b) Raman spectrum of as-prepared PB thin film on FTO substrate.

#### 3.5.2 Electrochemistry of PB thin film

The electrochemistry of PB@FTO has been performed in KCl electrolyte which produces  $K^+/Cl^-$  ion to activate the charge intercalation de-intercalation when used as the WE (Figure 3.9a). The usual three-electrode arrangement has been used for CV measurement as described

in section 2.3.2 (chapter 2) and the corresponding CV curve has been recorded in its typical potential window of -0.2V to +1V (Figure 3.9b). The whole CV curve has been obtained at a scan rate of 50 mV/sec and displays two oxidation and corresponding two reduction current peaks labeled by (A3, A4) and (C3, C4) respectively for the anodic and cathodic scan. It is interesting to notice that its redox behavior is observed in both potential directions (positive and negative) making it a potential CE for cathodic as well as anodic type of EC material. The oxidation of PB converts it into Prussian green (PG) whereas it reduces to Prussian white (PW) (transparent) to display the reversible change into all three chromic states under the possible redox reaction. The same can be understood easily with the help of Eq. 3.7 as shown below.

$$PG \leftarrow \frac{\text{oxi.}}{-e} PB \xrightarrow{\text{red.}} PW$$
 (3.7)

The above-mentioned EC modulation has been studied using in-situ bias dependent absorption spectroscopy by biasing the as-prepared PB@FTO electrode as per the polarity shown in Figure 3.9c. Figure 3.9c is showing the absorption spectra recorded at three different voltages 0V, -2V and +2V and shows absorption properties of as-prepared PB, PW (reduced PB) and regained PB (oxidation of PW). A reversible color modulation can be appreciated from the fact that absorption curves for as-prepared (0V) and under -2V bias are similar. Further, chronoamperometric measurement has been carried out to check the PB@FTO electrode performance for its device application under the given potential square pulse between +2V and -2V (Figure 3.9d). The given potential pulse has been applied for 10 sec duration and corresponding current has been measured to calculate the charge injected during the chromic modulation, shown in Figure 3.9d. To perform optical measurement with respect to the applied potential pulse, the electrode has been taken for the in-situ absorption spectroscopy at fix 650 nm wavelengths which shows the EC switching performance and stability (Figure 3.9e). The continuous absorption cycle measurement for 300 sec in Figure 3.9e is showing the gradual decrement in the

absorption value indicating a poor stability of electrode toward EC behavior. One of these cycles has been closely seen to estimate the switching time which comes out to be ~ 8s (Figure 3.9f). Overall, high switching time with poor stability cannot be used alone neither as an EC electrode nor in a device however it can be improved when used in combination with other suitably designed electrodes upto an extent to be used in a solid state EC. The device design, recipe of fabrication and detailed EC properties have been studied and discussed in chapter 4.

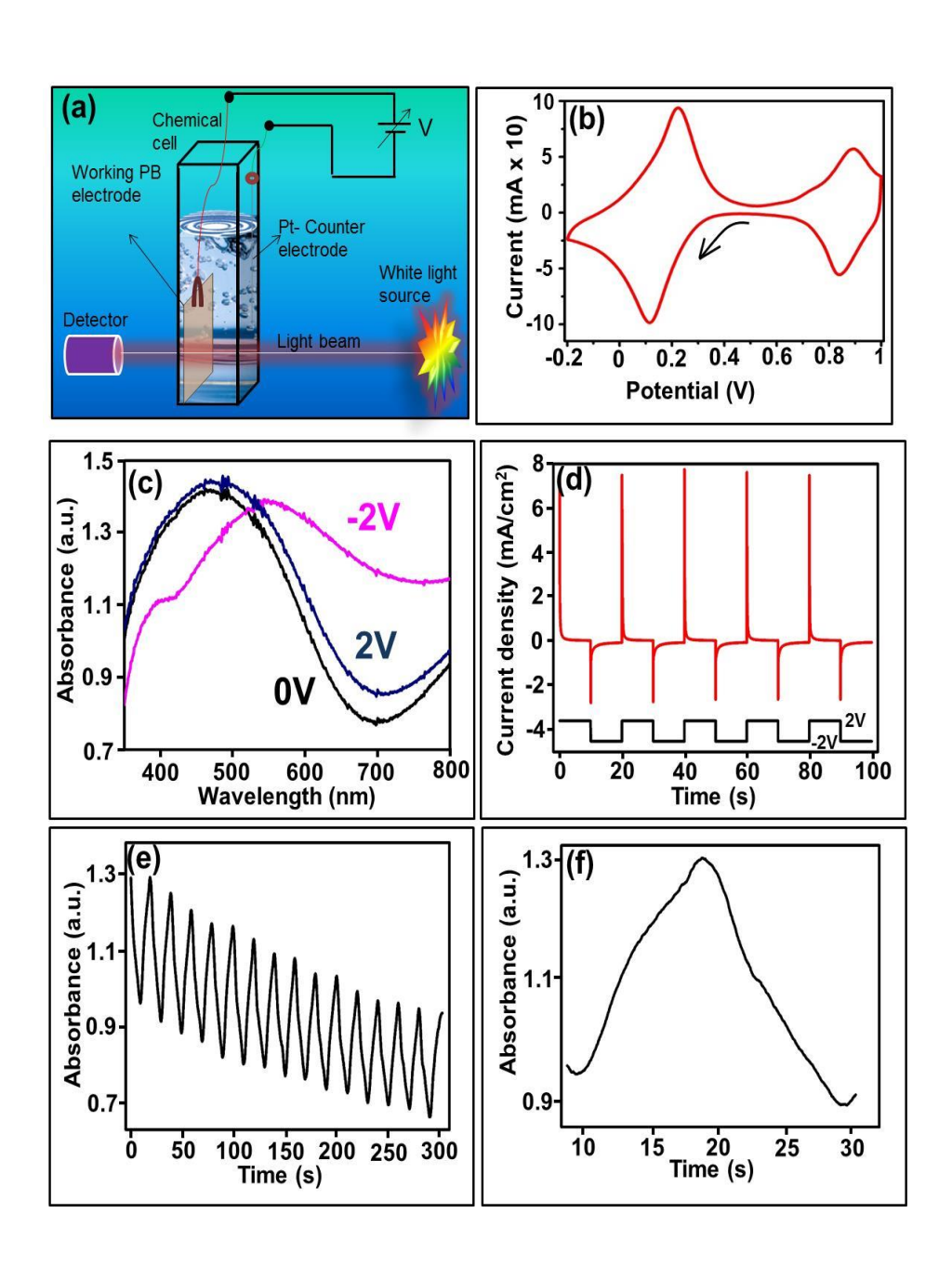


Figure 3.9: Schematic representation of spectroelectrochemisty of PB@ITO electrode in three electrode system (a), CV measurement of PB electrode in KCl electrolyte (b), In-situ Optical spectroscopy of PB electrode under the effect of external biasing (c), Chronoameropetric measurement of current with respect to the applied potential pules toggling between -2V to +2V (d), Switching absorption cycle of PB electrode for coloration and bleaching state (e), Zoomed portion of one complete absorption cycle (f).

#### 3.6 Summary

Nanostructures of some Transition metal oxide (TMO) and PB were prepared on FTO using an appropriate recipe. EC properties of these electrodes after proper characterization were studied and their merits and demerits were underlined for further studies and possible applications. The various TMO including NiO, TiO<sub>2</sub>, Co<sub>3</sub>O<sub>4</sub> etc. has been divided into cathodic and anodic EC active material. The films prepared by hydrothermal process showed more roughness at the surface of the film and the film are not stable. On the other hand, electrodeposition techniques is making smooth, more adhesive, more homogenous, dense thin film of cobalt oxide. Therefore, the electrodeposition technique will be adopted for further studies related to EC investigations as it showed quick switching response for optical modulation. The redox activity of Co<sub>3</sub>O<sub>4</sub> makes this material more important to act as a CE for improving the ECDs performance. This good result of inorganic Co<sub>3</sub>O<sub>4</sub>, prepared by using the electrodeposition technique, can be taken for inorganic as well as organic EC material for making the hybrid device. Moreover, these inorganic electrodes can be used with another organic EC electrode for improved hybrid ECDs.

### **Chapter 4**

# All-Inorganic & Hybrid EC Solid State Device

This chapter describes the study of solid state ECDs fabricated in two paradigms namely, inorganic/organic ("hybrid") and inorganic/inorganic ("all-inorganic"). Inorganic electrodes, reported in previous chapter have been used to fabricate these devices. Combination of appropriate electrodes in double layer geometry, apart from the individual species, makes it favorable in many ways to improve the device performance. The performance of the finished device with similar or dissimilar materials' combination has been checked through switching time, switching speed, CCr and coloration efficiency. In-situ spectroscopy techniques like UV-Visible and Raman have an extraordinary advantage to understand and to explain the mechanism for coloring and bleaching state of EC active materials. On the whole an "all-inorganic<sup>5</sup>" and "hybrid<sup>6</sup>" solid state ECDs have been successfully fabricated which shows performance for real applications.

<sup>&</sup>lt;sup>5</sup> Devesh K Pathak et al, ACS Appl. Electron. Mater. 2, 6, (2020) 1768–1773

<sup>&</sup>lt;sup>6</sup> Devesh K Pathak et al, Appl. Phys. Lett. 116,(2020) 141901

#### 4.1 EC Double layer device and Engineering

An EC double layer (EDL) device is prepared by choosing two suitable layers out of which at least one layer is made up of EC active material and both should have complementary redox activity. The device engineering for practical purpose is implemented in generic cross bar geometry using the flip chip method[50,64]. The material is coated over the conducting transparent FTO/ITO substrate using appropriate techniques for achieving the homogeneous thin film to make better contact with the electrolyte ions. Before preparing the ECDs, every WE is passed through testing step for knowing its chromic modulation under the effect of redox reaction. The redox activity is checked in an electrochemical cell in three-electrode system. The varying potential is applied to the material for knowing its redox activity to check intercalation/de-intercalation of ion and consequent color change, if any. This step is followed by identification of appropriate CE for the device fabrication. Here the redox activity and consequent color modulation (or otherwise) are the important facts that are used to design the solid state device.

Inorganic materials, compared to organic ones[60,138], have their own limitations when it comes to their application in solid state device and is one of the challenges in this area and being addressed worldwide. Using a single layer inorganic material is virtually impossible to realize a solid state ECDs with even nominal performance. To improve the EC performances of the finished device, different design paradigms like all-inorganic, double layer hybrid device, better coloration efficiency with greater conductivity/ electrolyte ion insertion etc. are attempted. In this attempt, a small step has been implemented here by using a packed and adhesive EC electrode (of Co<sub>3</sub>O<sub>4</sub> nanostructure), obtained by electrodeposition (section 2.1.2 & 2.4.4) to make the EDL device. EC performance of the so designed device using combination of nano-Co<sub>3</sub>O<sub>4</sub> (inorganic) material to EV (organic) and PB (inorganic) have been investigated and discussed below.

## 4.2 Nano-Cobalt Oxide/Viologen Hybrid Solid State Elecorochromic Device

As mentioned earlier, viologens are electron acceptor EC materials[143] has been combined with the Co<sub>3</sub>O<sub>4</sub>@FTO electrode to make a solid state ECDs. Prior to be finished as a device the compatibility of the two materials (viologen and Co<sub>3</sub>O<sub>4</sub>) has been tested using control experiment. Figure 4.1 shows CV response of both the materials along with corresponding color change when used as independent electrodes to suggest that the redox behavior of the two electrodes are complementary to each other as the two electrodes show redox activity at opposite polarity. The bias dependent redox behavior also accompanies a color change (in anodic scan) which makes it an EC active CE (Figure 4.1a). Since both the electrodes are EC active materials, an improvement in CC is expected. The EV shows EC behavior under cathodic scan (Figure 4.1b) and changes color from transparent to blue. During the color change scan, the transparent state of EV<sup>+2</sup> transforms to its reduced form EV<sup>-+</sup> showing blue colour and reversibly comes into its natural transparent state on further oxidation. Similar color switching is also observed when EV film is obtained on a FTO coated glass (to get EV@FTO electrode) and can be used for device fabrication purpose. In other words, if the other electrode, by some means, has the ability to show the chromic behavior under oxidation, must be installed with the viologen to improve the EC property of both materials. The inorganic nano-Co<sub>3</sub>O<sub>4</sub> material, which itself is changing color in oxidation, can be taken as supporting electrode to enhance the coloration efficiency and CCr of individual/single electrode based device.

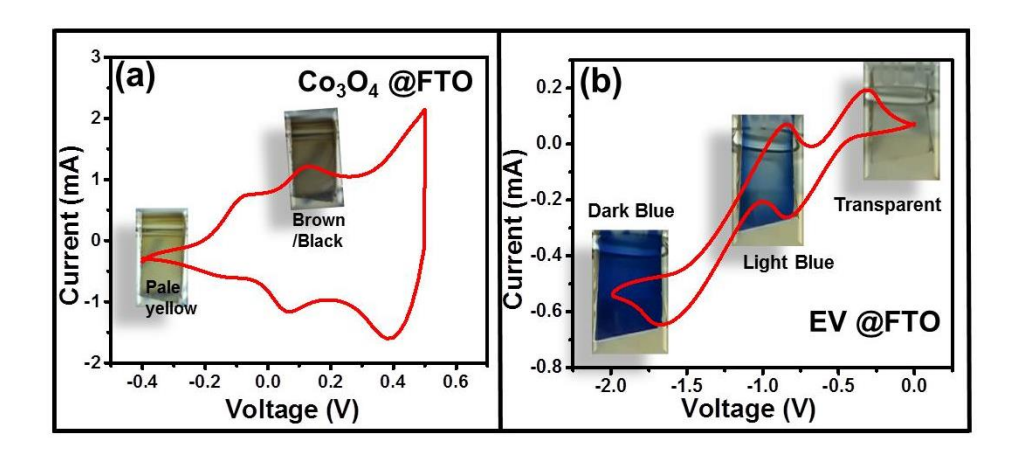


Figure 4.1: (a) CV curve of Co3O4@FTO electrode with changing EC state from pale yellow to brown/black under anodic scan and (b) CV curve of EV solution at bare FTO substrate with changing colour from transparent to blue color under cathodic scan.

#### 4.2.1 Device fabrication and characterisation

A solid state ECDs has been fabricated using the EV@FTO and  $Co_3O_4$ @FTO electrodes in cross-bar geometry by flip-chip method and schematically shown in Figure 4.2. Following steps were used to prepare this device which is also shown in the schematic in Figure 4.2.

- ➤ FTO coated glass substrate is used for preparing the electrode of materials 'nano-Co<sub>3</sub>O<sub>4</sub>' and 'EV dibromide'.
- ➤ For preparing the first electrode, electrodeposition method with constant current has been chosen to deposit the Co<sub>3</sub>O<sub>4</sub> material in nano regime. The deposited nano Co<sub>3</sub>O<sub>4</sub> materials appear pale yellow and convert to its black/brown colour during oxidation process.
- A transparent double-sided cello tape pasted over all four edges of deposited area (in a square manner) and left empty in the middle portion for filling the other EC active material.
- > In the meantime, other EC active material, named EV dibromide in PEO matrix, has been formed and then 50 μl of EV gel drop casted over the middle vacant portion of doubled sided tape. This is the above-mentioned EV@FTO electrode.

- At last, the same geometrical FTO substrate, from conducting side, put up over the last prepared electrode and pressed for a while to insure the better connection between the two substrates through EC active gel.
- ➤ The device finally is ready for testing.

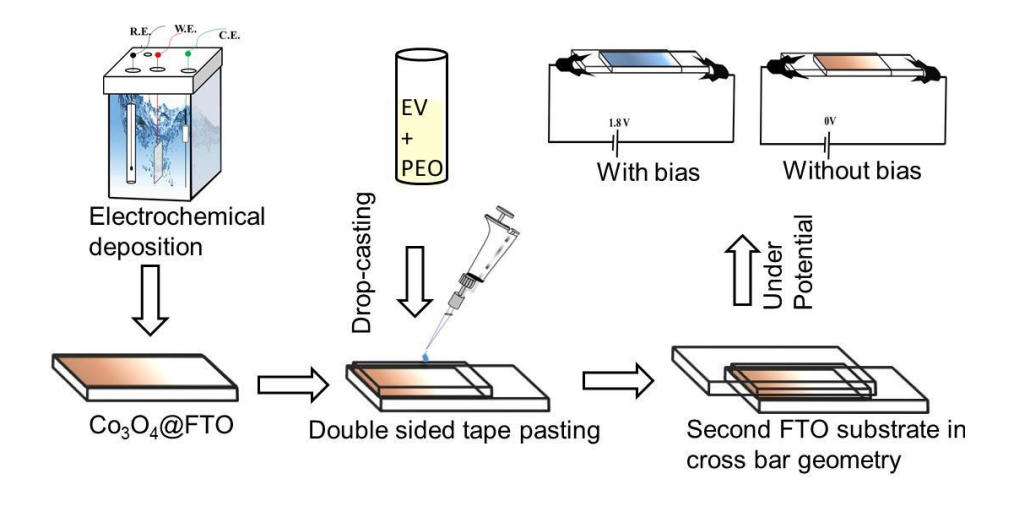
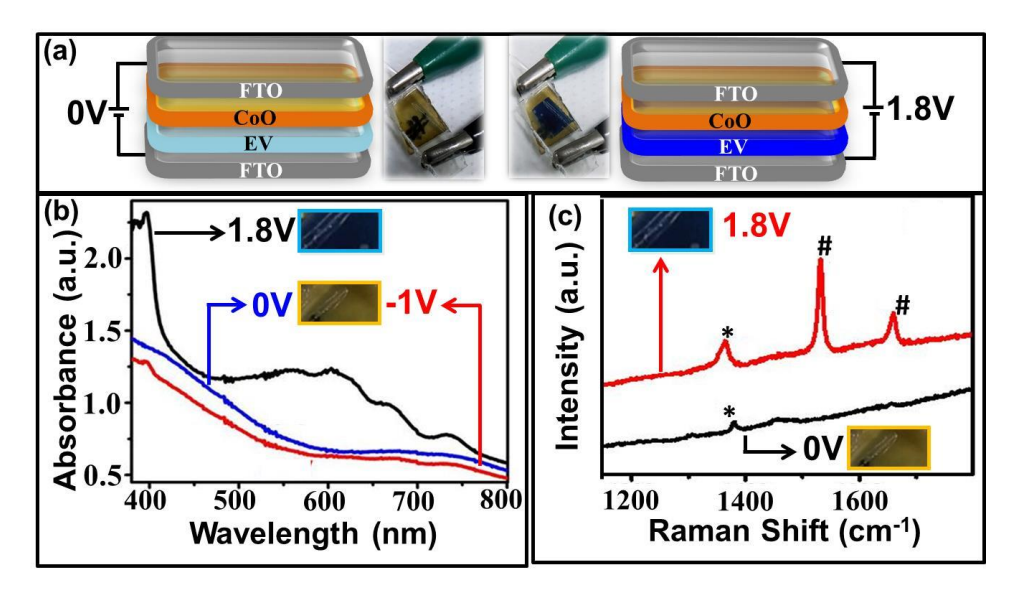


Figure 4.2: Schematic representation of fabrication process involved in making solid-state hybrid inorganic-organicECDs.

The fabricated device is in a cross-bar stacked geometry as shown in Figure 4.3a. During the measurement, the bias has been applied with the  $\text{Co}_3\text{O}_4$ @FTO electrode hooked to positive and other one hooked to the negative terminal. The finished device appears 'pale yellow' under no applied bias which changes to 'blue' with the application of a bias of 1.8V (Figure 4.3a). Corresponding UV-Vis spectra of the device under different bias conditions are shown in Figure 4.3b. With an application of 1.8V bias (positive to  $\text{Co}_3\text{O}_4$ @FTO electrode), the overall absorption increases throughout the entire wavelength range with an extra absorption around yellow region (black curve, Figure 4.3 b). An extra increase in yellow (mixture of red and green) means that only blue component remains less absorbed hence gives the dark blue (non-transparent) appearance of the device. Under this bias condition,  $\text{Co}_3\text{O}_4$ @FTO electrode, being connected to positive, gets oxidized as the reduction of EV<sup>+2</sup> to EV<sup>++</sup> on the other electrode (eventually connected to

negative voltage) take place which gives the well-known blue appearance.

The colored state of the device can be reversed (similar to the situation in electrochemical cell, Figure 4.1) on the application of -1V bias (red curve, Figure 4.3b). A significant change appears in absorption spectrum nearby 600 nm (400 nm) when positive (negative or no) bias is applied with a contrast of more than 60% for 600nm wavelength. This along with other device parameters has been discussed below in detail. This prominent change in absorption spectra at these two wavelengths is dominated by the blue colour of reduced EV<sup>-+</sup>. Whereas, the spectrum changes throughout the wavelength range, reveals that the Co<sub>3</sub>O<sub>4</sub> is showing self-coloration effect and working as a well supporting material for helping to reduce EV<sup>+2</sup> speedily. As mentioned above, the bias induced color change in EV and Co<sub>3</sub>O<sub>4</sub> electrodes is governed by corresponding redox activity. The same can be confirmed using in-situ Raman spectroscopy (Figure 4.3c). The bias dependent Raman spectrum shows the EV<sup>+2</sup> Raman vibration mode of EV di-bromide near 1381cm<sup>-1</sup> when the device is unbiased (black curve, Figure 4.3c). Whereas, Raman spectrum of the device under +1.8V bias show peaks at 1529 cm<sup>-1</sup> and 1656 cm<sup>-1</sup>, a signature of reduced state of viologen molecule, which is also responsible to display the blue colour of device[58]. On the whole, bias dependent in-situ Raman and UV-Vis spectroscopy confirms the redox driven color switching of the solid state ECDs.



**Figure 4.3:** (a) Schematic representation and actual images of device in cross bar geometry with and without bias, (b) in-situ absorbance spectra of fabricated device under three biasing states, (c) in-situ Raman spectroscopy of device 'with' and 'without' bias (1.8V) condition

#### 4.2.2 Electrochromic performance of Device

For application of a solid state device, optimal performance is desired which is understood in terms of performance parameters like cycle life, CCr and coloration efficiency. To check the performance of the device successfully fabricated above, various parameters have been measured by switching the device using square voltage trains toggling between +1.8 V (for 2 s) and -1V (for 3 s). The applied biasing and corresponding kinetics of absorption spectrum (for 375nm) has been tested for 600 seconds or 120 cycles, shown in Figure 4.4a. This spectrum is showing little variation in absorbance for more than 100 cycles meaning a good stability of the device. It is also important to mention here that there is only a little variation in the minimum absorption (from 1.5 to 1.6) after 400 s which is not much as the value in the other state and remains at 2.3. This small variation is not an uncommon observation from ECDs when switched consecutively too fast and does not affect the performance as none of the practical situations desire such a fast sequence of color switching of an ECDs. This absorbance switching of the complete hybrid device is excellent as compare to a device fabricated using only individual constituents. A zoomed portion, showing one of

the absorption switching cycles, as shown in Figure 4.4b, has been used to estimate the switching times of the device yielding a transparent to blue switching time of 500 ms and switching time from blue colored state to bleached state takes 2.3 s. The sub-second coloring response from EV family of EC materials is one of the fastest which is coming due to the role of good quality auxiliary nano-Co<sub>3</sub>O<sub>4</sub> electrode which required lesser oxidation potential to reduce EV<sup>+2</sup> and to bring itself in the colored state.

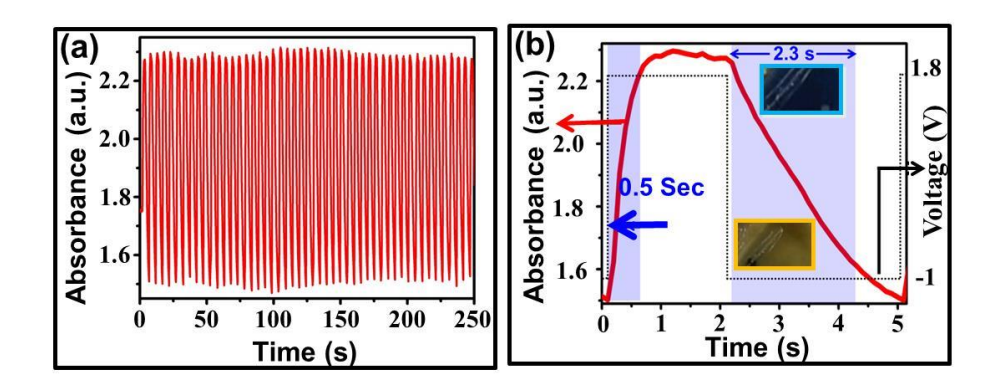


Figure 4.4: (a) Absorption switching kinetics of device with switching voltage from -1V to 1.8V of fabricated device, (b) color (ON) and bleached (OFF) representation through one absorption cycle.

Like the absorption switching shown in Figure 4.4a, cyclic choronoamperometric response in Figure 4.5a further validates the reversibility and stability of device for five cycles for 25s. An infinitesimally small change in the oxidation and reduction current is observed with an applied voltage pulse showing good stability of the device. A finite current can be seen flowing through the device in the forward bias condition (+1.8 V), which is a consequence of slow discharging of the material. It is important here to mention that the device behave as a diode shown (appendix A1), and therefore, the corresponding unequal currents are observed in the two color states of the device. Coloration efficiency ( $\eta_{ce}$ ) is another vital parameter to access the device performance and is defined by Eq. 1.4, mentioned in section 1.3.5.4 (chapter 1).

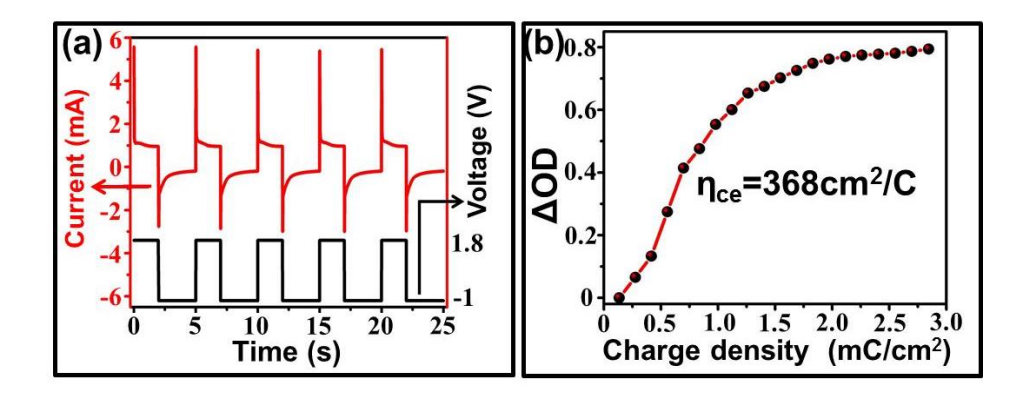


Figure 4.5: (c) current response of the devices under 1.8V/-1V potential pulse, (d) Optical density variation as a function of charge density.

Thus, in order to calculate the coloration efficiency of device, OD has been plotted with respect to charge density in Figure 4.4d and calculated to be 368cm<sup>2</sup>C<sup>-1</sup>. This high coloration efficiency is likely due to the fact that both the counter ions used in the device are EC in nature showing color switching at complementary voltages as mentioned above. This is also possible due to the reduction in redox potential of Co<sub>3</sub>O<sub>4</sub> electrode used for supporting EV electrode. Thus a smaller voltage is required to switch and maintain a given chromic state of the electrode in the device. In other words, the two materials support each other's redox activity to yield improved CCr at smaller bias values. A good quality dense film prepared by current controlled electrochemical synthesis helps in achieving an overall improved viologen (organic) based ECDs. The overall performance of the device is better than the ones from the cobalt oxide based family as can be seen from the list of comparison in table Table 4.1. The mutual complementary nature of the EC pairs, where one shows EC performance in the positive bias while the other in the negative bias, helps improving the overall performance of the device in the solid state. The device designed in such a manner not only makes the device complete but also helps in achieving a liquid electrolyte free ECDs. In other words, the two materials support each other's redox activity to yield CCr of 63% at less than 2 V. A film prepared by current controlled electrochemical synthesis helps in fabricating a hybrid solid state ECDs without compromising the switching parameters as

compared to the case of the electrochemical cell without the use of a liquid based electrolyte for actual usage in smart windows.

Table 4.1: Comparison table showing the performance of various ECDs containing  $Co_3O_4$ .

S. No	Materia 1	Synthesis method	Colour contrast (%)	Switchin g speed (s)	Coloura tion efficien cy (cm <sup>2</sup> /C)	Reference
1.	Co <sub>3</sub> O <sub>4</sub>	Electrodep osition	66	0.5	368	This work
2.	Co <sub>3</sub> O <sub>4</sub>	Electrodep osition	NR	3	NR	L. Wang et al [3]
3.	Co <sub>3</sub> O <sub>4</sub>	Nebulizer spray technique	20	2.5	6.8	C. R. Dhas et al[4]
4.	Co <sub>3</sub> O <sub>4</sub>	Chemical vapor deposition	NR	2.5	30	X.H. Xia et al[5]
5.	Cr doped Co <sub>3</sub> O <sub>4</sub>	Nebulizer spray technique	38		47	C. R. Dhas et al[6]

## 4.3An "all-inorganic" Nano-Cobalt Oxide/Prussian Bule ECDs

It is clear from the above discussion that with emerging materials, revisiting electrochromism from inorganic materials is likely to deliver an improved device if designed properly, as they have some advantages that remained unexplored because of some disadvantages[52,65,146]. Since, the organic ECDs got much attention even though they are less robust than the inorganic materials, because the latter showed poor switching times, higher operation voltages, and low coloration efficiency. The robust behavior, which is superior to their organic

counterparts, can be exploited to yield a very good solid-state ECDs if other drawbacks of inorganic materials are addressed. Designing the materials and considering device geometry, appropriately combining two mutually supporting materials can help in achieving an "all-inorganic" ECDs analogous to all-organic device. If designed properly, an improved solid-state application-oriented ECDs can be fabricated.

An "all-inorganic" fast, robust and power efficient solid state ECDs has been realized by using the nano-Co<sub>3</sub>O<sub>4</sub> electrode, mentioned in section 3.4, with PB which is also an EC active material. The Co<sub>3</sub>O<sub>4</sub>-PB combination has been chosen due to their complementing redox behavior. The inorganic PB has been known as a material exhibiting EC phenomenon since 1978 and widely understood for its CNC that changes its appearance from blue (PB), to light green upon oxidation (PG) and to transparent on reduction (PW), as discussed in detail (chapter 3). Similarly, cobalt oxide shows EC properties on positive bias (chapter 3). Therefore, both of them are gaining special attention because of the ability to modify their structure and adopt different architectures for device fabrication. Moreover, they are complementary to each other from a conductivity type point of view thus hinting at a possible combination for better performance. Moreover, these above-mentioned materials from different domain can be shown excellent EC property in an electrochemical cell. This is where the real challenge is faced and the same is addressed through various device design paradigms including all-organic and hybrid devices. Similarly, a new "all-inorganic" solidstate device design paradigm can be explored utilizing the advantages of inorganic materials, which can also be used for applications beyond electrochromism.

#### 4.3.1 Electrochemistry of PB- and Co<sub>3</sub>O<sub>4</sub>- electrodes

From the electrochemical measurements, it is clear that PB- and  $Co_3O_4$  electrodes are complementary to each other and thus a solid state device can be designed using them. Prior to device fabrication, the two electrodes ( $Co_3O_4$ @FTO and PB@FTO) has been tested in a liquid

electrolytic medium as discussed below. As-prepared Co<sub>3</sub>O<sub>4</sub> and PB electrodes on FTO substrate have been put in an electrochemical cell, containing 1M KCl as an electrolyte, with Co<sub>3</sub>O<sub>4</sub> (PB) is connected to negative (positive) terminal of a battery as shown in the schematic Figure 4.6a and the actual photographs under different bias conditions are shown in Figures 4.6b to 4.6d. The electrodes have been outlined with dotted lines, electrolyte has also been marked with blue dotted line and common area (overlapping area) of both electrodes has been highlighted for clarity. Schematic illustration of the setup used is depicted in Figure 4.6a indicating bias connections of electrodes with the battery i.e. Co<sub>3</sub>O<sub>4</sub> electrode is connected to negative and PB electrode is hooked to positive terminal of a battery. Under no bias condition (i.e. at 0V), with the yellowish transparent (Co<sub>3</sub>O<sub>4</sub>) and blue (PB) separate electrodes, the combination appears blue initially (Figure 4.6b). With a bias of 2V, (Figure 4.6c), common area of both electrodes turns greenish as a positive bias oxidizes PB to its green colour while appearance of Co<sub>3</sub>O<sub>4</sub> remains unchanged. This can be further explained based on CV of these electrodes later on. Further, by applying -1.5 V bias the combination appears light brown likely due to corresponding redox changes. To investigate the redox activity of two electrodes, and confirm its compatibility for a possible ECDs, CV (CV) has been carried out (Figure 4.6e &f) in an electrochemical cell. The CV of Co<sub>3</sub>O<sub>4</sub> electrode (Figure 4.6e) in 0.1 M aqueous KOH shows two anodic (cathodic) peaks as a1 and a2 (c1 and c2) appearing only in positive voltage range indicating its "p type" nature. On the other hand, the CV of PB electrode (Figure 4.6f) in 0.1 M aqueous KCl shows anodic peaks as a3 & a4 and cathodic peaks as c3 & c4 while scanning reversibly in the direction of arrow. Its redox behavior is observed in both potentials directions (positive and negative). The electrochemistry electrochemical work station is designed for these two individual electrodes in the well-defined pattern as described in section 2.3. As mentioned above, the Co<sub>3</sub>O<sub>4</sub> and PB electrodes can be combined together in a solid-state device that may lead to a device to show multi-colour.

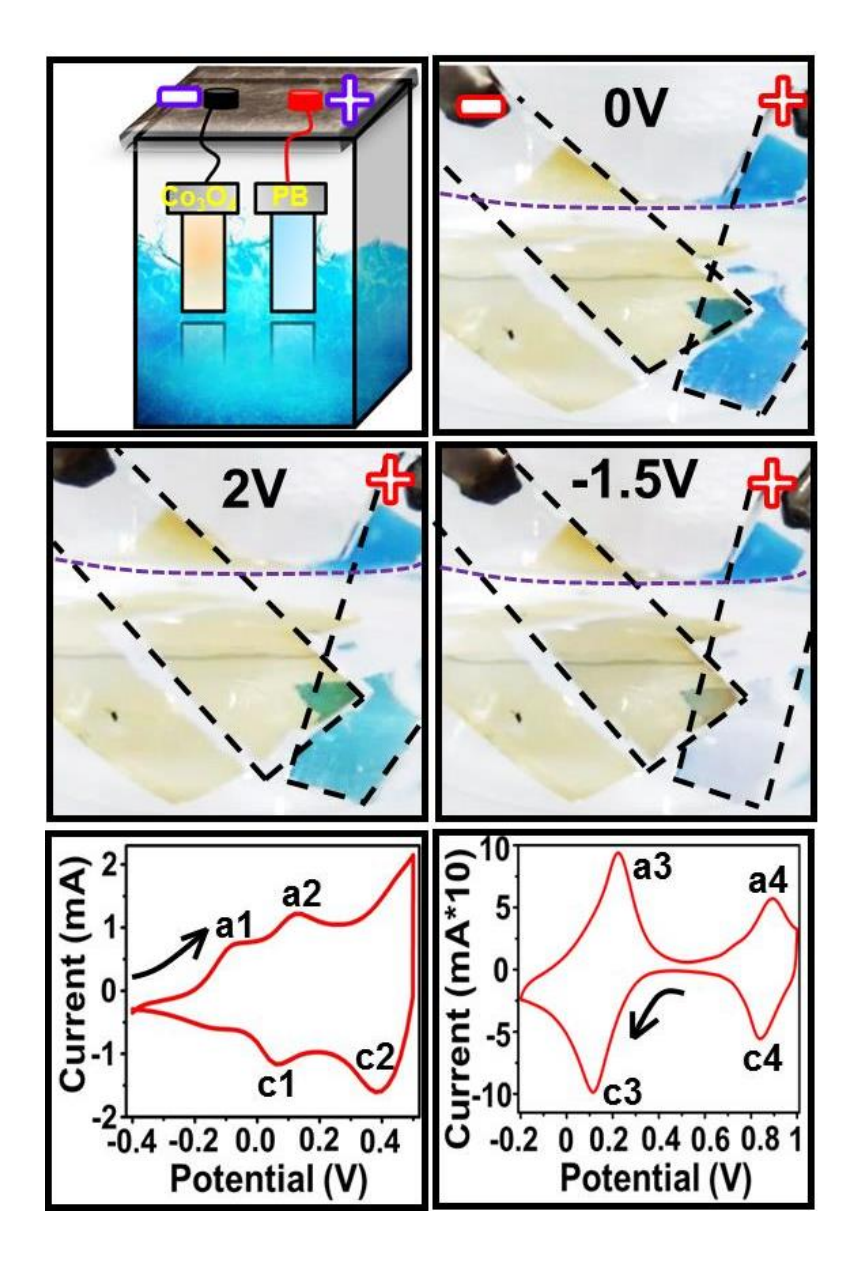


Figure 4.6: (a) Schematic illustration of experimental arrangement showing Co<sub>3</sub>O<sub>4</sub>and PB electrodes dipped in an electrochemical cell, (b-d) with actual images of the set up under different operational conditions and cyclic voltammetry curves of (e) Co<sub>3</sub>O<sub>4</sub>and (f) PB electrodes.

#### 4.3.2 Device fabrication and Characterisation

A solid-state device comprising of  $\text{Co}_3\text{O}_4$  and PB has been fabricated with a gel electrolyte of  $\text{LiClO}_4$  in PEO matrix filled in between the two electrodes so that the solid state device mimics the situation similar to one in Figure 4.6. Following step-wise description of recipe was followed to prepare the device.

- ➤ Both as prepared electrodes of PB and Co<sub>3</sub>O<sub>4</sub> have been sandwiched together with a double sided tape.
- ➤ A 5wt% PEO is dissolved in Acetonitrile (ACN) and a mixer of 1M LiClO<sub>4</sub> in ACN has been prepared. To make a gel electrolyte PEO gel was mixed with solution of LiClO<sub>4</sub> in 2:1.
- As-prepared gel electrolyte is used as electrolytic layer as shown in schematic (Figure 4.7) and the device is ready to use.

A schematic of the fabricated device along with its real images in various bias states are shown in Figure 4.7 with PB (Co<sub>3</sub>O<sub>4</sub>) electrode connected to positive (negative) terminal of the battery in all the three conditions. Initially, the unbiased device appears blue (Figure 4.7a) with original colors of as-deposited Co<sub>3</sub>O<sub>4</sub> and PB films on FTO substrate. A biasing of 2V turns device into green appearance (Figure 4.7b). This is likely due to oxidation of only PB electrode with Co<sub>3</sub>O<sub>4</sub> electrode remaining unchanged similar to the situation shown in Figure 4.7c. Further on reversing the bias with 1.5 V yields a brown color to the device most likely due to reduction of PB and oxidation of Co<sub>3</sub>O<sub>4</sub> electrode as discussed above (Figure 4.6d). Colour changes occur due to redox processes of both electrodes, PB and Co<sub>3</sub>O<sub>4</sub>, during EC reactions can be understood from the reactions (Eq. 3.3 to 3.6 & 3.7).

It is also clear that the EC properties of individual electrodes are responsible for multi-colour exhibition by the solid state device. Dynamic doping, a well-known concept in molecular/organic electronics which changes redox state of materials' due to the applied potential is responsible for such color change. This change in redox state of the material changes its optical property in EC materials. A correlation of the above-mentioned bias dependent color modulation with corresponding optical spectral response needs to be studied to establish the exhibited device color change.

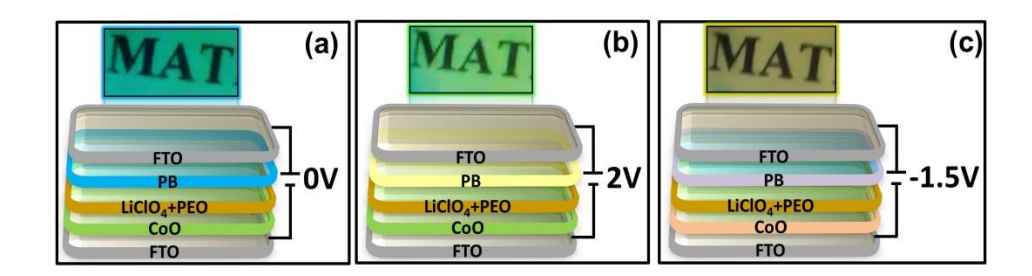


**Figure 4.7:** Schematic illustration of fabricated device in (a) unbiased state (0 V) and biased with (b) 2 V and (c) -1.5 V.

To quantify observed colour switching of the device, in-situ bias dependent visible spectra of the device have been taken in various states as shown in Figure 4.8a with its real images. The spectrum from the unbiased device in Figure 4.8a shows a dip in absorbance spectrum near 500 nm and appears blue. On biasing the device with 2V in Figure 4.8a(ii) and subsequently with -1.5 V (Figure 4.8a(iii)) turns the device appear green followed by brownish yellow. The greenish color can be understood from the observed absorbance minima at ~550 nm whereas little absorbance of most of the visible spectrum (Figure 4.8a(iii)), except blue, explains why the device should look yellowish under -1.5V bias. All these colors can be understood quantitatively through CIE (Commission Internationale de I' Eclairge International Commission on Illumination, 1976) color chart (Figure 4.8b) of fabricated device with photographs of device in all states on the image and their representation by (u', v') coordinates.

A direct correlation between bias dependent in-situ optical spectroscopy, visible color switching and the mutually complementary redox activity of Co<sub>3</sub>O<sub>4</sub>/PB bilayer device confirms the redox mediated color modulation and thus a successful fabrication of ECDs in solid state form capable of showing multi-color behavior. Further investigations are needed to understand the EC performance of the device to judge its applications suitability.

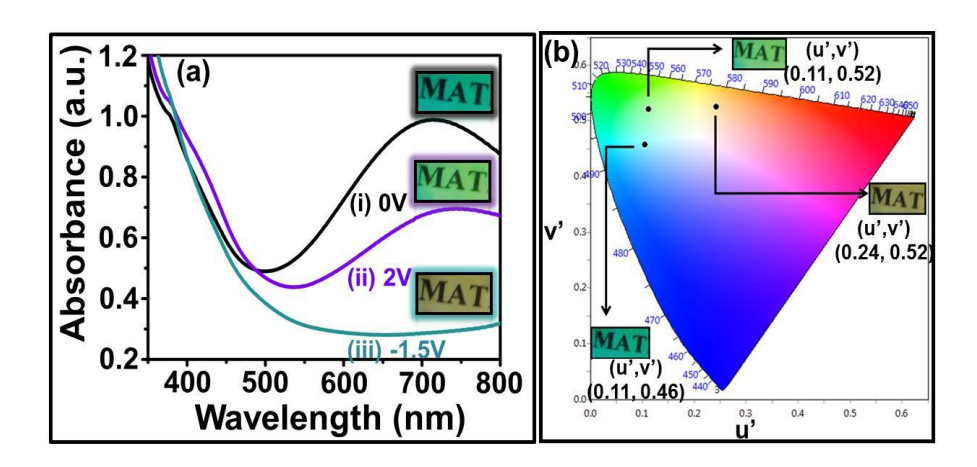


Figure 4.8: (a) In-situ bias-dependent optical absorption spectra from device under different bias conditions (i)-(iii) along with the actual image of device (insets) and (b) representation of each state on CIE diagram.

#### 4.3.3 Performance of the all-inorganic Device

Spectroelectrochemistry of the device at 650 nm with bias switching between 2V and -1.5 V (with an interval of 3s) has been carried out to evaluate the device's EC performance parameters like CCr, coloration efficiency and switching time and cycle life. One switching cycle with applied bias in figure 4.9a shows a switching time of 1.5 s by the device to switch between green and brown states with 80% absorbance change in both cases (Figure 4.9a), this absorbance change is sufficient to see appreciable colour change between two coloured states of the device. However, as per reported literatures on ECDs, for 90% absorbance change the device took 2s to switch between green and brown coloured states. This switching time is one of the best for an inorganic solid state device. Moreover, it takes very small biases of less than couple of volts for switching which is an additional advantage. The device shows very stable absorbance switching for more than 900 s or 300 consequent switching cycles (Figure 4.9b) between green and blue states with little change in the absorbance of the device in either of the states. This stability in absorbance cycles of the device is better as compared to the performance of the individual components. The EC performance of Co<sub>3</sub>O<sub>4</sub> and PB individual electrodes show poor performance (section 3.1.4) whereas the combined device of  $Co_3O_4$  and PB is far better. Current injected/ extracted with applied switching pulse has been plotted in Figure 4.9c. Colouration efficiency ( $\eta_{ce}$ ) one of the key parameters for measuring performance of any ECDs, is obtained using Eq. 1.4 and estimated to be 246 cm<sup>2</sup>/C (Figure 4.9d).

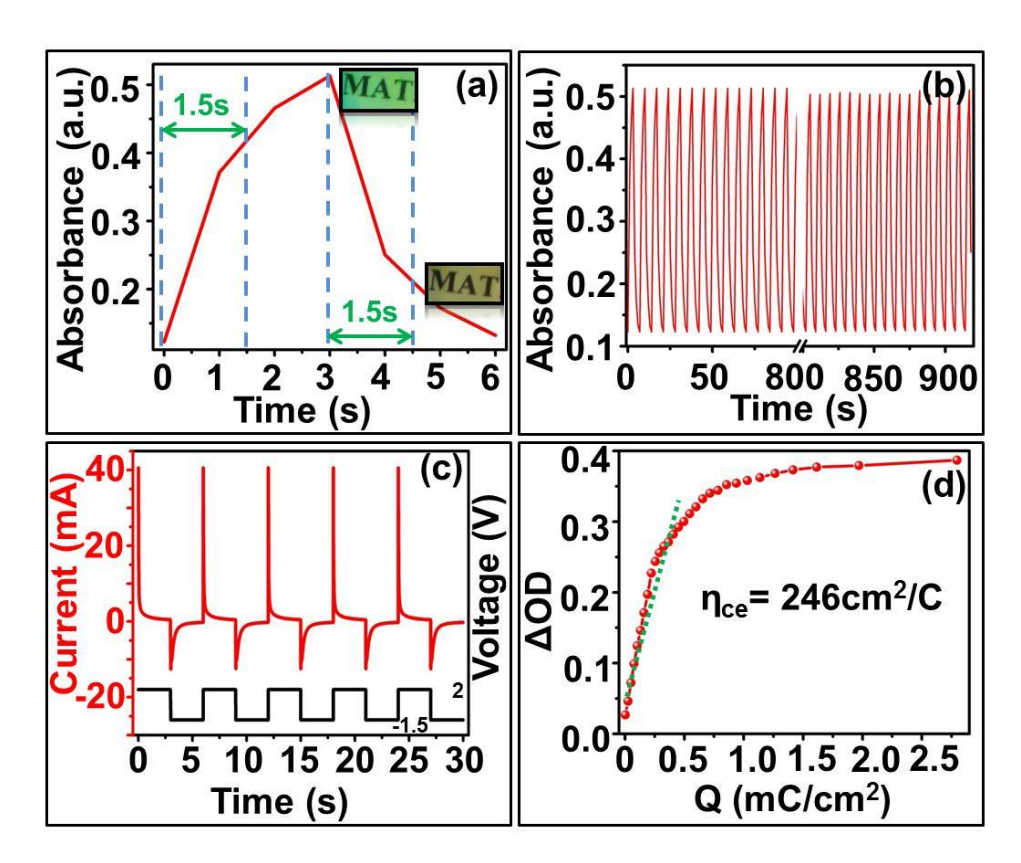


Figure 4.9: (a) One absorbance switching cycle of the device under bias pulse with extreme bias of 2V & -1.5 V, (b) extended absorbance switching for 300 pulses along with variation of current with applied bias in (c), and (d) variation in optical density with charge density.

The estimated coloration efficiency of approximately 250 cm<sup>2</sup>/C is very high especially for an all-inorganic device as it is comparable to an all-organic or hybrid EC solid state ECDs. A comparison has been shown to appreciate this fact in table 3.2. The other results have been shown for PB and Co<sub>3</sub>O<sub>4</sub> containing inorganic material toward its performances in table 3.2. It is due to the fact that the combined device contains complementary EC materials in the pre-designed manner which supports each other's redox reaction during device operation.

Table 4.2: Comparison of reported device with known inorganic devices containing PB or Co<sub>3</sub>O<sub>4</sub>.

S.N	Device	Switchi	Colouratio	Optical	Stabili	Refer
0.	composit	ng time	n	Contras	ty	ences
	ion	(s)	efficiency (cm <sup>2</sup> /C)	t (%)	(no. of cycles)	
1.	Cr doped Co <sub>3</sub> O <sub>4</sub>	3.47	11.8	5	Not reporte d	C. R. Dhas et al <sup>3</sup>
2.	Co <sub>3</sub> O <sub>4</sub>	4	20	31	10	A. Bach iri et al <sup>4</sup>
3.	PB+TiO <sub>2</sub>	3,2	135	30	400	B. Seela ndt et al <sup>5</sup>
4.	PB+PAN I	Not reported	86.7	27	Not reporte d	R. Duek et al <sup>6</sup>
5.	PB+poly butylviol ogen	10	157	58	1000	M. Fan et al <sup>7</sup>
6.	PB	3.4	150	Not reported	Not reporte d	R. Morti mer et al <sup>8</sup>
7.	PB+Co <sub>3</sub> O <sub>4</sub>	2	246	40	300	This work

Thus, less amount of charge is required for a definite optical change in the combined device as compared to a single layer ECDs. This smaller value of charge density obtained during EC operation helps in achieving higher value of coloration efficiency. Such a highly efficient all-inorganic device with less than 2 s switching time makes this device one

of its kind. Furthermore with stability of more than 300 cycles with little compromise on the performance makes the inorganic EC materials relevant for an actual solid state device thus its robust behaviors, an advantage of inorganic family, can still be exploited to achieve application oriented solid state ECDs. In other words, the presented Co<sub>3</sub>O<sub>4</sub>/PB bi-layered structure can help overcoming the drawbacks of inorganic EC materials thus facilitating an efficiency fast all-inorganic ECDs.

#### 4.4 Summary

A step-wise spectroscopic and electrochemical studies on two different combination of all-inorganic and inorganic /organic (say hybrid) device suggests that the improved EC performances and multicolor EC behavior is possible if used in bi-layered geometry. A controlled electrochemical experiments performed on individual electrodes suggests bias induced redox activity of EV, Co<sub>3</sub>O<sub>4</sub> and PB as the switching mechanism of the device. The electrochemically deposited dense films of Co<sub>3</sub>O<sub>4</sub> and PB showed decreased redox potential and were accompanied by redox induced chromic modulation. The device engineering of the amalgamation of Co<sub>3</sub>O<sub>4</sub> to EV and PB improves and generates the EC property with creating the effect of new color. A device fabricated using the organic (Viologen)-inorganic (Co<sub>3</sub>O<sub>4</sub>) hybrid components, showed a CCr of 66% with a switching time of 500ms with a low operation voltage of 1.8V. As a result, the device showed a coloration efficiency of 368 cm<sup>2</sup>/C and remained stable for more than 120 switching cycles.

Furthermore, an all-inorganic device was realized using Co<sub>3</sub>O<sub>4</sub>-PB showed a fast response (1.5s) and power efficient (246 cm<sup>2</sup>/C) performance with a good CCr (40%) and stability (more than 300 switching cycles) maintaining the robust nature of the inorganic EC family which switches between blue, green and brownish colors with a small bias of less than couple of volts. Therefore, the overall EC performances of inorganic material can be increased at some extant by

choosing these suitable parameters and combination of materials and can also be enhance on preparing the nanomaterials in different chemical composition which comes in the category of binary, ternary mixed metal oxides and in oxyfluorides. These materials with different nanoarchitecture may exhibit additional application in addition to electrochromism. Such multifunctuional application from these nanostructures has been explored in following chapters.

### Chapter 5

### Bifunctional Application of Nano-Nickel Cobalt Oxide

This chapter deals with the bifunctional application of Ni-Co binary oxide nanoneedles in electrochromism and glucose sensing. Detailed electrochemical and in-situ bias dependent optical spectroscopic studies of hydrothermally grown nanoneedles have been carried out to understand various aspects related to electrochromism and glucose sensing. A good operating voltage ( $\sim$  2V) and color modulation (50% contrast) for switching between whitish translucent and dark brown colors have been achieved<sup>7</sup>. Furthermore, the nanoneedles grown on carbon cloth electrode shows selective glucose sensing properties with a sensitivity of 3000  $\mu$ A/mM/cm<sup>2</sup> as revealed using detailed electrochemical and impedance spectroscopic measurements<sup>8</sup>. Role of nanoneedle architecture on each of these applications have been studied on the samples deposited over appropriate substrates.

<sup>&</sup>lt;sup>7</sup> Devesh K Pathak et al, IET Nanodielectric, 2021, 4,75-80

<sup>&</sup>lt;sup>8</sup> Devesh K Pathak et al, ACS Appl. Nano Mater., 2021, 4, 2, 2143–2152

## 5.1 Binary Transition Metal Oxide nanostructures and their application

An outstanding class of functional material having the ability to show potential applications in important science and technological fields comes under the 'Binary (or Ternary)' metal oxides family[147–151]. Simple synthesis process of these oxides, among the all other tedious synthesis process, through non-aquous non-hydrolytic process, makes these materials much favourable for controlling their crystallite size, shape and assembly behaviour which is highly required to deliver its surface controlled electrochemical property. Binary metal oxides  $(A_xB_yO_z; A\&B \text{ transition metal}, x,y,z = \text{chemical composition})$  possess structural stability along with higher electrical conductivity which leads to the occurrence of many applications. The metals present with the oxides provide different oxidation state of both metals which are helpful to generate different electrochemical active/inactive ions and thus affect surface controlled properties leading to applications such as supercapacitor[71,152], glucose sensing[153], hydrogen/oxygen evolution[154,155] reaction and of course the electrochromism. Out of them, EC property can be greatly improved in terms of switching performance in which ions/electrons are required to activate the redox reaction speedily at the material (or electrode) for showing the fast coloration and bleaching even for the inorganic materials where it is challenging process[156,157].

There are many possible ways to improve the ECDs performance as described in chapters 3 and 4. Various improvising factors can be taken care of from the steps as early as the preparation of electrode to device fabrication. Doped TMO or metal composite materials also exhibit improved chromic modulation[158]. Different crystal structures or nanostructure architecture altogether gives different property of the material which can be seen through electrochemistry measurement of single electrode. Nanocomposites are also currently being studied beyond the bulk that has emerged for their exceptional optical and electronic properties.

Amongst all TMOs and their composites, spinal compounds are less often studied. Oxide of Ni and Co (NiCo<sub>2</sub>O<sub>4</sub>) is one such material which remains one of the least discussed among all[159]. Other magnetic spinal compounds like NiFe<sub>2</sub>O<sub>4</sub> [160], CoFe<sub>2</sub>O<sub>4</sub>[161], Co<sub>3</sub>O<sub>4</sub>[162] and Fe<sub>3</sub>O<sub>4</sub>[163] have been studied very well in bulk and thin film phase of material to investigate the physical, chemical and mechanical properties. The main reasons behind this disparity are the unavailability of single crystal or films and its less stable nature at low temperature. However, Ni and Co oxide in NiCo<sub>2</sub>O<sub>4</sub> phase attracted much attention from industry for exploring in fuel cell electrode, supercapacitor, sensing devices. oxygen catalysis and water electrolysis applications[164,165]. Being the magnetic material, it has also other applications but still has a wide scope to search new properties in the NiCo<sub>2</sub>O<sub>4</sub> insight using the different techniques and phenomenon.

#### 5.2 Preparation of NiCo<sub>2</sub>O<sub>4</sub> Nanoneedles

Hydrothermal method[102] has been used to deposit the film from Ni and Co precursors in different molar concentration over the two different types of geometrical substrates. The nanostructures have been grown on both the substrates (FTO coated glass and CC) under same environment and same deposition conditions using recipe mentioned earlier (section 2.4.3, chapter 2). Figure 5.1 schematically represents the hydrothermal process carried out to yield a thick white translucent film on an FTO substrate. Due to the substrate's constraints, the FTO provides only one possible direction for growing the nanostructure. On the other hand, the CC allows all possible three directions to grow the same nanostructure as shown in Figure 5.1 which is likely to have higher surface area. The prepared thin film has been characterized to known the phase purity and surface architecture of the film prior to any application.

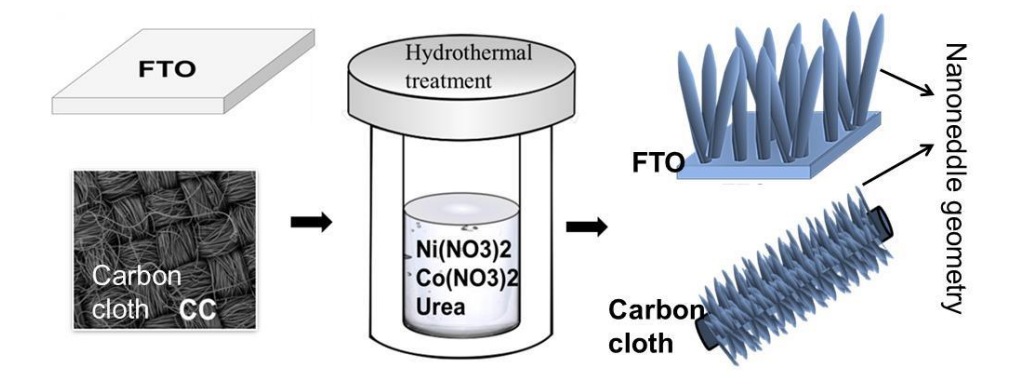


**Figure 5.1:** Schematic showing growth process of Ni-Co nanoneedle over FTO and carbon cloth substrates using hydrothermal process.

#### 5.2.1 Characterisation of NiCo<sub>2</sub>O<sub>4</sub>

The deposited film has been scratched off from one of the substrates and taken for the XRD measurement (Figure 5.2a). Peaks corresponding to diffraction angles at 36.6°, 64.7°, 59.2° 44.4°, 31.2°, 55.2°, 19.0° are observed in the order of decreasing intensity. The observed XRD pattern well supports the JCPDS no 20-0781[166,167] reveals the existence of its inverse spinal crystal structure. A given XRD peak shows a broader width which is a sign of nanomaterial formation. Absence of any extra peak or hump in the XRD measurement represents the occurrence of single phase nanomaterial film. This has been further confirmed using Raman spectroscopy (Figure 5.2b) measured using 532 nm excitation source wavelengths in which laser spot was focused on the sample at size of ~2 µm. The sample was scanned from the 100 cm<sup>-1</sup> to 1000 cm<sup>-1</sup> with the fixed 30 sec acquisition time and shows five Raman active modes from the inverse spinal NiCo<sub>2</sub>O<sub>4</sub> crystal structure. Raman modes observed at 187.8 cm<sup>-1</sup>, 521.1 cm<sup>-1</sup>, 610 cm<sup>-1</sup> are assigned to F<sub>2g</sub> mode whereas the 474  $\text{cm}^{-1}$  mode is assigned to  $E_{2g}$  and 680.5  $\text{cm}^{-1}$  mode is assigned to  $A_{1g}$  mode (Figure 5.2b). The Raman spectra shown in Figure 5.2b is showing the broader peak which is a consequence of doublet-like feature by virtue of the presence of un-identical Ni and Co atoms at the octahedral sites[160,168]. Therefore, a distortion arises in a crystal structure due to the different ionic radii of Ni and Co ions and thus the considerable effect appears clearly in the Raman spectrum. Since Raman spectroscopy is a local structure sensitive tool so it probes the defects very effectively.

Above two initial characterizations help to identify the nature of sample which tells that, Ni and Co atoms are combined in  $NiCo_2O_4$  inverse spinel structure. The band gap calculation has been done for  $NiCo_2O_4$  scratched film using DRS in (Figure 5.2c). The inset of Figure 5.2c shows the whole reflectance spectra from 200 nm to 800 nm and the band gap calculation has been carried out using Tauc plot[134,169], which comes around two values 1.6 eV and 2.3 eV. The two band gap values are coming by extrapolating the slope on the energy axis. Since the band gap is a measure of electronic transition from O 2p orbital of valence band to 3d ( $t_{2g}$ ,  $e_g$ ) orbital of conduction band of transition metals and the signature of two band gap in  $NiCo_2O_4$  occurs due to the high and low spin state of  $Co^{+3}$  co-existing in given spinal compounds[170].

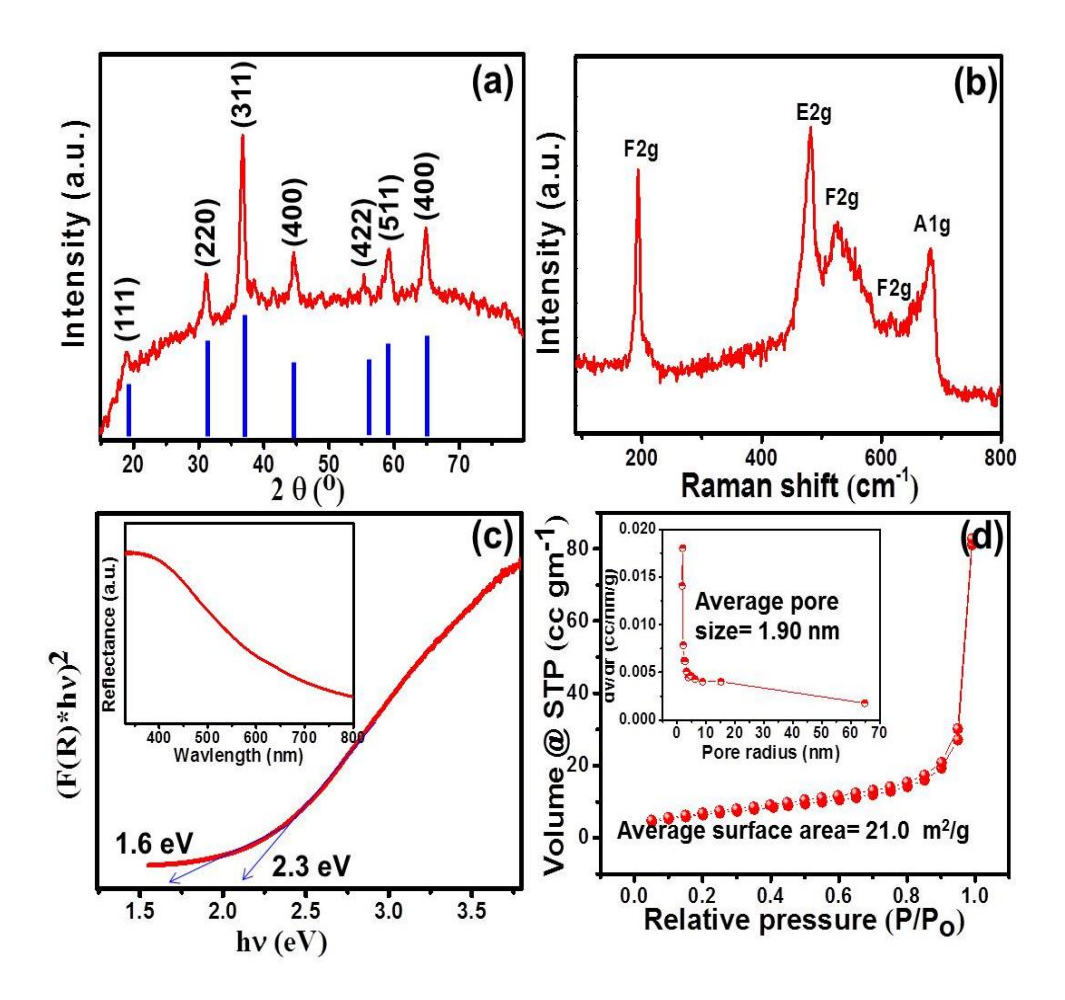


Figure 5.2: (a) XRD pattern, (b) Raman spectrum, (c) diffused reflectance spectroscopy for finding the band gap using Tauc-plot and (d) BET curve performed under  $N_2$  absorption de-absorption process from the sample in powder form obtained by scratching off the film.

Since one of the samples has been intended for application as a glucose sensor, its surface area has been estimated as it is one of the important factors. Therefore, Brunauer-Emmett-Teller (BET) measurement (Figure 5.2d) has been carried out to check the surface area of local architecture through N2 absorption-desorption measurement under the relative pressure ranging from  $0 < \frac{P}{P_0} \le 1.00$  at 77 K temperature[171]. The average surface area of 21 m²/gm and average pore size of 1.9 nm have been estimated from the BET measurements suggests its possible application for sensing and EC applications. This microporous nature of the nanostructures may further get improved if it is grown in an architecture that allows more exposed surface for any reaction to take

place that enables its utility. Keeping this in mind, the NiCo<sub>2</sub>O<sub>4</sub> nanostructures have been grown on CC so that overall exposed area of the nanostructure can be increased. On the other hand, these nanostructures have also been grown on conducting electrode (FTO on glass) for EC application where CC is not a suitable substrate due to design constraints. The nanostructure architecture and its homogeneity over these different geometrical substrates must be analyzed and therefore SEM has been chosen for this measurement. The next section is showing the morphological analysis of hydrothermally deposited NiCo<sub>2</sub>O<sub>4</sub> on two substrates for which both applications have to be done. Both the applications, an EC electrode and glucose sensor, have been discussed one by one as follows.

#### 5.2.2 Morphology of NiCo<sub>2</sub>O<sub>4</sub>

The surface morphology has been checked on both sample (@FTO and @CC) to know the surface plot alignment of nanostructure. The morphology of white translucent film of NiCo<sub>2</sub>O<sub>4</sub>, characterized by XRD and Raman measurements, have been studied using SEM (Figure 5.3a-5.3d) revealing a film consisting of nanoneedle like structures. Figure 5.3a is showing the top view image of the film NC@FTO revealing vertically aligned nanoneedle architecture with sharp tips. The zoomed SEM image (Figure 5.3b) also reveals that the nanoneedles are deposited homogenously over the whole substrate. Moreover, all the nanoneedles are well separated from each other which mean the availability of larger surface areas to be exploited for specific application as has been discussed later on. In other words, better morphology coverage with porous nanostructures signifies the presence of larger contact area of nanoneedle to activate the charge transfer reaction (in the case of electrolytic medium) for further application with a higher rate of reaction. The ImageJ<sup>TM</sup> software has been used to qualitatively estimate the average tip size of nanoneedle nanostructures (inset, Figure 5.3b) which comes out to be ~10 nm. The nanoneedles are well separated leaving most of the nanostructure exposed which can be clearly seen from the top view.

The morphology of NiCo<sub>2</sub>O<sub>4</sub> grown on the CC substrate (NC@CC) has also been checked through SEM (Figure 5.3c). The inset SEM image in Figure 5.3c is showing the bare CC substrate over which the NSs have been grown. Top view of SEM image in Figure 5.3c is displaying the material deposited all over the CC fabric with maintaining the homogeneity of material. The same nanoneedle like structure of deposited material can be clearly seen in the magnified view (Figure 5.3d). The top view images clearly show that the deposited film is homogenous in nature. The elemental composition for the deposited material has also been checked through EDX experimental on the NC@FTO and the elemental composition peak from elements present in NC@FTO is shown in Figure 5.3e. The elemental composition present in the selected scan area in SEM during EDX experiment has been shown in Figure 5.3f. The combined results from figure 5.3e& 5.3f confirm the composition of material prepared by of Ni and Co oxides.

To complete the morphological analysis, TEM measurement has been performed on nanoneedle and confirms the deposited architecture occurs at nano scale (Figure 5.3g) with ~ 45 nm thick nanoneedles getting deposited (inset). Crystallinity of these nanoneddles can be confirmed using the selective area electron diffraction (SAED) pattern (Figure 5.3f) showing spot patterns.

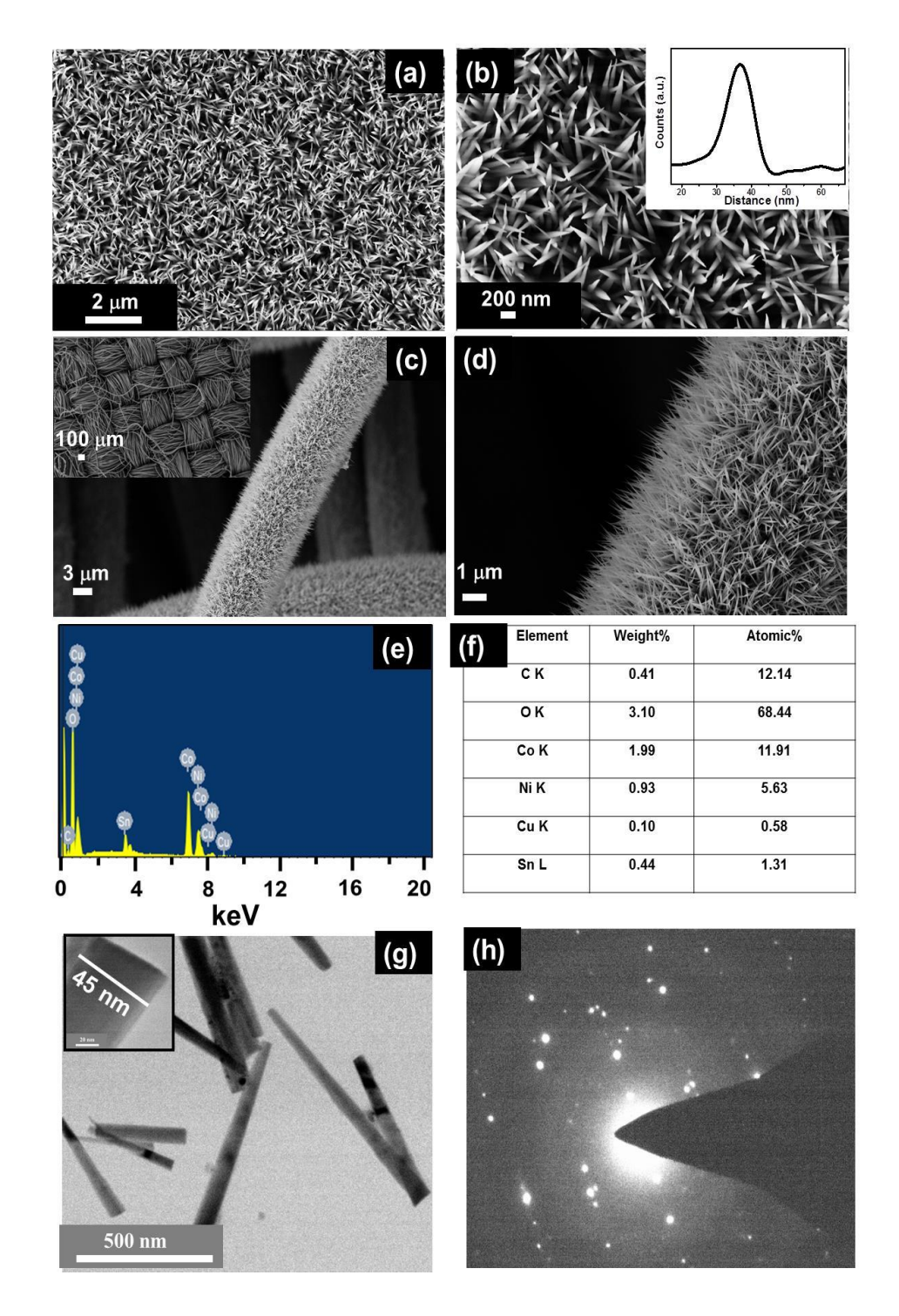


Figure 5.3: (a) Top view of nanoneddle  $NiCo_2O_4@FTO$  film with enlarged view at 200 nm (b), (c) Top view of nanoneddle  $NiCo_2O_4@CC$  film (CC in inset) with enlarged view at 1  $\mu$ m (d). (e) EDX analysis of filme over FTO substrate and their (f) different elemental composition ratio, (g) TEM analysis of one nanoneddle with the average diameter (inset) of 45 nm, (h) SAED pattern of nanoneddle.

#### 5.2.3 Elemental composition validation of NiCo<sub>2</sub>O<sub>4</sub>

To further investigate constitutes present in the sample, XPS measurement in high energy synchrotron source with each element at its valence state of NiCo<sub>2</sub>O<sub>4</sub> nanoneedle has been carried out (Figure 5.4). The full scan spectrum (Figure 5.4a) shows the existence of each desired element in sample like Ni, Co, O and C as well. The other XPS spectra (Figure 5.4 b,c & d) have been recorded at valence state edge of Ni(2p), Co(2p) and O(1s) which have been plotted with considering the reference of carbon peak (~284.3 eV). The Ni(2p) edge spectrum (Figure 5.4b) gives two intense peaks corresponding to  $2p_{3/2}$  (856 eV) and  $2p_{1/2}$ (874 eV) along with two intense satellite peaks. Further on deconvoluting the spectrum, the peak corresponding to  $2p_{3/2}$  and  $2p_{1/2}$  are observed due to the occurrence of two pairs of spin orbit doublet characteristic for Ni<sup>+3</sup> and Ni<sup>+2</sup> [72,172]. A similar trend can also be seen for Co (2p) edge (Figure 5.4c), which contains intense peaks of 2p3/2 (782 eV) and 2p1/2 (798 eV). De-convoluted spectrum reveals that Co<sup>+3</sup> and Co<sup>+2</sup> existence as a consequence of two strong spin-orbit doublets of Co(2p)[141,173]. Further on analysing and deconvoluting the O(1s) spectrum (Figure 5.4 d) two peaks at 531 eV and 533 eV corresponding to O(I) and O(II) respectively,[166] are observed likely due to existence of defect with low oxygen coordination or may be attributed to the metal-oxygen bond. The above-mentioned structural and compositional investigations not only established the formation of NiCo<sub>2</sub>O<sub>4</sub> but also suggest that the architecture with obtained porosity and surface area are suitable from application in sensing. Additionally, EC properties, a very less explored application of NiCo<sub>2</sub>O<sub>4</sub> nanostructures, can also be explored from these samples designed on appropriate substrate. For this, the samples have been prepared on FTO (say, NiCo<sub>2</sub>O<sub>4</sub>@FTO) and CC (say, NiCo<sub>2</sub>O<sub>4</sub>@CC) substrates for further study using electrochemical methods.

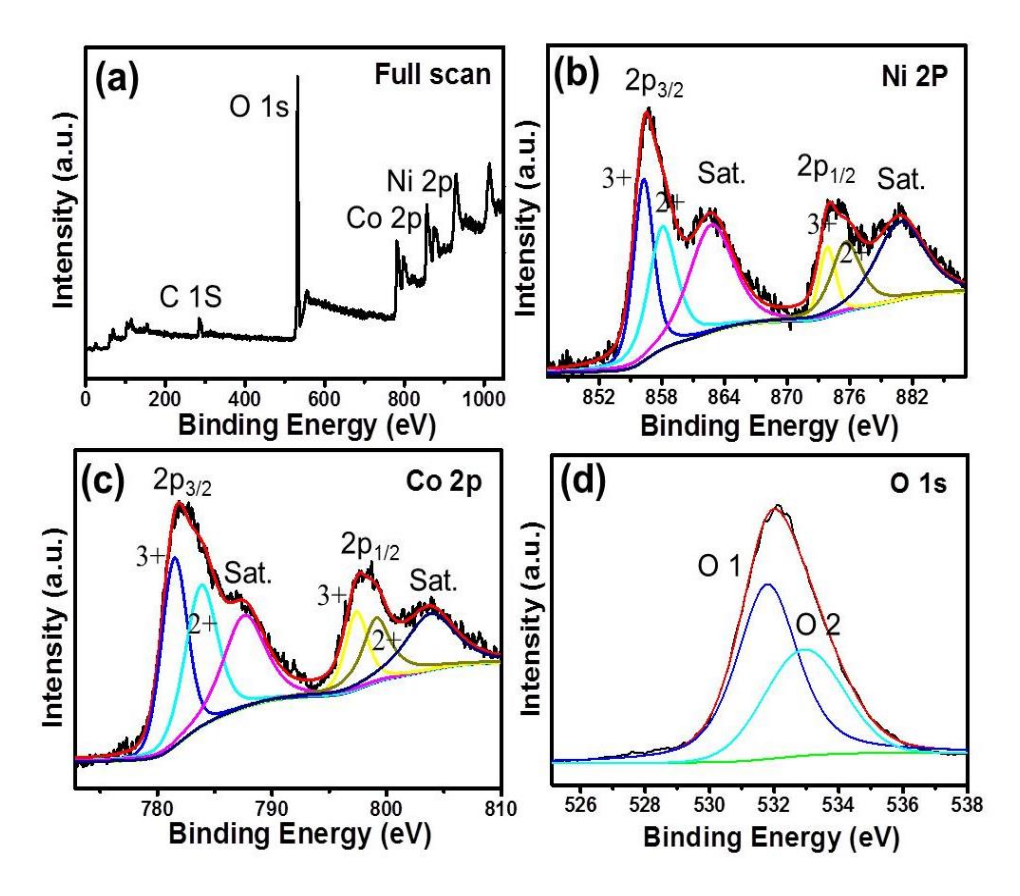


Figure 5.4: Synchrotron source XPS curves from NiCo<sub>2</sub>O<sub>4</sub> nanoneedle in (a) full scan, (b) Ni 2p edge, (c) Co 2p edge and (d) O 1s edge scans.

#### 5.3 Electrochromism of nano-NiCo<sub>2</sub>O<sub>4</sub>

Since, the NiCo<sub>2</sub>O<sub>4</sub> films have been prepared for intended application as EC electrodes, the electrochemical measurement has been performed using three electrodes setup. Three electrodes setup consists of RE, CE and WE as Ag/AgCl, a Pt-wire and NiCo<sub>2</sub>O<sub>4</sub>@FTO film respectively, based on the procedure discussed in section 2.3. The electrochemistry was performed in a cell consisting of 1 M aqueous NaOH electrolyte. The CV measurements were done using a reversible voltage scan from -0.2V to +0.6 V applied across the WE (NiCo<sub>2</sub>O<sub>4</sub>) and RE (Ag/AgCl) and corresponding current is measured across the CE (pt- wire) and WE. Figure 5.5a shows the CV scan curves obtained with a scan rate of 50mV/sec corresponding to 1<sup>st</sup>, 25<sup>th</sup> and 50<sup>th</sup> cycle of CV scans along with the actual images of the electrode at different bias values. Under the anodic scan on sweeping the voltage from -0.2 V to +0.6 V, an anodic current peak appears near +0.45 V due to the OH<sup>-</sup> ion intercalated to the

NiCo<sub>2</sub>O<sub>4</sub>. The intercalation of OH ion to the WE switches the electrode from its parent translucent white colour state to opaque dark brown coloured state. After that, the WE get back to its natural colour, showing reversibility of the color change, state under the cathodic scan from +0.6 V to -0.2 V ( on reversing) with generating the cathodic current peak around +0.1 V is due to the OH ion de-intercalation from the electrode. Since, NiCo<sub>2</sub>O<sub>4</sub> nanoneddle type morphology possesses the larger atomic site in every isolated single nanoneddle which gives more possibility to intercalation of the OH ion and hence does not allow much time delay during on reduction/oxidation processes. The higher surface area of morphology makes the larger contact to the NaOH electrolyte making more sites for redox reaction and thus helps color modulation at low operating voltage. Due to this correlation, a low bias color switching appears to be a direct consequence of deposited nanoneddle architecture.

Therefore, a complete cycle of CV measurement shows the reversible colour switching from whitish colour to dark brown colour under the charge intercalation and de-intercalation to the NiCo<sub>2</sub>O<sub>4</sub> electrode. Thus, the electrode exhibiting two states colour switching, shown in the background of CV diagram (real photographs), is said to be EC electrode and the redox behavior of electrode making it potential CE candidate for the other EC active species. The stability of redox behavior of electrode under colour modulation has also been checked upto 50 cycles and the data corresponding to  $1^{st}$ ,  $25^{th}$  and  $50^{th}$  cycle is being presented in Figure 5.5a showing little variation in current. It signifies that the electrode is exhibiting a stable EC performance when used as electrode in an electrochemical cell with liquid electrolyte. Therefore, the coloration (white  $\rightarrow$  brown) and bleaching (brown  $\rightarrow$  white) state of the EC active NiCo<sub>2</sub>O<sub>4</sub> electrode can be named as ON and OFF states of switching respectively for discussion purpose.

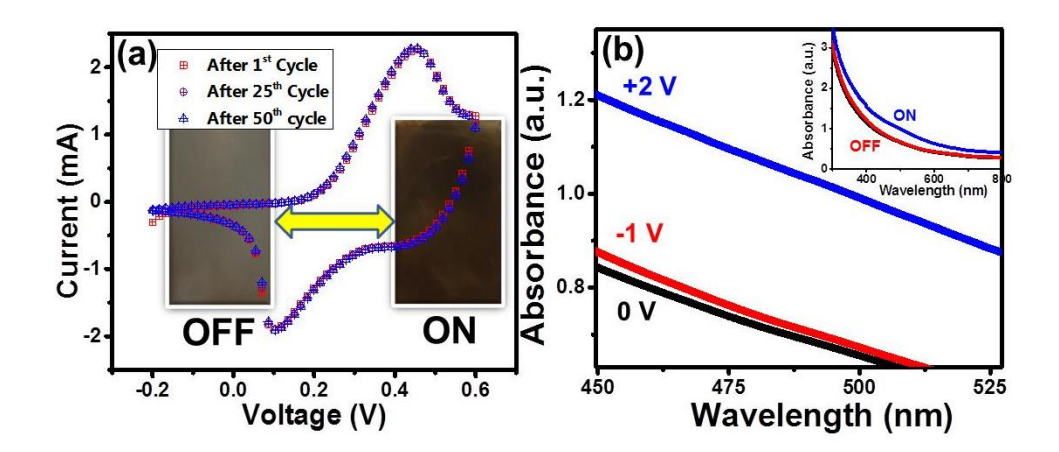


Figure 5.5: (a) CV curves from  $NiCo_2O_4@FTO$  with colour switching for different cycles and, (b) in-situ UV-Visible spectroscopy of  $NiCo_2O_4@FTO$  electrode under the external bias of +2V and -1V.

To better understand the chromic modulation of EC electrode during color switching, in-situ UV-Vis spectroscopy has been performed by applying bias in two electrode system due to experimental constraints to use three electrode arrangements. The UV-Vis experiments have been done by applying voltages upto 2V between the EC NiCo<sub>2</sub>O<sub>4</sub> electrode and Pt-wire as the two electrode system needs relatively higher raw voltages to switch the electrode from beached state to the coloured state as compared to three electrode system. The bias dependent absorption spectra have been recorded in the whole range of visible wavelength for OFF and ON states of the electrode (Figure 5.5b). The absorption spectrum (black curve, Figure 5.5b) is taken from the electrode in natural state shows a smooth absorption spectrum explaining translucent nature of the electrode. The absorbance throughout the whole wavelength range increases on applying a +2 V bias to the electrode which indicates the appearance of the dark brown colour of electrode shown by the blue curve (Figure 5.5b). The reversibility, an important aspect in electrochromism, was checked during CV measurements and the same state has been seen using absorption spectrum by reversing the applied bias (-1 V) to the NiCo<sub>2</sub>O<sub>4</sub> electrode (red curve, Figure 5.5b). It is apparent that a -1 V bias is sufficient to completely reverse the visible spectrum to reinstall the original color of the electrode (the bleaching

process) confirming the reversible nature of the EC effect. Therefore, the electrode found in active state for the chromic modulation in the potential domain of +2 V and -1V which is itself less operating voltage in the family of all inorganic transition metal oxide (TMO). Overall absorption spectrum in the whole visible range has been shown in the inset (Figure 5.5b) to appreciate the bias dependent color modulation of the solid state nanoneedle electrode. A close analysis of the bias dependent spectra (Figure 5.5b) showing ~ 50 % change in the absorbance hence the electrode acquires an CCr of 50% corresponding to 500 nm wavelength which is one of the best for an inorganic EC material especially for such a low operating bias. A large optical contrast with small operating voltage of as low as 1V can be achieved for NiCo<sub>2</sub>O<sub>4</sub> electrode likely due to the deposited nanoneedle structure which makes larger active sites exposed to allow the charge intercalation, de-intercalation reaction speedily making the redox process easy for color modulation. It is clear from the above discussion that the new nanoneedle architecture made of binary transition metal oxides enables one to get EC modulation easily in terms of switching voltage and CC which is one of the best in the family of inorganic EC materials. It opens a possibility of new paradigm for revisiting power efficient ECDs using robust inorganic materials.

#### 5.4 Glucose-sensing of nano-NiCo<sub>2</sub>O<sub>4</sub>

The development in the area of nanoscience has touched biosciences and biomedical engineering as well because it successfully addressed several problems related to detection and treatment of diseases in addition to developing sensor[174–177]. Various chronic deceases that are fatal for human life include 'diabetes' where therapy is the only management protocol[178–181]. Prior to decide a therapeutic management protocol, detection and monitoring of glucose level in the blood is most important. Under this context, availability of glucose sensors are lifesaving and needs research to optimize the material used for this purpose[72,182]. Glucose sensors are generally based on the very basic principle of

detecting the glucose by the root of converting glucose into gluconic acid and H<sub>2</sub>O<sub>2</sub> as a result of oxidation process leading to rise in current which is value proportional to the amount of glucose present[72,153,182]. Sensitivity of such sensors is decided by the efficiency with which such oxidation take place[183,184]. Thus, the sensitivity of glucose sensor device/electrode can be increased by appropriately designing the sensor electrode with large surface area and good redox activity behavior. Easy and accurate CV measurements help to understand the oxidation process for detecting glucose with high sensitivity at low detection limit and help also in optimizing the operation voltage for power efficient function.

Prior to sensing experiments, the same three electrode system in electrochemistry has also been used for glucose sensing application for  $NiCo_2O_4@CC$  (works as WE) has been discussed later on. When scanned in the direction shown (Figure 5.6a) clear oxidation and reduction peaks at +0.34 V and +0.24 V respectively can be seen when measured with a scan rate of 10 mV/s. The peak redox current values show a linear variation as a function of scan rate (Figure 5.6b). Such a linear relation of current with respect to scan rate is a manifestation of surface controlled reaction that further indicates that the  $NiCo_2O_4@CC$  could be a good system for glucose sensing applications.

The glucose-sensing capabilities of stable NiCo<sub>2</sub>O<sub>4</sub>@CC electrode were examined by observing the dependence of the EC response on the addition of glucose in the electrochemical cell when measured in three electrode geometry (Figure 5.6c). When an aqueous solution of glucose (with varying concentrations) is added, the oxidation current increases compared to the current values observed in the absence of glucose (Figure 5.6c). The current enhancement, in response of the amount of glucose added, varies as a function of glucose concentration (Figure 5.6d). Different glucose concentration has been chosen from 1mM to 8mM for glucose sensing with high accuracy and added into the electrochemical bath of 50 μl of each stock solution. A direct trend between the current flowing in the electrochemical cell and glucose

concentration means that the Redox current change is a response of added glucose and signifies the glucose sensing properties of  $NiCo_2O_4@CC$  electrode. Sensing of glucose has apparently taken place form the dipped area of electrode (0.25 cm<sup>2</sup>) as a result of following redox reaction (Eqs.5.1- 5.3).

$$NiCo_2O_4 + H_2O \rightarrow NiCo(OH)_2$$
 (5.1)

$$NiCo(OH)_2 + glucose \rightarrow NiCo_2O_4 + H_2O_2 + Gluconic acid$$
 (5.2)

Gluconic acid + 
$$H_2O \rightarrow Gluconate^- + H^+$$
 (5.3)

The CV measurement shows the redox activity of  $NiCo_2O_4$  by means of change in the oxidation state of  $Ni^{+3}/Ni^{+2}$  and  $Co^{+3}/Co^{+2}$  during the oxidation process (Eq. 5.1). Oxidized Ni/Co acts as a catalyst to oxidize glucose on reducing itself (Eq. 5.2). Immediate conversion of gluconolactone to gluconic acid followed by formation of gluconate ion (Eq. 5.3) that increases the conduction as reflected in the increased current in the CV curves. Specific sensitivity has been measured to quantify the sensing properties of the electrode from the glucose concentration dependent variation of current (Figure 5.6d) which comes out to be 3000  $\mu$ A/mM/cm<sup>2</sup>.

In order to further ensure that the current response is due to the added glucose, the oxidation current's (corresponding to +0.4 V) response has been studied as a result of gradual glucose addition as a function of time (Figure 5.6e). A spike in oxidation current is observed every time when glucose is added (shown as \* mark, Figure 5.6e) in the cell which further confirms that the electrode is sensitive to glucose. Furthermore, to discount the hindrance effect of other compound like uric acid (UA), folic acid (FA) ascorbic acid (AA) on oxidation current, these compounds have been added which does not alter the current flowing in the cell as shown in Figure 5.6e where markings @, \$ and # shows the

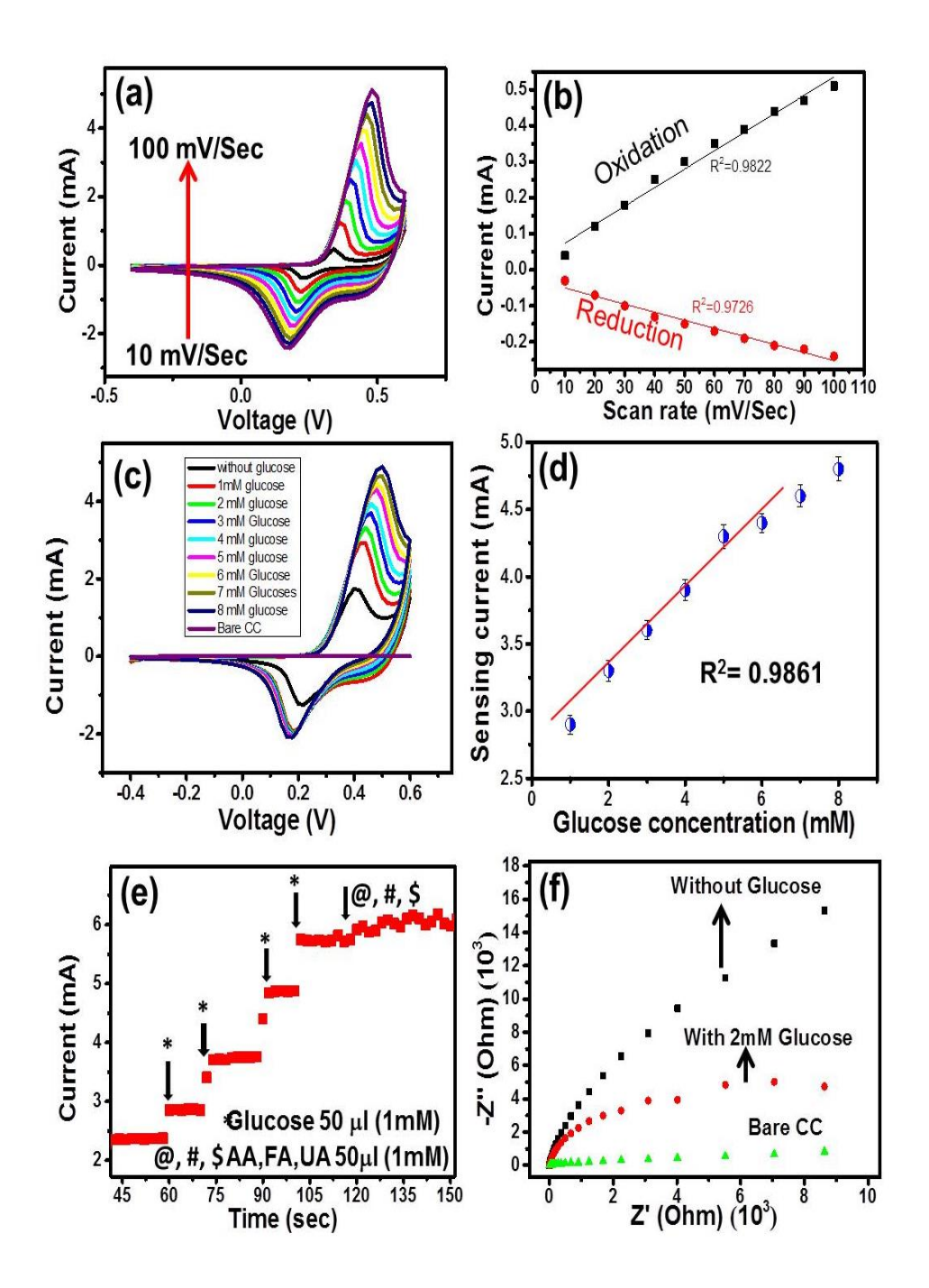


Figure 5.6: (a) CV performance of  $NiCo_2O_4@CC$  WE under different scan rate, (b) Variation of oxidation and reduction current with respect to scan rate, (c) Glucose sensing current response with varying concentration from 1mM to 8mM (d) The variation of sensing current with the varying glucose concentration, (e) Chronoamperometric techniques for measuring exclusive glucose sensing, (f) EIS (Nyquist plot) data of NiCo2O@CC with and without presence of glucose.

points when AA, FA and UA have been added. Gradual addition of glucose (50 µl) has been sensed by the NiCo<sub>2</sub>O<sub>4</sub>@CC with showing the gradual enhancement in the current (50-100s, Figure 5.6e) whereas on adding same volume of AA, UA and FA solution does not change the current. This ensures the selectivity of glucose sensing of NiCo<sub>2</sub>O<sub>4</sub> nanoneddle compared to other compounds. The effect of glucose has also been seen using Electrochemical Impedance Spectroscopy (EIS)[185] done on NiCo<sub>2</sub>O<sub>4</sub>@CC electrode in a solution with and without glucose (Figure 5.6f). The Nyquist plot shown in black curve represents the case when no glucose was present in the cell and represents a larger semicircle, as compared to the case when glucose was present in the cell (red curve, Figure 5.6f) at high frequency region. The surface of NiCo<sub>2</sub>O<sub>4</sub> nanoneddle structure and the glucose molecule in the electrolytic solution gives rise to a high frequency semicircle due to the electrochemical reaction impedance and, on the other hand, the negligibly small semicircle at lower frequency side is due to minimal interface impedance between material and the substrate. On the whole, clearly visible effect of glucose on Nyquist plot, like electrochemical analysis, ascertains the glucose sensing properties of NiCo<sub>2</sub>O<sub>4</sub>@CC electrode. A glucose concentration dependence of oxidation current and impedance, along with passive response of AA, FA and UA, makes this a suitable candidate (spinal NiCo<sub>2</sub>O<sub>4</sub> nanoneedle) for glucose sensing application. On the whole, electrochemical and in-situ optical measurements from hydrothermally grown NiCo<sub>2</sub>O<sub>4</sub> nanoneedles establishes them to be good candidate for dual application as EC electrode as well as glucose sensor.

# 5.5 Summary

Hydrothermally grown microporous NiCo<sub>2</sub>O<sub>4</sub> nanoneddle structures, showing optical and electrochemical modulations under applied biased and under glucose addition respectively, are found to be good candidate for dual application in electrochromism and sensing. The NiCo<sub>2</sub>O<sub>4</sub> nanoneddles, grown on conducting transparent FTO electrode, show bias dependent reversible color switching. The electrode shows color

switching between whitish translucent and dark brown as examined using in-situ absorption spectroscopy. An encouraging optical contrast of 50%, with an application of only 2V bias was observed, which is one of the best operating voltages in the inorganic EC materials' family. These NiCo<sub>2</sub>O<sub>4</sub> nanoneddles, grown on carbon cloth electrode, show selective sensitivity towards glucose as reflected in terms of increased electrochemical activity in the presence of glucose whereas it shows a passive behavior towards Ascorbic acid, Uric Acid and Folic acid. Detailed electrochemical and impedance spectroscopic measurements further establishes the glucose sensing properties of these nanoneedles. Oxidation of glucose to gluconate, to increase the CV current, appears to be the sensing mechanism. A sensitivity of 3000 µA/mM/cm<sup>2</sup> could be achieved from the given architecture due to availability of more exposed area for more redox reaction to take place. Though the present chapter dealt with only couple of applications, the nanoneedles architecture, that also shows well aligned needles, can be used for exploration of other application where well aligned sharp tips are required. Electron field display, working on field emission, is one such application that requires higher S/V ratios. Applications of well aligned nanowires as field emitters have been studied in the next chapter.

# Chapter 6

# Metal Oxides Nanostructures: Field Emitters

This chapter summarizes study of electron emission property, exploited in FE display devices, of metal oxide nanostructures which are known EC materials used in EC displays. FE properties of NiO NPs and TNRs have been studied and analyzed within the frame work of Fowler-Nordheim formulation<sup>9,10</sup>. An alternative formulation for the interpretation of FE properties has been developed and validated using theoretical fitting of the experimentally observed data<sup>11</sup>. The proposed model addresses the little incompleteness presence in the traditionally used Fowler-Nordheim model.

<sup>&</sup>lt;sup>9</sup> Devesh K Pathak et al, Superlattices and Microstructures 125 (2019), 138-143

<sup>&</sup>lt;sup>10</sup> Devesh K Pathak et al, Superlattices and Microstructures 126 (2019), 1-7

<sup>&</sup>lt;sup>11</sup> Devesh et al. Materials chemistry and Physics 245 (2020), 122686

#### 6.1 Electron Field Emission

Emission of electrons under an applied bias, known as FE, is a quantum tunneling process which depends upon work function of the material, their electronic structure and upon the material surface geometry and of course on the magnitude of the applied electric field[75,85,87,90,186,187]. Diode like two-electrode geometrical setup is usually designed to understand the measure FE properties of a material through measuring the bias dependent current. Cathode plate is designed with the material used for investigation for FE application and attached with a high voltage for which corresponding current is observed using the other (anode) electrode. The whole apparatus is kept under a high vacuum to prevent the scattering of emitting electron (tunneling electron) from any gaseous particle[188–192]. The emission current highly depends upon the applied field and voltage required to start the emission depends on the geometry especially for nanomaterials. The applied field gets enhanced at the surface of material depending upon the morphologies in 'nano' regime that generate the overall emission of electrons after surpassing the quantum mechanical barrier[193]. This quantum mechanical approach has been solved by considering the WKB principle and summarized in Fowler-Nordheim (F-N) relation, Eq. 1.9 (section 1.5.2, chapter 1). The F-N Equation behavior describes the FE property of any material. Nanostructures of NiO and TiO<sub>2</sub> have already been discussed in chapter 3 as a potential candidate for EC display devices. Cold electron emission from these nanostructures have been discussed here that can be of use in a FE display device[194–198].

# **6.2 Nickel Oxide Nanopetals**

Optimization of various fabrication parameters, affecting the nanomaterials' properties, can be considered as one of the most important steps as it decides the material onto which the performance of the end device will depend[7,75,199–201]. This is mainly because the synthesis method and associated atomistic dynamics decide how they will come together to result in the nano-form under a given

thermodynamic conditions which in turn gets directly manifested in a unique morphology[86]. In other words, morphological variation can be one of the best parameters to study the property of nanostructure thus helping one in identifying best suitable material for applications. The morphology can be controlled by appropriately choosing the parameters and may result in surface architecture, tuned for a particular cause.

A precursor's concentration dependent surface morphologies of NiO NPs (NPs) have been studied for designing application-specific nanomaterials by hydrothermal technique. A detailed analysis on surface morphology shows how the synthesis parameters can be optimized to get a desired application specific nanostructure by taking an example of FE properties. The NiO NPs were prepared with three different precursor's concentrations out of which the sample prepared with lowest concentration was identified to show very good FE property with high enhancement factor.

#### 6.2.1 Reaction route and surface analysis

Nanomaterials' properties and thus its application inherently depend on their morphology which may depend on various parameters including concentration of precursors used. Figure 6.1 (a)-(c) show surface morphologies, obtained using SEM techniques, of samples S1, S2 and S3, (described in chapter 2, section 2.4.1) fabricated using hydrothermal process with precursor concentrations of 60 mM, 80 mM and 100 mM respectively, along with the schematic of sample preparation method and corresponding reaction leading to the nanostructures (Figure 6.1d). NPs of NiO can be seen in all the three samples with some variation in surface morphology as can be noticed qualitatively meaning that different concentration of Ni(NO<sub>3</sub>)<sub>2</sub> lead to different surface morphologies.

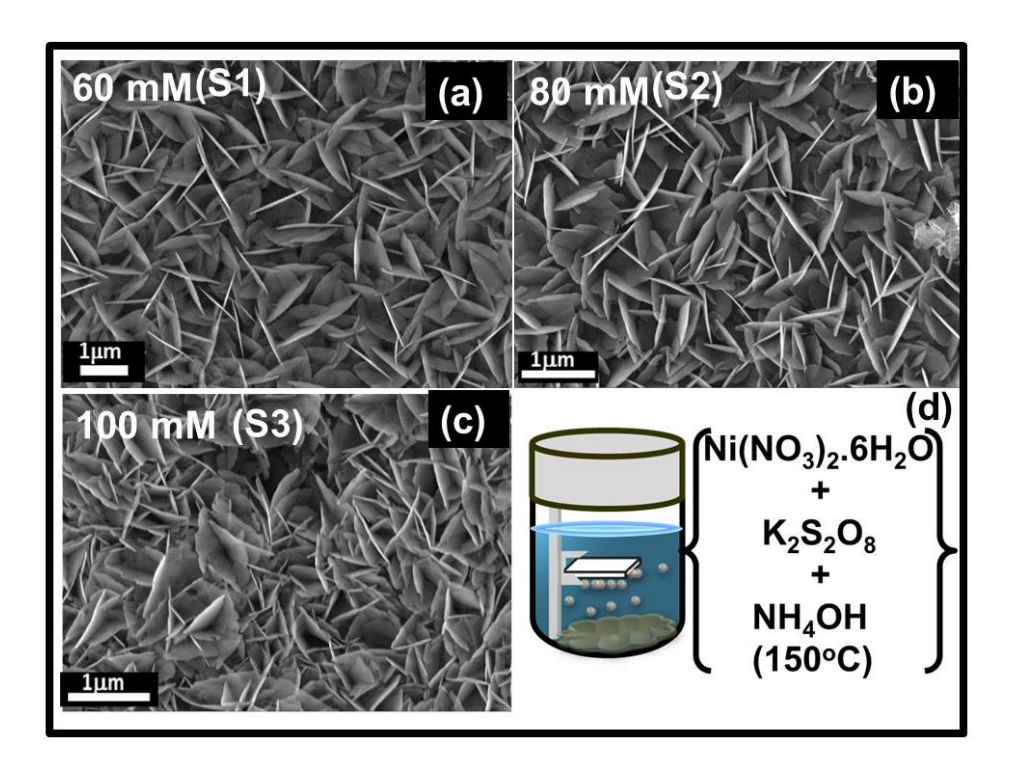


Figure 6.1: NiO NPs' micrographs of samples prepared with Ni(NO3)2 concentration of (a) 60mM, (b) 80mM and (c) 100mM along with (d) Schematic of experimental set up.

In the hydrothermal process, the NPs are formed as a result of following reaction at  $150\,^{\circ}\text{C}$  temperature.

$$Ni(NO_3)_2 + 2NH_4OH \rightarrow Ni(OH)_2 + 2NH_4NO_3$$
 (6.1)

$$2\text{Ni}(0\text{H})_2 + \text{K}_2\text{S}_2\text{O}_8 + 20\text{H}^- + \text{H}_2\text{O} \rightarrow 2\text{Ni}00\text{H}.\text{H}_2\text{O} + 2\text{SO}_4^- + 2\text{H}_2\text{O}$$
 (6.2)

After the above reaction under high temperature and pressure conditions, NPs of Ni(OH)<sub>2</sub> get deposited on conducting ITO substrate. Presence of NH<sub>4</sub>OH and  $K_2S_2O_8$  has their individual roles in this process. The first one makes available the -OH sites to form the Nickel hydroxide and the second one is a crucial parameter for heterogeneous nucleation. The Ni(OH)<sub>2</sub> formed after the abovementioned reactions converts to NiO after annealing process (at 250  $^{\circ}$ C) as a result of following reaction[202]:

$$2\text{NiOOH. H}_2\text{O} + \text{e}^- \rightarrow \text{Ni(OH)}_2 + \text{OH}^-$$
 (6.3)

$$Ni(OH)_2 \rightarrow NiO + H_2O \tag{6.4}$$

All four reaction (Eq. 6.1– 6.4), as depicted in Figure 6.1d, explains the formation of NiO NPs by bottom-up approach. It is intuitive that a higher concentration of Ni(NO<sub>3</sub>)<sub>2</sub> will contain more Ni and O atoms and it is very likely to yield more amount of NiO as is apparent from Figures 6.1b & 6.1c as compared to Figure 6.1a. It will be interesting to see how this increased yield manifests itself in terms of morphology of the film. The phase purity and material characteristics of NiO NPs film for S1 sample has already been discussed in chapter 3 (section(3.1.1)) and now can be taken for geometrical analysis for knowing electron transport mechanism in FE study.

#### 6.2.2 Geometrical analysis

Though it is evident from Figure 6.1 that uniform deposition of NPs has taken place across the whole substrate for all the samples, some quantitative study of the same will be interesting and has been discussed below. Quantitative analysis of the SEM images (Figure 6.1a-c) has been carried out using Image J<sup>TM</sup> software. Surface plots obtained from selected portion on the SEM images show 3D representation of beautiful rose petal like structures as extracted using ImageJ<sup>TM</sup>. The ImageJ<sup>TM</sup> deduced surface plots representing sample S1, S2 and S3 clearly shows that the petal density increases with increasing concentration of precursor. Sample S1, prepared from minimum precursor concentration, contains petals like structures which appear more closer in samples (samples S2 and S3) prepared using higher precursor concentration. High concentration means presence of more reactants resulting in more end materials to give denser NPs. It is also clear from Figure 6.2a that, on increasing the precursor concentration, the petals not only become thicker but also gets packed more closely. This can be verified quantitatively by taking a closer look at these images along with SEM images of Figure 6.1a-c through line profiling. Line profiles, obtained from ImageJ<sup>TM</sup>, were analyzed to obtain petal thickness and petal

density. To define the average petal density and thickness, multiple line profiles were drawn on the SEM image frame for all the three samples. The concentration dependent petal density and petal thickness show a direct proportionate variation (Figure 6.2b).

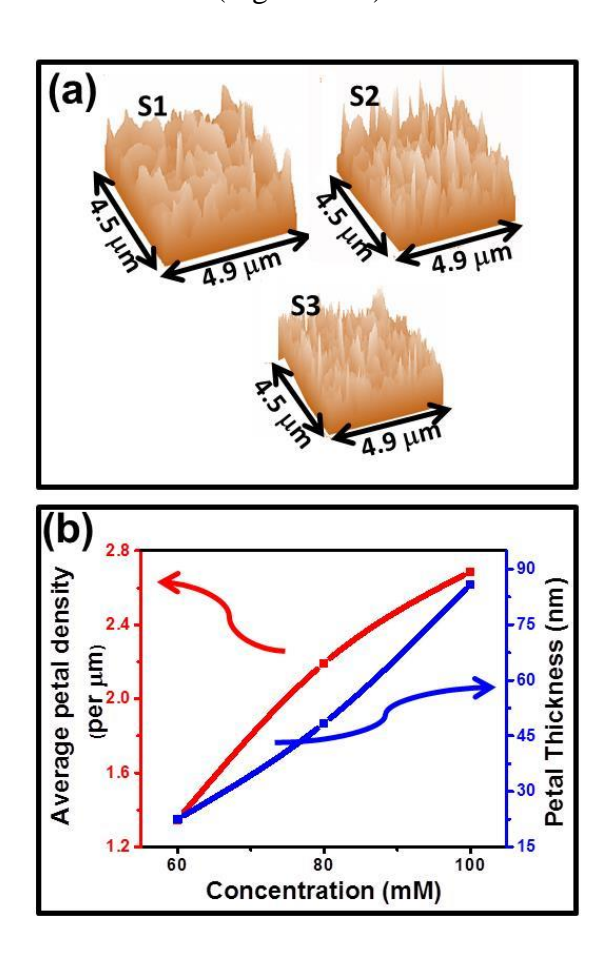


Figure 6.2: Surface plots extracted from SEM images using ImageJ and (b) Variation of average petal thickness and petal density as a function of precursor concentration

It is also interesting to see in Figure 6.2b that on increasing precursor concentration the petal density tends towards getting saturated (left Y-axis) whereas the thickness starts dominating at higher concentrations (right Y-axis). Figure 6.2b has been used to estimate the linear porosity (in percentage) by taking the ratio of overall cumulative coverage of the petals over the total length under analysis. It is interesting to see that linear porosity decreases as a function of concentration (Table-6.1). This is consistent with abovementioned results (Figure 6.2(b)) as porosity reduction is a direct consequence of continuously increase in the

thickness of the NPs as well as increased packing density i.e, decrease in inter-petal distance.

Table 6.1: Details of linear porosity as a function of precursor concentration.

Sample Name	precursor Concentration	Linear Porosity
S1	60 mM	85.6 %
S2	80 mM	69.3 %
S3	100 mM	22.1 %

#### **6.2.3 Electron Field Emission**

As mentioned above, FE is one such application where surface morphology plays very important roles and it directly affects the local electric field when kept under external bias. Thickness and separation between two emitting source (NPs in the present case) are other factors governing the electron emission as inappropriate substrate may kill the electron emission. Thin nanostructures, not very closely packed, are best suited for FE applications. Less porous medium are highly dense and has smaller aspect ratio. It sees very high screening effect and thus is poor electron emitter. To take both of these factors into account linear porosity and product of petal density & petal thickness may be helpful in identifying the optimal condition for FE. It is appropriate to define a term quality factor,  $\xi$ , defined by product of the petal thickness and petal density to identify suitable samples for FE. The same has been calculated for all the three samples and summarized in Table-6.2. Smaller the value  $\xi$ , more suitable will be the sample for FE which is sample S1 in the present case (Table-6.2).

Table6.2: Details of parameters calculated by Image J software.

Sample name, Concentration (mM)	Petal Thickness (nm)	Petal density (per μm)	Petal density x Petal Thickness (ξ) (x 10 <sup>-3</sup> )
S1, 60	22	1.34	29.6
S2, 80	48	2.19	106.2
S3, 100	85	2.68	230.2

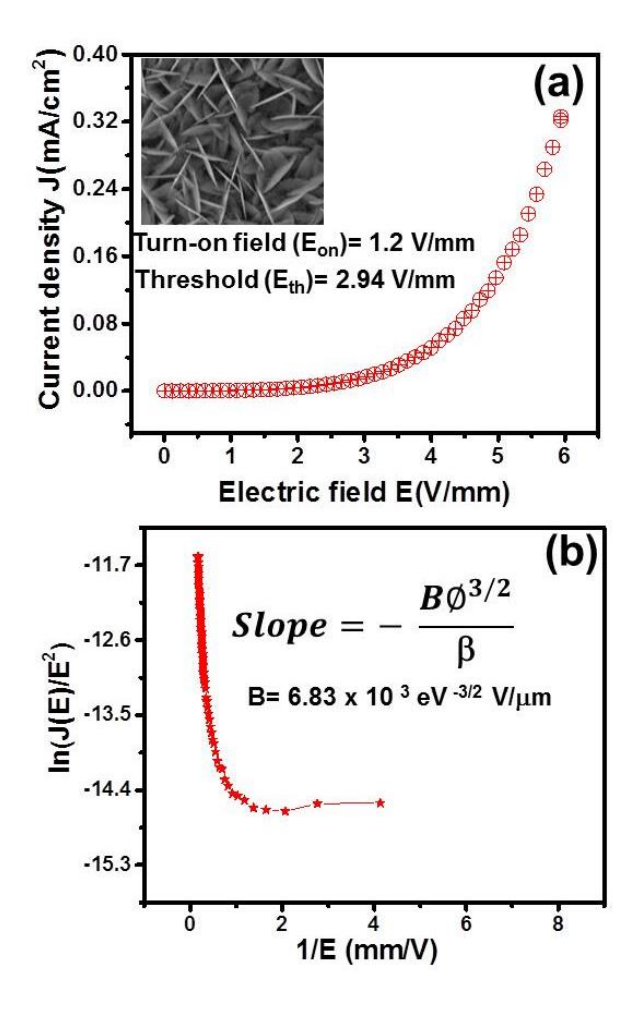


Figure 6.3: FE from a specially characterized NiO NPs with turn on field 1.2 V/mm (a), F-N plot for finding the estimate value of enhancement factor  $\beta$  (b).

The FE properties of sample S1 has been studied where the electron emission was measured by putting an electrode 0.5 mm from the sample S1 in planner geometry. Figure 6.3a shows the emission electron current density (J) as a function of applied electric field (E). The J-E curve follows the F-N relation (Eq. 1.9) below (section 1.5), The observed FE from NiO NPs is very efficient with a turn-on field of 1.2 V/mm and threshold field of 2.94 V/mm. The field enhancement factor of 5713 thousand has been calculated from the sample using the F-N Eq., described using Eq. 1.9, shown in the Figure 6.3 (b). This affirms the hypothesis that morphology may be predesigned prior to its use in a given application and in the present case the same can be done by appropriately controlling the precursors' concentration for field emission. Thin nanothorns are present on these NPs which enable one to achieve such a good FE from the sample.

## 6.3 Field Emission from Packed TiO<sub>2</sub> nanorod

Titania (TiO<sub>2</sub>), a member of the metal oxide group of materials and said to be a nature's gift to the mankind, has been intensively studied in last couple of decades in various applications like, resistive memory[203,204], solar cell[205], photocatalysis[206] etc. Application specific nanomaterials need to be not only designed but also be synthesized by an appropriate method as different methods have its own advantages and disadvantages. Each of these applications exploits a particular aspect of the nanomaterials like the surface morphological variation tuning which the best possible property can be obtained, as described in the previous section. FE is one such application which highly depends upon the surface morphology and is the main problem to be discussed here [207].

An improved electron FE property from vertically aligned TNRs (TNR) grown over the FTO glass substrate, prepared by hydrothermal technique (section 2.4.2). The TNRs having high aspect ratio with appropriate separation were prepared by optimizing the nucleation temperature. The TNR density has been optimized to cease the screening effect in closely

packed nanorods. The well aligned rods have been designed so that the applied field is equally distributes on each rod to improve the electron emission. Therefore, before going into the electron emission property of TNR, it must be checked the alignment of nanorod geometry and their surface analysis.

#### 6.3.1 Structural analysis and characterisation of TNR

Morphology of the TNRs deposited on FTO coated glass substrate have been examined using SEM. The SEM shown in Figure (3.3e & 3.3f) shows the homogeneously packed dense TNR with average packing density of ~10 NRs per micron as estimated using method reported in previous section using image J<sup>TM</sup> software. The TNRs appears to have grown vertically on the substrate, shown in Figure (3.3e & 3.3f) Information about the height of TNR has been obtained by taking the cross-sectional SEM image. Figure 3.3f clearly shows that the nanorods of TNR having height of about 2μm are by-and-large aligned. Therefore, the combined morphological study of top view and cross-sectional view gives the high aspect ratio of TNR which can be suitable parameter to become an efficient field emitter. Crystallinity of these individual TNR have already been studied using HRTEM and analyzed (section 3.1.2) in detail.

Additionally, the structural as well as optical properties of prepared TNRs, studied using XRD and UV-Vis spectroscopy, reveals that the crystalline rutile phase of TiO<sub>2</sub> with band gap of 3.19 eV is formed (section(3.1.2.1). An enhanced band gap from TNR, as compared to its bulk counterpart (3.0 eV), is a consequence of QCE as the confined carriers often lead to band gap enhancement. The combined study hints to the phase purity of crystalline TiO<sub>2</sub> martial and their nanorod geometry shows high aspect ratio, thus can be takes for the FE study.

#### **6.3.2 Field Emission from TNR**

Besides the wide band gap of TiO<sub>2</sub>, it has some unique features to make it different from other transition metal oxide like its application in electronics. These features can be obtained in terms of high aspect ratio

(length to diameter) and less porosity for one-dimensional TNR. Since the high aspect ratio of TNR indicate the appreciable electron emission property due to high electron density at the tip of nanorods with vertical alignment being an additional advantage. Emission of electron from the nanostructure in high vacuum displays the promising FE applications. The FE properties have been measured from abovementioned TNR@FTO in high vacuum chamber. An anode of area 0.72 cm<sup>2</sup> in the form of a circular plate made up of copper was used in parallel plate geometry for FE measurement. Background image of Figure 6.4a, depicts the geometry of FE apparatus in two electrode system with TNR deposited sample used as cathode (to emit electrons) and the copper sheet being the anode (to accept electrons) completing the cycle of electron current. The distance between these two electrodes was fixed at 0.5 mm. Figure 6.4(a) represents the FE current observed from TNR on the application of external voltage and obtained graph between J v/s E follows the typical FE data trend of Eq. 1.8. Experiments were carried out in high vacuum chamber which was at 10<sup>-5</sup> mbar pressure. The conversion of FE current into the F-N Eq. using Eq. 1.9 and plotted in Figure 6.4b to known the FE parameter for which every material is checked for its better FE property.

Since the FE phenomenon is based on quantum mechanical tunneling effect from the tip of nanostructure inside a high vacuum, it is expected that a potential distribution at the surface of nanostructure will play an essential role in facilitating the tunneling of the electrons. Under high vacuum condition, this potential distribution is known to take the shape of a triangular barrier with a round edge (Eq. 1.7 chapter 1) From Eq. 1.5 & Eq. 1.6. It is confirmed that, to draw the significant FE current, the electron potential distribution must be either tailored by applying external field (trivial) or through internally induced perturbations.

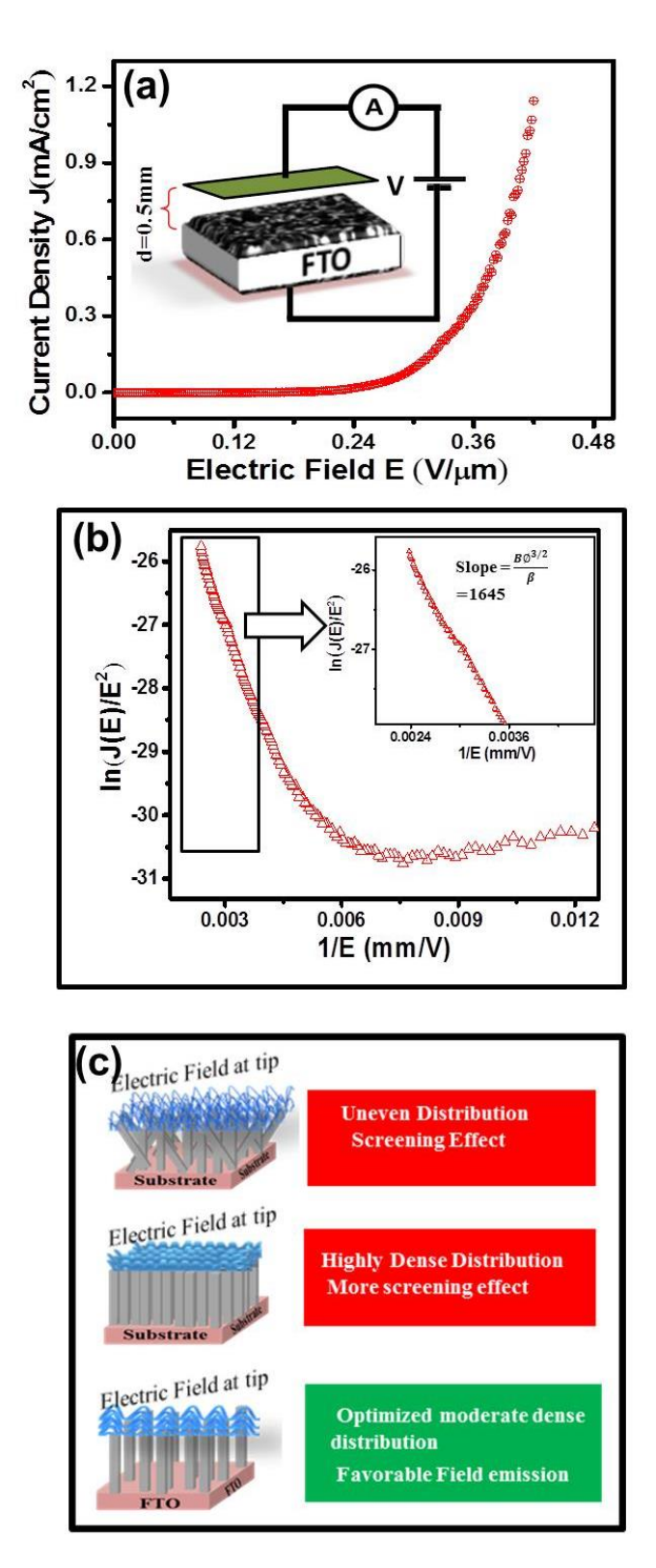


Figure 6.4: (a) FE(J-E plot) from  $TiO_2@FTO$  nanorods measured in a parallel plate geometry (inset). (b) F-N plot in linear relationship for estimation of enhancement factor, (c) Schematic representation of favorable (the green panel) and non-favorable (red panels) situations for efficient field emission.

Inset of Figure 6.4b shows the estimation of intercept (on the 1/E axis) and slope of linear region which provides the information of  $\beta$  and threshold field respectively. The estimated values of  $\beta$  and threshold field ( $E_{th}$ ) are ~37 thousand and 0.3 V/µm respectively. A significant enhancement factor of ~37 thousand is helping in achieving a low threshold field of less than half a volt per micron. The observed values of  $\beta$  in the present TNR are better than those reported from various morphologies of  $TiO_2[84,85]$ . The values of  $\beta$  and  $E_{th}$  depend upon the structure of nanostructures' tip, which in turn govern the emission, and needs to be analyzed to understand the improvement in the enhancement factor. The properly vertically aligned sharp nanoneedles of TNR give the advantage in improving the FE by restricting the shielding of electric field to get randomized from uneven emission surface if available otherwise. The appropriateness of distance between two TNRs is another factor playing a role in improving the FE as too closely packed nanorods kills FE due to screening effect. This has been summarized using a schematic shown in Figure 6.4c where the favorable condition has been shown in the bottom most panels (green) whereas two non-favorable conditions have been shown in top and middle panels (red). Another important parameter used in quantification of FE is the turn-on field, defined here as the electric field required to get a current density of 0.01 μA/cm<sup>2</sup>. The turn on field for the TNR is obtained to be equal to 0.2 V/µm which is better as compared to various TiO2 NSs reported in literature. Thus, vertically aligned TNR@FTO prepared by hydrothermal method seems to improve the FE properties as evident from the low values of threshold & turn-on fields and high value of enhancement factor. High enhancement factor observed for this case may be defined by the presence of less screening effect and conducting nature of substrate. It can be well certified that the obtained well aligned TNR are capable of being used in FE application.

## **6.4 Alternate Analytical FEFramework**

An improved framework is being described here to validate the FE results discussed above and will be compared with the existing analysis. A new set of parameters for quantification of electron emission quality has been proposed for analyzing the different FE properties of NiO and TiO<sub>2</sub> nanostructures. The proposed analytical method enables one to understand the FE properties in better sense as compared to the traditionally used framework, namely the F-N approach. The proposed model improves the analysis by introducing a boost-factor to take care of the FE data in totality unlike the traditional method where only currents for higher electric fields are considered. The proposed model is found to be more appropriate as it addresses the ambiguity present in the previously used method. A quantum mechanical approach has been adopted for explaining the improved FE properties from these nanostructures using the concept of tunneling probability.

#### **6.4.1 Background study**

As mentioned above, a new analytical framework has been developed for analyzing FE properties of nanomaterials by appropriately addressing the discrepancies of the existing model. Need of a new methodology can be appreciated by the fact that the existing F-N Eq. (the straight line) uses the work function of bulk material (for calculation of  $\beta$ ) whereas the electron emission takes place from the nano form of the material. It is a well-known fact that electronic structure of a nanomaterial is different from its bulk counterpart due to discretization of the energy levels enforced by QCE[32,208-216]. Noncompliance to the use of actual effective work function of the nanomaterial in analysis and deviation of the actual data from straight line insists that alternate analysis should be done by considering the J-E curve for all E values and by taking into account the modified work function. The proposed framework uses the F-N equation, rather than the processed one, to fit the complete experimental J-E data (instead of the selected one as in current practice) and yield redefined parameters (defined as boost-factor) as fitting parameters. This factor explains how modified electronic structure from the nanomaterials helps improving the FE by decreasing the barrier height as well as barrier width thus increasing the probability of tunnelling. The proposed model has been validated by analyzing FE properties from nanostructures of NiO and TiO<sub>2</sub> grown in naopetals and nanorods shapes respectively. The proposed model successfully explains the enhanced electron emission, a quantum mechanical phenomenon, from these two nanostructures by adopting a quantum mechanical approach.

#### **6.4.2** Origin of New Framework: Validations

Currently, the theoretical framework based on F-N formulation is used as the most acceptable methodology to quantify FE quality of a sample. FE mechanism is understood using the predicted J-E relationship (Eq. 1.8) (Eq. 1.8 followed by the F-N Eq. 1.9). Eq. 1.9 represents, at least apparently, a straight line between ln (J/E<sup>2</sup>) and 1/E, whose slope is used to determine the value of  $\beta$ . However, a well-accepted model for understanding FE properties of material, it is important to mention some of the inconsistencies in the F-N equation. These inconsistencies induce ambiguity in the analysis which make the understanding of FE incomplete because the field enhancement factor (B) used as quality factor, is estimated from Eq. 1.9. The origin of ambiguity lies in the fact that  $\beta$  is estimated from the slope of the so called straight line (Eq. 1.9) which is not true for all values of E. In other words, this Eq. expresses a straight line only for the high electric field values. Thus the quality factor estimated from only a portion of data should not be treated as the representative of the FE behavior in the global context. Since FE is a display device based application where emission current at any electric field is equally important thus defining these parameters by considering a limited data is likely to cease some information about the true FE properties of a material. Actually there is no reason why the whole I-V data should not be seen in completeness to give the true picture of a material. Keeping this point in view, a completely new methodology has been adopted here to analyze the FE characteristic by taking examples of both the metal oxide nanostructures.

It is proposed to use Eq. 1.8 as the master Eq. which can be rewritten as Eq. 6.5 after simplification:

$$J = \eta E^2 e^{-\zeta/E} \tag{6.5}$$

where,  $\eta = \frac{A\beta^2}{\phi_0}$  &  $\zeta = \frac{B\phi_e^{3/2}}{\beta}$  are the redefined master parameters with A & B being the same parameters defined above. The values of  $\zeta$  and  $\eta$ can be estimated by fitting the observed J-E curve with Eq. 6.5 by taking these two as the fitting parameters. When the known values of A & B are used,  $\beta$  &  $\phi_e$  remains the only parameters to be calculated from these two obtained values corresponding to the best fit. This gives the values of effective work function from the following Eq. obtained using simple algebra:  $\phi_e = \left(\frac{\zeta}{B}\right) \sqrt{\frac{\eta}{A}}$ ; where  $\phi_e = \chi \phi$  with  $\chi$  as the "boost factor" that explains the factor by which the work function gets an effective boost as compared to the bulk counterpart and can be calculated by simply taking the ratio of calculated  $\phi_e$  and the bulk work function value φ. As the word itself mean, it is the factor by which the FE changes in nano materials as compared to the bulk counterpart. The main nanostructures' property from where the difference starts is the change in energy level discretization, which will further affect the work function of material and the potential profile of tunnelling electrons. In the quantum mechanical regime for bound electrons inside the nano dimension offers effectively less potential width for tunnelling of electron, which result in higher FE current compared to the bulk phase where quantum effects play little role. To make the whole description easy for nano-dimension, the terminology 'boost factor', introduced for quantification of combined role of work function and tunneling width, is used for elaborating the FE phenomenon in the new framework which will be elaborated later on.

#### 6.4.2.1 Validation using NiO NPs and TNR

As mentioned above (sections 6.2 & 6.3) the NiO &  $TiO_2$  nanostructures result in different morphologies with ~20 nm thick petals of NiO and ~40nm thick  $TiO_2$  NRs and display a well-defined FE current behavior as

mentioned in figures 6.5a & 6.5b. The FE current, generated as a result of tunnelling of electron from a sample, varies differently as a function of applied field for NiO and TiO<sub>2</sub> due to different morphologies which in turn results in different field profile on the tip of the nanostructure, as shown in figures 6.5a & 6.5b. The obtained behaviour of current for both the samples is clearly pointing out that the emission nature of material is depending on the morphology. The main difference between the FE characteristics of NiO NPs (Figure 6.5a) and TiO<sub>2</sub> NRs (Figure 6.5 b) is visible in terms of observed current density at a given electric field. Figure 6.5 clearly shows that NiO NPs are far better field emitters as compared to TiO<sub>2</sub> NRs. Amongst various parameters affecting the tunneling; tunneling probability is a factor that can be used to understand the present observation. The tunneling probability is known to be inversely proportion to the width of potential barrier, which may be tuned by changing the surface morphology, physical properties of material, nature of substrate, and the vacuum level. Less electric field is required to initiate the emission of electron means more tunneling probability of electron from NiO NPs in comparison to TiO2 NRs. The study of morphology dependent FE is a well- known phenomenon and has been reported. Another factor that affects the tunneling probability, and thus the FE, is height of potential barrier, which is in the present case is dictated indirectly by the (effective) work function of the nanostructures. More details about the effect of these two factors (the tunneling width and work function) on tunneling probability will be discussed later on.

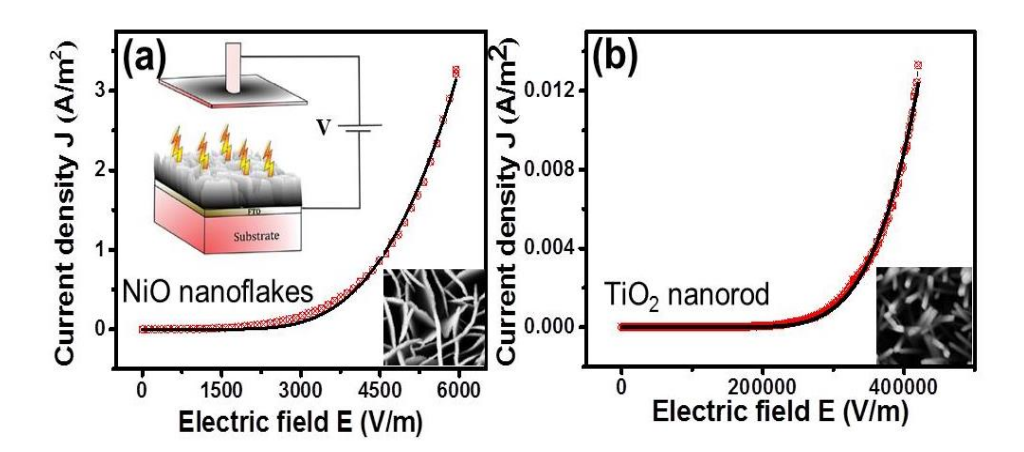


Figure 6.5: FE current density as a function of applied electric field for (a) NiO NPs (schematic of electrode geometry in top inset) and (b) TNRs. Bottom insets in (a) and (b) shows portion of corresponding microstructures.

Table 6.3: Summary of FEparameters and obtained master fitting parameters along with boost factor and effective work function for NiO NPs and TNRs

Sampl e name	Maximu m current density (A/m²)	Master paramete r 'η'	Master paramete r 'ζ'	Work function (bulk)	Effectiv e work functio n (\phi_e) (eV)	$\mathcal{X} = \frac{\phi_{eff}}{\phi}$
NiO	3.2	8.54x10 <sup>-7</sup>	1.3 x 10 <sup>4</sup>	4.2	1.4 x 10 <sup>-6</sup>	3.3 x 10 <sup>-7</sup>
TiO <sub>2</sub>	0.01	7.5 x 10 <sup>-</sup>	1.9 x 10 <sup>6</sup>	4.3	5.9 x 10 <sup>-7</sup>	1.3 x 10 <sup>-7</sup>

Therefore, the FE data from NiO NPs and TNR has been fitted using the proposed new Eq. 6.5. The master parameters ( $\zeta$  and  $\eta$ ), obtained corresponding to the best fit, have been summarized in Table 6 for both the samples. Table-6.3 also lists the calculated values of redefined

"boost factor" as well as the effective work function for both the samples.

The importance of the master parameters, and thus estimated  $\phi_e$  & boost factor  $(\chi)$ , is that it comes from the experimentally observed measurable quantity J(E) thus leaves no ambiguity. An overview of the parameters in Table 6.3 makes it clear that NiO NPs displays much larger current density as compare to TNRs for a given value of E, this is likely because of the much discussed screening effect, which is playing a greater role in TiO<sub>2</sub>. Random distribution of TNRs creates the cloud of space charge around the tips of nanorods, because of which all charges generate the heating effect instead of ballistic tunnelling and thus result in low current. Very small values of  $\chi$  for both, NiO and TiO<sub>2</sub> nanostructures signify that the effective work functions are very small as compared to their bulk counterparts. The effective work function is somewhat analogous to the height of potential step when talked in the context of quantum tunneling. A shallow potential step means more quantum tunnelling probability. As a result the nanostructures, due to their smaller effective work function, are better field emitters as compared to their bulk counterparts. It is worth mentioning here that however the effective work function is smaller (as compared to NiO) for TiO<sub>2</sub>, it is a poor field emitter as compared to NiO because of the smaller boost factor (last column). Thus the boost factor, estimated from the fitting of the observed consolidated J-E data is true representation of the FE properties of a given nanostructure thus should be used as factor to quantify the quality of FE instead of traditionally used factor  $\beta$ .

Role of this quantum effect and quantum induced discretization of energy levels in improving FE from nanomaterials can be understood by comparing the band structures of a nanomaterial and that of its bulk counterpart as shown in Figure 6.6. For FE, the electrons need to be pushed through a tunneling barrier under an influence of applied electric field. Quantum mechanics enforces that higher electric field is required if the work function (the potential step) is more thus is difficult for

electrons to tunnel in bulk materials. Moreover, since the sizes of materials (thus the tunnelling width) are very large, it is virtually impossible for the electrons to tunnel in bulk form. This is depicted in Figure 6.6a where the left schematic shows continuum of electronic energies and representative electron wave function in three different regions. The slanted plane shown by dotted boundary is the potential profile, under an applied bias, which will remain horizontal otherwise to represent the potential step when not placed in an electric field. The right panel in Figure 6.6a shows representation of the same potential step under the FE measurement set up. When the bias is applied, the electrons at the surface of the material (shown as black dots) needs to tunnel through a distance  $\tau_b$  so as to reach the "anode" (with the material connected to cathode) to give (field emission) current. It is worth mentioning here that the most energetic electrons (the ones at the top of the energy band) have energy equal to the work function  $(\phi_b)$ . If somehow the electrons can achieve some higher energy levels (if available in the material) then these electrons will need to tunnel smaller width.

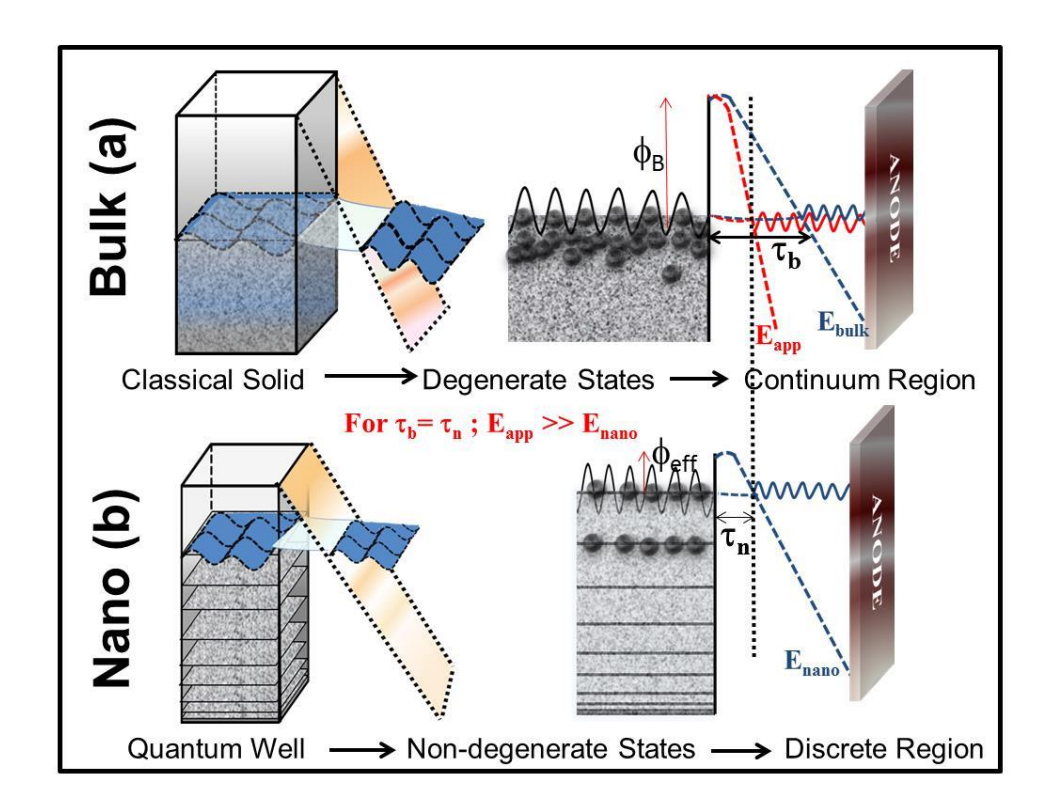


Figure 6.6: Schematic energy band representation for depiction of electron tunneling from (a) bulk material and (b) a nanostructured material. The energy levels and behavior of electron wave-function in different regions with dotted plane as the potential profile under applied electric field is shown in the left panel. The right panel shows the effect of quantization of energy bands on effective work function ( $\phi_{eff}$ ) which is less that the bulk counterpart ( $\phi_b$ ) and the tunneling widths ( $\tau_b \& \tau_n$ ) under two different applied biases ( $E_{app}$  and  $E_{nano}$ ).

This is possible due to the slanted nature of the effective potential barrier. The reason for this slanted nature of the potential step has been discussed earlier (section 1.5.1, chapter 1). The latter situation is possible in nanomaterials due to energy quantization leading to opening of energy bands (Figure 6.6b). When miniaturized to form nanomaterials, the energy distribution is completely changed and gets discretized with separation (between the energy levels) varying as a function of size. The energy discretization helps the electrons to get filled up to a level, closer to the vacuum level. This helps tunneling in two ways, firstly, the electrons are now filled more close to the vacuum level (represented by an effective work function  $\phi_{eff}$  which is less than its

bulk counterpart  $\phi_b$ ) which reduces the potential step height. This in turn increases the tunneling probability. Secondly, now the surface electrons need to tunnel a relatively smaller width  $(\tau_n)$  as compared to the bulk width  $\tau_b$ , (Figure 6.6b right panel). As a consequence of reduction in effective potential step height and effective tunneling width, an exponential improvement in the tunneling probability becomes obvious as explained in the section.

The above-mentioned double boost, the reduction in potential step height and experiencing lesser tunneling barrier allows easy FE from nanomaterials. As mentioned above, this boost is quantified using the boost factor  $\chi$ . This transition of energy levels getting non-degenerated once the material moves from its bulk to nanoscale due to symmetry breakdown yields better electron emission. In other words, bulk materials show the symmetric behavior in all dimensions, which has degeneracy of certain order which makes the continuum region of filled electronic state shown in Figure 6.6a. In contrary, the nanomaterials has only one confined dimension which results in all levels to get split into different nondegenerate energy states shown in Figure 6.6b. It is also clear from figure 6.6 (right panels) that if one want to achieve a smaller tunnel width, equivalent to the one in nano case  $(\tau_n)$  than higher electric field (E<sub>app</sub>) needs to be applied as compared to the one in nanomaterials (E<sub>nano</sub>). This is consistent with the values observed from the experimental data from both the nanomaterials as summarized in Table 6.3. This scenario can be better understood quantitatively using the present analysis where "boost factor" is considered as compared to the traditionally used "field enhancement factor" as prescribed by the proposed analytical framework. It is also important here to mention that the new framework does not alter the basic underlying concept of FE and only rearranges the master F-N Eq. thus can be used for analysis of FE properties of any nanomaterials capable of showing electron emission. The above-mentioned framework has been validated using FE properties of Si nanowires and has been summarized in Appendix A2. The fitting of the obtained FE data with the new framework also shows consistence behavior and validates the new rearranged formula.

# 6.5 Summary

Surface morphologies of hydrothermally grown NiO NPs and TNR are found to be dependent on the precursor's concentration at a given deposition and annealing temperature. In case of NiO, on increasing the precursor's concentration, the linear petal density increases and tends to saturate whereas the petal thickness keeps increasing within the concentration upto 100mM. Sample prepared with 40mM precursor concentration exhibited very good FE properties with turn-on field of 1.2 V/mm and threshold field of 2.94 V/mm resulting in a field enhancement factor of more than 5 million. Nanorods of TiO<sub>2</sub>, besides high aspect ratio, moderate nanorods' density and good alignment of nanorods, leads to the enhancement in FE. The moderate nanorods density keeps these rods at appropriate distance to cease the screening effect, which take place when the rods are too closely packed.

An inclusive new methodology, developed using quantum mechanical principles, for analysis and explanation of FE from nanostructures is found to be more comprehensive as compared to the traditional framework which uses "field enhancement" as the most significant parameter. In the new framework a new parameter "boost factor" is defined which takes into account two most important factors, energy discretization & its effect on effective work function as well as the reduction in effective tunnelling width which helps in easy electron FE from nanostructures. Analysis of FE from two different oxides (NiO and TiO<sub>2</sub>) and two different morphologies (NPs and nanorodss) validates the proposed analysis. The boost factor and effective work function from both the nanostructured samples, calculated using the current platform, represent the observed J-E curve for all values of electric field unlike the case of traditionally used analysis where only high electric field J-E curves are taken into account. In other words, the conclusions pertaining to FEdrawn using present model represents the complete data thus takes

care of the incompleteness/ambiguity that's latent in the previously used analysis. The inclusion of QCEs, inherently taking place in nanomaterials, in the analytical framework is in the root of the completeness of the proposed analysis.

# Chapter 7

# Conclusion, Summary and Future Scope

Major conclusions of the research work reported in this thesis are being summarized below along with the scope of future extension of the work.

#### 7.1 Conclusions and Summary

#### 7.1.1 Electrochromic Display

- Material characteristic for electrochemical properties have been studied for different inorganic and organic material in detail along with establishing the color changing mechanism.
- Different methods have been chosen for preparing the solid thin film electrode for better electrochromism and various parameter optimized for appropriate composition.
- 3. Electrochromic properties of TMO electrodes after proper characterization have been studied and their merits/demerits underlined for further studies and possible applications.
- 4. Spectroelectrochemistry measurement at individual EC electrode for in-situ optical spectroscopy has been performed for spectroscopic study and studied the factor influences the performances.
- 5. Electrodeposition techniques has been selected for making smooth, more adhesive, more homogenous, dense thin film of cobalt oxide which lead to investigate the better switching response for optical modulation.
- 6. Designing electrochemical set up containing EC electrodes in an appropriate electrolytic medium has been used to determine how each electrode possess its EC behaviors with applied bias.

- Therefore, EC double layer display has been designed through a flip chip techniques.
- 7. Two different combination of all-inorganic and inorganic /organic (say hybrid) device suggests that the improved EC performances and multicolor EC behavior is possible for bilayered geometry.
- 8. A device fabricated using the organic (Viologen) -inorganic (Co<sub>3</sub>O<sub>4</sub>) hybrid components, showed a CCr of 66% with a switching time of 500ms with a low operation voltage of 1.8V. As a result, the device showed a coloration efficiency of 368 cm<sup>2</sup>/C and remained stable for more than 120 switching cycles.
- 9. All-inorganic device of Co<sub>3</sub>O<sub>4</sub>-PB shows a fast response (1.5s) and power efficient (246 cm<sup>2</sup>/C) performance with a good CC (40%) and stability (more than 300 switching cycles) maintaining the robust nature of the inorganic EC family which switches between blue, green and brownish colors with a small bias of less than couple of volt.
- 10. In-situ bias dependent spectroscopic experiments including Raman spectroscopy have been carried out during device operation to establish and understand the working mechanism of bias induced color switching of fabricated ECDs.
- 11. In-situ Raman spectroscopy prove to be a handy and non-destructive tool to track bias induced redox changes of active materials involved in electrochromism of the device. It revealed bias induced changes in the redox state of interfacial layers and also spectroscopically see the live information and deformation of redox species.
- 12. The overall EC performances of inorganic material can be increased at some extant by choosing these suitable parameters and combination of materials and can also be enhance on preparing the nanomaterials in different chemical composition which comes in the category of binary, ternary mixed metal oxides and in oxyfluorides.

- 13. The binary NiCo<sub>2</sub>O<sub>4</sub> nanoneddles based electrode shows color switching between whitish translucent and dark brown as examined using in-situ absorption spectroscopy. An encouraging optical contrast of 50%, with an application of only 2V bias has been observed, which is one of the best operating voltages in the inorganic EC materials' family.
- 14. These materials with different nano-architecture may exhibit additional application in addition to electrochromism. Such multifunctional application from different nanostructures has been explored in various transition metal oxides.

#### 7.1.2 Bifunctional role

- Hydrothermally grown microporous NiCo<sub>2</sub>O<sub>4</sub> nanoneddle structures, showing optical and electrochemical modulations under applied biased and under glucose addition respectively, are found to be good candidate for dual application in electrochromism and Glucose sensing.
- 2. These NiCo<sub>2</sub>O<sub>4</sub> nanoneddle, grown on carbon cloth electrode, show selective sensitivity towards glucose as reflected in terms of increased electrochemical activity in the presence of glucose whereas it shows a passive behavior towards Ascorbic acid, Uric Acid and Folic acid.
- 3. Oxidation of glucose to gluconate, is responsible to increase the current response, lead to sensitivity of 3000 μA/mM/cm² for the given architecture due to availability of more exposed area for more redox reaction to take place.
- 4. Metals like Ni and Co in its oxide (NiCo<sub>2</sub>O<sub>4</sub>) form opens a new possibility towards electrochemical application for showing multifunctional application.

### 7.1.3 Field Emission Display

 Surface morphologies of hydrothermally grown NiO NPs and TNR are found to be dependent on the precursor's concentration at a given deposition and annealing temperature.

- 2. Sample prepared with 40mM precursor concentration exhibited very good FE properties with turn-on field of 1.2 V/mm and threshold field of 2.94 V/mm resulting in a field enhancement factor of more than 5 million.
- 3. Nanorods of  $TiO_2$ , besides high aspect ratio, moderate nanorods' density and good alignment of nanorods, leads to the enhancement in FE and two orders of magnitude enhancement in the electric field has been observed for this kind of geometry giving improved turn-on field and field enhancement factor of 0.2 V/ $\mu$ m and 37 thousands respectively.
- 4. An inclusive new methodology, developed using quantum mechanical principles, for analysis and explanation of FE from nanostructures is found to be more comprehensive as compared to the traditional framework which uses "field enhancement" as the most significant parameter.
- 5. In the new framework a new parameter "boost factor" is defined which takes into account two most important factors, energy discretization & its effect on effective work function as well as the reduction in effective tunneling width which helps in easy electron FE from nanostructures and validated on two results.

## 7.2 New Findings Reported in the Thesis

- 1. Electrodeposition technique for deposition of solid thin film found much favorable for showing the electrochromism with better performances and can be act as a suitable auxiliary electro to improve the other EC of inorganic and organic materials.
- 2. The tri-EC device of Co<sub>3</sub>O<sub>4</sub> and PB electrode displaying three different colors within the 1.5 sec response time.
- 3. In-situ bias dependent Raman spectroscopy has been demonstrated for investigating of working mechanism of an ECDs.
- 4. Suitable metal doping can enhance the oxidation state of material lead to bifunctional role of those materials.

5. Morphology of nanostructure having high aspect ratio also displays many applications beyond the electrochemistry like FE and has been seen in nano-NiO and nano-TiO<sub>2</sub> architectures.

#### 7.3 Future scope of the work

- 1. Designing the Fast, Flexible, Wearable, Stretchable, Compact and Robust ECDs.
- 2. EC displays with other application such as memory devices, Supercapacitor, UV sensing, Heat shielding etc.
- 3. Investigating other materials' to their different morphologies, electrical properties and stability for energy storage, sensing, water splitting like applications.
- 4. Optimizing the parameter like film thickness, precursor concentration, deposition parameter, role of electrolyte and etc. will be considered for future work.
- 5. Fabrication of device at large scale for commercialization purpose.
- 6. Making use of dual wavelength filter device for waveguide purpose.
- 7. To search the EC active species in natural herbal product and their implication for other application in electronic and biomedical fields.
- 8. Raman Spectroscopy of different oxides, biomolecules for searching a new area of research toward application point.\
- 9. Exploring other characterisation techniques like XPS, TEM, Mass spectroscopy, in detail and finding the correlation to others.
- 10. There will always be an effort to focus on designing a device with multiple embedded applications.

The thesis can be concluded with the following lines:

"Ideas do not always come in a flash but by diligent trial-and-error experiments that take time and thought".

--- Charles K Kao (fibre optics)

## **Appendix**

## A1. Diode behavior of hybrid ECDs

Figure A1 shows I-V characteristic of the fabricated hybrid solid state ECDs in which electrode containing EV ( $Co_3O_4$ ) is connected to negative (positive) terminal of battery. The device IV characteristic has been taken as the same biased condition from -1 V to +1.8 V. As seen from this diagram, a much and significant current is flowing after +1.5 V, when -1.5 V will be at EV. However, the current starts going up from the +1 V and enhances after +1.5 V. Therefore, +1.5 V can be taken as threshold voltage of the device.

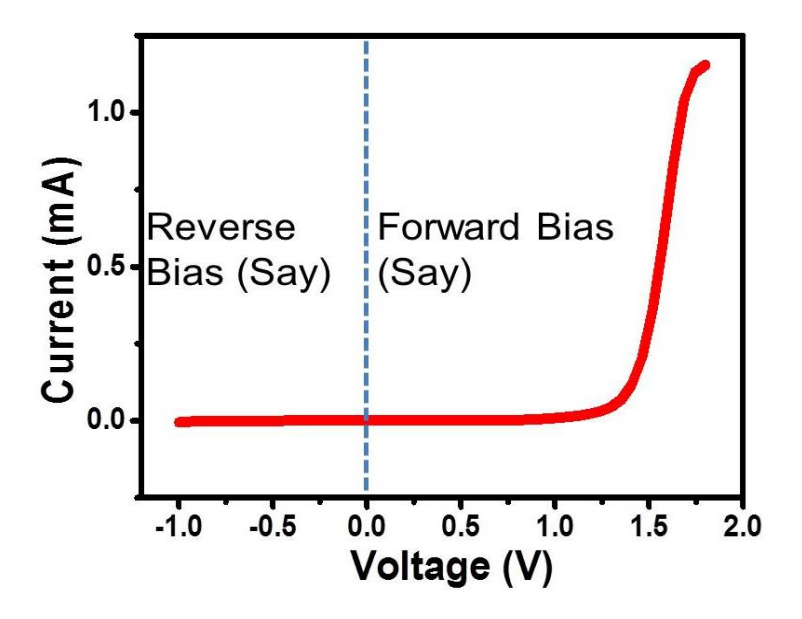


Figure A1: Current voltage (I-V) response of the fabricated solid state device

## A2. Quantifying Electron Emission from Silicon Nanowires using new framework

A consolidated new methodology, developed on the basis of quantum mechanical principles, for analysis and explanation of size dependent FE from silicon nanowires has been found to be more comprehensive as compared to the traditional framework. The new methodology, developed by introducing "boost factor", and "FE power density", successfully quantifies the observed FE from SiNWs prepared by using metal induced etching technique, shown in Figure A2.

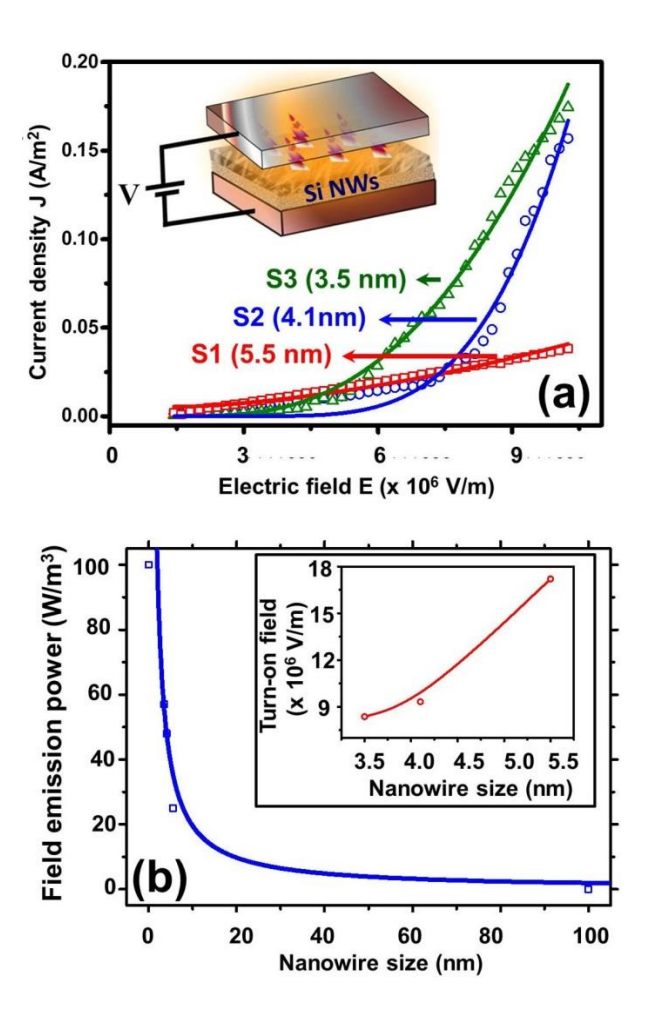


Figure A2: (a) FEJ-E curves for different SiNWs samples measured in diode geometry (inset) and (b) Variation of FE power as a function of SiNWs diameter along with variation of turn on field as a function of SiNWs diameter (inset).

The "boost factor" takes care of two most important factors, energy discretization & its effect on effective work function that reflects as reduction in tunneling width which helps in easy electron FEfrom nanostructures. Analysis of size dependent boost factor, effective work function and FE power density reveals that the redefined master parameters represent the actual FE from nanostructures'. The proposed model in a way completes the Fowler-Nordheim framework, mainly of generic nature and proposed for classic field emitters, to be used for nanostructures unlike the traditionally way where the experimental data are explained only partially. The inclusion of quantum size effects, inherently taking place in nanomaterials, in the analytical framework is the basic building block leading to the completeness of the proposed analysis as evident from the size dependent analysis.

## References

- [1] Book Review of What is What in the Nanoworld: A Handbook on Nanoscience and Nanotechnology, Completely Revised and Enlarged 2nd ed., J. Am. Chem. Soc. 130 (2008) 17204–17204. https://doi.org/10.1021/ja808460u.
- [2] R.F. Service, Nanotechnology Grows Up, Science. 304 (2004) 1732–1734. https://doi.org/10.1126/science.304.5678.1732.
- [3] G.L. Hornyak, A.K. Rao, Chapter 2 Fundamentals of Nanoscience (and Nanotechnology), in: M.R. Hamblin, P. Avci, T.W. Prow (Eds.), Nanoscience in Dermatology, Academic Press, Boston, 2016: pp. 15–29. https://doi.org/10.1016/B978-0-12-802926-8.00002-1.
- [4] J.A. Schwarz, C.I. Contescu, K. Putyera, Dekker Encyclopedia of Nanoscience and Nanotechnology, CRC Press, 2004.
- [5] C.P.P. Jr, F.J. Owens, Introduction to Nanotechnology, John Wiley & Sons, 2003.
- [6] R.D. Adams, Book Review of Nanomaterials Chemistry: Recent Developments and New Directions, J. Am. Chem. Soc. 130 (2008) 14019–14019. https://doi.org/10.1021/ja806755n.
- [7] M. Tulinski, M. Jurczyk, Nanomaterials Synthesis Methods, in: Metrology and Standardization of Nanotechnology, Wiley-Blackwell, 2017: pp. 75–98. https://doi.org/10.1002/9783527800308.ch4.
- [8] Handbook of Nanomaterials in Analytical Chemistry, Elsevier, 2020. https://doi.org/10.1016/C2018-0-00945-7.
- [9] Nanolithography | ScienceDirect, (n.d.). https://www.sciencedirect.com/book/9780857095008/nanolithography (accessed February 23, 2021).
- [10] H. Pan, Y.P. Feng, Semiconductor Nanowires and Nanotubes: Effects of Size and Surface-to-Volume Ratio, ACS Nano. 2 (2008) 2410–2414. https://doi.org/10.1021/nn8004872.
- [11] T. Takagahara, K. Takeda, Theory of the quantum confinement effect on excitons in quantum dots of indirect-gap materials, Phys. Rev. B. 46 (1992) 15578–15581. https://doi.org/10.1103/PhysRevB.46.15578.
- [12] M. Chamarro, C. Gourdon, P. Lavallard, O. Lublinskaya, A.I. Ekimov, Enhancement of electron-hole exchange interaction in CdSe nanocrystals: A quantum confinement effect, Phys. Rev. B. 53 (1996) 1336–1342. https://doi.org/10.1103/PhysRevB.53.1336.
- [13] V. Schroeder, S. Savagatrup, M. He, S. Lin, T.M. Swager, Carbon Nanotube Chemical Sensors, Chem. Rev. 119 (2019) 599–663. https://doi.org/10.1021/acs.chemrev.8b00340.
- [14] R.H. Tunuguntla, R.Y. Henley, Y.-C. Yao, T.A. Pham, M. Wanunu, A. Noy, Enhanced water permeability and tunable ion selectivity in subnanometer carbon nanotube porins, Science. 357 (2017) 792–796. https://doi.org/10.1126/science.aan2438.

- [15] A. Di Mauro, M.E. Fragalà, V. Privitera, G. Impellizzeri, ZnO for application in photocatalysis: From thin films to nanostructures, Materials Science in Semiconductor Processing. 69 (2017) 44–51. https://doi.org/10.1016/j.mssp.2017.03.029.
- [16] M. Sheikh, M. Pazirofteh, M. Dehghani, M. Asghari, M. Rezakazemi, C. Valderrama, J.-L. Cortina, Application of ZnO nanostructures in ceramic and polymeric membranes for water and wastewater technologies: A review, Chemical Engineering Journal. 391 (2020) 123475. https://doi.org/10.1016/j.cej.2019.123475.
- [17] A.A.M. Sakib, S.M. Masum, J. Hoinkis, R. Islam, M.A.I. Molla, Synthesis of CuO/ZnO Nanocomposites and Their Application in Photodegradation of Toxic Textile Dye, Journal of Composites Science. 3 (2019) 91. https://doi.org/10.3390/jcs3030091.
- [18] A. Tereshchenko, G.R. Yazdi, I. Konup, V. Smyntyna, V. Khranovskyy, R. Yakimova, A. Ramanavicius, Application of ZnO Nanorods Based Whispering Gallery Mode Resonator in Optical Immunosensors, Colloids and Surfaces B: Biointerfaces. 191 (2020) 110999. https://doi.org/10.1016/j.colsurfb.2020.110999.
- [19] B. Alfano, E. Massera, T. Polichetti, M.L. Miglietta, G. Di Francia, Effect of palladium nanoparticle functionalization on the hydrogen gas sensing of graphene based chemi-resistive devices, Sensors and Actuators B: Chemical. 253 (2017) 1163–1169. https://doi.org/10.1016/j.snb.2017.07.146.
- [20] M. Iqbal, Y.V. Kaneti, J. Kim, B. Yuliarto, Y.-M. Kang, Y. Bando, Y. Sugahara, Y. Yamauchi, Chemical Design of Palladium-Based Nanoarchitectures for Catalytic Applications, Small. 15 (2019) 1804378. https://doi.org/10.1002/smll.201804378.
- [21] M. Massaro, C. G. Colletti, G. Buscemi, S. Cataldo, S. Guernelli, G. Lazzara, L. F. Liotta, F. Parisi, A. Pettignano, S. Riela, Palladium nanoparticles immobilized on halloysite nanotubes covered by a multilayer network for catalytic applications, New Journal of Chemistry. 42 (2018) 13938–13947. https://doi.org/10.1039/C8NJ02932F.
- [22] X. Tang, P.-A. Haddad, N. Mager, X. Geng, N. Reckinger, S. Hermans, M. Debliquy, J.-P. Raskin, Chemically deposited palladium nanoparticles on graphene for hydrogen sensor applications, Scientific Reports. 9 (2019) 3653. https://doi.org/10.1038/s41598-019-40257-7.
- [23] R.S. Riley, E.S. Day, Gold nanoparticle-mediated photothermal therapy: applications and opportunities for multimodal cancer treatment, WIREs Nanomedicine and Nanobiotechnology. 9 (2017) e1449. https://doi.org/10.1002/wnan.1449.
- [24] S. Najmaei, Z. Liu, W. Zhou, X. Zou, G. Shi, S. Lei, B.I. Yakobson, J.-C. Idrobo, P.M. Ajayan, J. Lou, Vapour phase growth and grain boundary structure of molybdenum disulphide atomic layers, Nature Materials. 12 (2013) 754–759. https://doi.org/10.1038/nmat3673.
- [25] A. J, V. Ks, W. Cd, G. K, S. Y, C. Ct, D. J, P. E, H. Sj, G. Iv, C. P, G. Ak, N. Rr, Tunable sieving of ions using graphene oxide

- membranes., Nat Nanotechnol. 12 (2017) 546–550. https://doi.org/10.1038/nnano.2017.21.
- [26] J. Lahann, Nanomaterials clean up, Nature Nanotechnology. 3 (2008) 320–321. https://doi.org/10.1038/nnano.2008.143.
- [27] M. Zahn, T.A. Hatton, S.R. Khushrushahi, Magnetic colloid petroleum oil spill clean-up of ocean surface, depth, and shore regions, US20120211428A1, 2012. https://patents.google.com/patent/US20120211428A1/en (accessed February 23, 2021).
- [28] L.A.K. Staveley, The Characterization of Chemical Purity: Organic Compounds, Elsevier, 2016.
- [29] X. Xue, W. Ji, Z. Mao, H. Mao, Y. Wang, X. Wang, W. Ruan, B. Zhao, J.R. Lombardi, Raman Investigation of Nanosized TiO2: Effect of Crystallite Size and Quantum Confinement, J. Phys. Chem. C. 116 (2012) 8792–8797. https://doi.org/10.1021/jp2122196.
- [30] R. Gupta, Q. Xiong, C.K. Adu, U.J. Kim, P.C. Eklund, Laser-induced fano resonance scattering in silicon nanowires, Nano Lett. 3 (2003) 627–631. https://doi.org/10.1021/nl0341133.
- [31] R. Kumar, H.S. Mavi, A.K. Shukla, V.D. Vankar, Photoexcited Fano interaction in laser-etched silicon nanostructures, Journal of Applied Physics. 101 (2007) 064315. https://doi.org/10.1063/1.2713367.
- [32] P. Yogi, S. Mishra, S.K. Saxena, V. Kumar, R. Kumar, Fano Scattering: Manifestation of Acoustic Phonons at the Nanoscale, J. Phys. Chem. Lett. 7 (2016) 5291–5296. https://doi.org/10.1021/acs.jpclett.6b02090.
- [33] M. Ferrari, Cancer nanotechnology: opportunities and challenges, Nature Reviews Cancer. 5 (2005) 161–171. https://doi.org/10.1038/nrc1566.
- [34] D. Tiwari, S. Jakhmola, D.K. Pathak, R. Kumar, H.C. Jha, Temporal In Vitro Raman Spectroscopy for Monitoring Replication Kinetics of Epstein–Barr Virus Infection in Glial Cells, ACS Omega. 5 (2020) 29547–29560. https://doi.org/10.1021/acsomega.0c04525.
- [35] V.S. Saji, H.C. Choe, K.W.K. Yeung, Nanotechnology in biomedical applications: a review, International Journal of Nano and Biomaterials. 3 (2010) 119–139. https://doi.org/10.1504/JJNBM.2010.037801.
- [36] V. Labhasetwar, D.L. Leslie-Pelecky, Biomedical Applications of Nanotechnology, John Wiley & Sons, 2007.
- [37] S. Mishra, A.K. Mondal, S. Pal, T.K. Das, E.Z.B. Smolinsky, G. Siligardi, R. Naaman, Length-Dependent Electron Spin Polarization in Oligopeptides and DNA, J. Phys. Chem. C. 124 (2020) 10776–10782. https://doi.org/10.1021/acs.jpcc.0c02291.
- [38] A.K. Mondal, N. Brown, S. Mishra, P. Makam, D. Wing, S. Gilead, Y. Wiesenfeld, G. Leitus, L.J.W. Shimon, R. Carmieli, D. Ehre, G. Kamieniarz, J. Fransson, O. Hod, L. Kronik, E. Gazit, R. Naaman, Long-Range Spin-Selective Transport in Chiral Metal—Organic

- Crystals with Temperature-Activated Magnetization, ACS Nano. 14 (2020) 16624–16633. https://doi.org/10.1021/acsnano.0c07569.
- [39] S. Mishra, A.K. Mondal, E.Z.B. Smolinsky, R. Naaman, K. Maeda, T. Nishimura, T. Taniguchi, T. Yoshida, K. Takayama, E. Yashima, Spin Filtering Along Chiral Polymers, Angewandte Chemie International Edition. 59 (2020) 14671–14676. https://doi.org/10.1002/anie.202006570.
- [40] Y. Liu, M. Pharr, G.A. Salvatore, Lab-on-Skin: A Review of Flexible and Stretchable Electronics for Wearable Health Monitoring, ACS Nano. 11 (2017) 9614–9635. https://doi.org/10.1021/acsnano.7b04898.
- [41] Y. Yang, N. Sun, Z. Wen, P. Cheng, H. Zheng, H. Shao, Y. Xia, C. Chen, H. Lan, X. Xie, C. Zhou, J. Zhong, X. Sun, S.-T. Lee, Liquid-Metal-Based Super-Stretchable and Structure-Designable Triboelectric Nanogenerator for Wearable Electronics, ACS Nano. 12 (2018) 2027–2034. https://doi.org/10.1021/acsnano.8b00147.
- [42] C. Yan, W. Kang, J. Wang, M. Cui, X. Wang, C.Y. Foo, K.J. Chee, P.S. Lee, Stretchable and wearable electrochromic devices, ACS Nano. 8 (2014) 316–322. https://doi.org/10.1021/nn404061g.
- [43] D. Son, J.H. Koo, J.-K. Song, J. Kim, M. Lee, H.J. Shim, M. Park, M. Lee, J.H. Kim, D.-H. Kim, Stretchable carbon nanotube chargetrap floating-gate memory and logic devices for wearable electronics, ACS Nano. 9 (2015) 5585–5593. https://doi.org/10.1021/acsnano.5b01848.
- [44] T. Ozulumba, G. Ingavle, Y. Gogotsi, S. Sandeman, Moderating cellular inflammation using 2-dimensional titanium carbide MXene and graphene variants, Biomaterials Science. (2021). https://doi.org/10.1039/D0BM01953D.
- [45] Z. Bi, X. Li, Y. Chen, X. He, X. Xu, X. Gao, Large-Scale Multifunctional Electrochromic-Energy Storage Device Based on Tungsten Trioxide Monohydrate Nanosheets and Prussian White, ACS Appl Mater Interfaces. 9 (2017) 29872–29880. https://doi.org/10.1021/acsami.7b08656.
- [46] S. Mishra, P. Yogi, P.R. Sagdeo, R. Kumar, TiO2–Co3O4 Core—Shell Nanorods: Bifunctional Role in Better Energy Storage and Electrochromism, (2018). https://doi.org/10.1021/acsaem.7b00254.
- [47] P.R. Somani, S. Radhakrishnan, Electrochromic materials and devices: present and future, Materials Chemistry and Physics. 77 (2003) 117–133. https://doi.org/10.1016/S0254-0584(01)00575-2.
- [48] P.M. Beaujuge, J.R. Reynolds, Color Control in π-Conjugated Organic Polymers for Use in Electrochromic Devices, Chem. Rev. 110 (2010) 268–320. https://doi.org/10.1021/cr900129a.
- [49] S. Mishra, H. Pandey, P. Yogi, S.K. Saxena, S. Roy, P.R. Sagdeo, R. Kumar, Interfacial redox centers as origin of color switching in organic electrochromic device, Optical Materials. 66 (2017) 65–71. https://doi.org/10.1016/j.optmat.2017.01.030.
- [50] A. Chaudhary, D.K. Pathak, M. Tanwar, P. Yogi, P.R. Sagdeo, R. Kumar, Polythiophene–PCBM-Based All-Organic Electrochromic Device: Fast and Flexible, ACS Appl. Electron. Mater. 1 (2019) 58–63. https://doi.org/10.1021/acsaelm.8b00012.

- [51] R.J. Mortimer, Electrochromic Materials, Annual Review of Materials Research. 41 (2011) 241–268. https://doi.org/10.1146/annurev-matsci-062910-100344.
- [52] D.R. Rosseinsky, R.J. Mortimer, Electrochromic Systems and the Prospects for Devices, Advanced Materials. 13 (2001) 783–793. https://doi.org/10.1002/1521-4095(200106)13:11<783::AID-ADMA783>3.0.CO;2-D.
- [53] S. Zhang, S. Chen, B. Yan, Y. Gu, Y. Luo, F. Yang, Y. Cao, Solution-Processable and Patternable Poly(o-methoxyaniline)-Based Nanocomposite Film for Large-Area Electrochromic Display with Large Optical Modulation and Ultrafast Response Speed, J. Phys. Chem. C. 124 (2020) 10898–10906. https://doi.org/10.1021/acs.jpcc.0c03079.
- [54] A.L.-S. Eh, A.W.M. Tan, X. Cheng, S. Magdassi, P.S. Lee, Recent Advances in Flexible Electrochromic Devices: Prerequisites, Challenges, and Prospects, Energy Technology. 6 (2018) 33–45. https://doi.org/10.1002/ente.201700705.
- [55] J. Xiong, J. Chen, P.S. Lee, Functional Fibers and Fabrics for Soft Robotics, Wearables, and Human–Robot Interface, Advanced Materials. n/a (n.d.) 2002640. https://doi.org/10.1002/adma.202002640.
- [56] S. Zhang, G. Sun, Y. He, R. Fu, Y. Gu, S. Chen, Preparation, Characterization, and Electrochromic Properties of Nanocellulose-Based Polyaniline Nanocomposite Films, ACS Appl. Mater. Interfaces. 9 (2017) 16426–16434. https://doi.org/10.1021/acsami.7b02794.
- [57] SmartGlass aiming to be top of the class in Qatar, Construction Week Online Middle East. (n.d.). https://www.constructionweekonline.com/article-17012-smartglass-aiming-to-be-top-of-the-class-in-qatar (accessed February 23, 2021).
- [58] S. Mishra, H. Pandey, P. Yogi, S.K. Saxena, S. Roy, P.R. Sagdeo, R. Kumar, Live spectroscopy to observe electrochromism in viologen based solid state device, Solid State Communications. 261 (2017) 17–20. https://doi.org/10.1016/j.ssc.2017.05.020.
- [59] Color, (n.d.). http://depts.washington.edu/cmditr/modules/lum/color.html (accessed February 23, 2021).
- [60] K.J. Patel, G.G. Bhatt, J.R. Ray, P. Suryavanshi, C.J. Panchal, All-inorganic solid-state electrochromic devices: a review, J Solid State Electrochem. 21 (2017) 337–347. https://doi.org/10.1007/s10008-016-3408-z.
- [61] C.G. Granqvist, Handbook of Inorganic Electrochromic Materials, Elsevier, 1995.
- [62] C.G. Granqvist, Electrochromic tungsten oxide films: Review of progress 1993–1998, Solar Energy Materials and Solar Cells. 60 (2000) 201–262. https://doi.org/10.1016/S0927-0248(99)00088-4.
- [63] G.A. Niklasson, L. Berggren, A.-L. Larsson, Electrochromic tungsten oxide: the role of defects, Solar Energy Materials and

- Solar Cells. 84 (2004) 315–328. https://doi.org/10.1016/j.solmat.2004.01.045.
- [64] A. Chaudhary, D.K. Pathak, S. Mishra, P. Yogi, P.R. Sagdeo, R. Kumar, Polythiophene -viologen bilayer for electro-trichromic device, Solar Energy Materials and Solar Cells. 188 (2018) 249–254. https://doi.org/10.1016/j.solmat.2018.08.029.
- [65] J. Zhang, J. Tu, D. Zhang, Y. Qiao, X. Xia, X. Wang, C. Gu, Multicolor electrochromic polyaniline – WO3 hybrid thin films: One-pot molecular assembling synthesis, Journal of Materials Chemistry. 21 (2011) 17316–17324. https://doi.org/10.1039/C1JM13069B.
- [66] A. Chaudhary, D.K. Pathak, S. Kandpal, T. Ghosh, M. Tanwar, R. Kumar, Raw hibiscus extract as redox active biomaterial for novel herbal electrochromic device, Solar Energy Materials and Solar Cells. 215 (2020) 110588. https://doi.org/10.1016/j.solmat.2020.110588.
- [67] V.S. Bagotsky, Fundamentals of Electrochemistry, John Wiley & Sons, 2005.
- [68] N. Elgrishi, K.J. Rountree, B.D. McCarthy, E.S. Rountree, T.T. Eisenhart, J.L. Dempsey, A Practical Beginner's Guide to Cyclic Voltammetry, J. Chem. Educ. 95 (2018) 197–206. https://doi.org/10.1021/acs.jchemed.7b00361.
- [69] Y. Shi, M. Sun, Y. Zhang, J. Cui, X. Shu, Y. Wang, Y. Qin, J. Liu, H.H. Tan, Y. Wu, Rational Design of Oxygen Deficiency-Controlled Tungsten Oxide Electrochromic Films with an Exceptional Memory Effect, ACS Appl. Mater. Interfaces. 12 (2020) 32658–32665. https://doi.org/10.1021/acsami.0c06786.
- [70] C.J. Schoot, J.J. Ponjee, H.T. van Dam, R.A. van Doorn, P.T. Bolwijn, New electrochromic memory display, Appl. Phys. Lett. 23 (1973) 64–65. https://doi.org/10.1063/1.1654808.
- [71] T.Y. Yun, X. Li, S.H. Kim, H.C. Moon, Dual-Function Electrochromic Supercapacitors Displaying Real-Time Capacity in Color, ACS Appl. Mater. Interfaces. 10 (2018) 43993–43999. https://doi.org/10.1021/acsami.8b15066.
- [72] S. Mishra, P. Yogi, P.R. Sagdeo, R. Kumar, Mesoporous Nickel Oxide (NiO) Nanopetals for Ultrasensitive Glucose Sensing, Nanoscale Research Letters. 13 (2018) 16. https://doi.org/10.1186/s11671-018-2435-3.
- [73] A. Chaudhary, D. K. Pathak, M. Tanwar, J. Koch, H. Pfnür, R. Kumar, Polythiophene-nanoWO 3 bilayer as an electrochromic infrared filter: a transparent heat shield, Journal of Materials Chemistry C. 8 (2020) 1773–1780. https://doi.org/10.1039/C9TC05523A.
- [74] Y.R. In, Y.M. Kim, Y. Lee, W.Y. Choi, S.H. Kim, S.W. Lee, H.C. Moon, Ultra-Low Power Electrochromic Heat Shutters Through Tailoring Diffusion-Controlled Behaviors, ACS Appl. Mater. Interfaces. 12 (2020) 30635–30642. https://doi.org/10.1021/acsami.0c05918.

- [75] W.A. de Heer, A. Châtelain, D. Ugarte, A Carbon Nanotube Field-Emission Electron Source, Science. 270 (1995) 1179–1180. https://doi.org/10.1126/science.270.5239.1179.
- [76] A. Pandey, A. Prasad, J.P. Moscatello, Y.K. Yap, Stable Electron Field Emission from PMMA-CNT Matrices, ACS Nano. 4 (2010) 6760–6766. https://doi.org/10.1021/nn100925g.
- [77] A. Pandey, A. Prasad, J.P. Moscatello, M. Engelhard, C. Wang, Y.K. Yap, Very Stable Electron Field Emission from Strontium Titanate Coated Carbon Nanotube Matrices with Low Emission Thresholds, ACS Nano. 7 (2013) 117–125. https://doi.org/10.1021/nn303351g.
- [78] M. Sreekanth, P. Srivastava, S. Ghosh, Highly enhanced field emission from copper oxide nanoparticle decorated vertically aligned carbon nanotubes: Role of interfacial electronic structure, Applied Surface Science. 508 (2020) 145215. https://doi.org/10.1016/j.apsusc.2019.145215.
- [79] A. Tewari, P. Srivastava, S. Ghosh, Modeling of the in-situ nitrogen (N) doping of graphene-carbon nanotube (CNT) hybrids in a plasma medium and their field emission properties, Physics of Plasmas. 25 (2018) 083520. https://doi.org/10.1063/1.5048053.
- [80] M. Sreekanth, S. Ghosh, S.R. Barman, P. Sadhukhan, P. Srivastava, Field emission properties of indium-decorated vertically aligned carbon nanotubes: an interplay between type of hybridization, density of states and metal thickness, Appl. Phys. A. 124 (2018) 528. https://doi.org/10.1007/s00339-018-1954-1.
- [81] M. Sreekanth, S. Ghosh, P. Biswas, S. Kumar, P. Srivastava, Improved field emission from indium decorated multi-walled carbon nanotubes, Applied Surface Science. 383 (2016) 84–89. https://doi.org/10.1016/j.apsusc.2016.04.170.
- [82] D. Sarker, S. Bhattacharya, R.D. Rodriguez, E. Sheremet, D. Kabiraj, D.K. Avasthi, D.R.T. Zahn, H. Schmidt, P. Srivastava, S. Ghosh, Unraveling The Origin of Enhanced Field Emission from Irradiated FeCo-SiO2 Nanocomposites: A Combined Experimental and First-Principles Based Study, ACS Appl. Mater. Interfaces. 8 (2016) 4994–5001. https://doi.org/10.1021/acsami.5b07937.
- [83] M. Sreekanth, S. Ghosh, R. Patra, P. Srivastava, Highly enhanced and temporally stable field emission from MWCNTs grown on aluminum coated silicon substrate, AIP Advances. 5 (2015) 067173. https://doi.org/10.1063/1.4923423.
- [84] G. Ali, M. Maqbool, Field emission properties of TiO2 nanotubes fabricated on Ti wire, Materials Chemistry and Physics. 233 (2019) 21–26. https://doi.org/10.1016/j.matchemphys.2019.05.026.
- [85] J. Liang, G. Zhang, TiO2 Nanotip Arrays: Anodic Fabrication and Field-Emission Properties, ACS Appl. Mater. Interfaces. 4 (2012) 6053–6061. https://doi.org/10.1021/am301690f.
- [86] Q. Zhao, H.Z. Zhang, Y.W. Zhu, S.Q. Feng, X.C. Sun, J. Xu, D.P. Yu, Morphological effects on the field emission of ZnO nanorod arrays, Appl. Phys. Lett. 86 (2005) 203115. https://doi.org/10.1063/1.1931831.

- [87] X.-G. Zhang, S.T. Pantelides, Screening in Nanowires and Nanocontacts: Field Emission, Adhesion Force, and Contact Resistance, Nano Lett. 9 (2009) 4306–4310. https://doi.org/10.1021/nl902533n.
- [88] J.P. Barbour, W.W. Dolan, J.K. Trolan, E.E. Martin, W.P. Dyke, Space-Charge Effects in Field Emission, Phys. Rev. 92 (1953) 45–51. https://doi.org/10.1103/PhysRev.92.45.
- [89] R.W. Strayer, W. Mackie, L.W. Swanson, Work function measurements by the field emission retarding potential method, Surface Science. 34 (1973) 225–248. https://doi.org/10.1016/0039-6028(73)90117-9.
- [90] R.H. Fowler, L. Nordheim, Electron emission in intense electric fields, Proc. R. Soc. Lond. A. 119 (1928) 173–181. https://doi.org/10.1098/rspa.1928.0091.
- [91] S.E. Létant, T.W. van Buuren, L.J. Terminello, Nanochannel Arrays on Silicon Platforms by Electrochemistry, Nano Lett. 4 (2004) 1705–1707. https://doi.org/10.1021/nl049111c.
- [92] D. Dimova-Malinovska, M. Sendova-Vassileva, N. Tzenov, M. Kamenova, Preparation of thin porous silicon layers by stain etching, Thin Solid Films. 297 (1997) 9–12. https://doi.org/10.1016/S0040-6090(96)09434-5.
- [93] B. González-Díaz, R. Guerrero-Lemus, N. Marrero, C. Hernández-Rodríguez, F.A. Ben-Hander, J.M. Martínez-Duart, Anisotropic textured silicon obtained by stain-etching at low etching rates, J. Phys. D: Appl. Phys. 39 (2006) 631–634. https://doi.org/10.1088/0022-3727/39/4/006.
- [94] H. Föll, M. Christophersen, J. Carstensen, G. Hasse, Formation and application of porous silicon, Materials Science and Engineering: R: Reports. 39 (2002) 93–141. https://doi.org/10.1016/S0927-796X(02)00090-6.
- [95] H.S. Mavi, S. Prusty, M. Kumar, R. Kumar, A.K. Shukla, S. Rath, Formation of Si and Ge quantum structures by laser-induced etching, Physica Status Solidi (a). 203 (2006) 2444–2450. https://doi.org/10.1002/pssa.200521027.
- [96] Y. KENEMITSU, Light emission from novel silicon materials, J.Phys.Soc.of Japan. 63 (1994). https://ci.nii.ac.jp/naid/10004650854/ (accessed February 24, 2021).
- [97] A. Meldrum, R.F. Haglund Jr, L.A. Boatner, C.W. White, Nanocomposite Materials Formed by Ion Implantation, Advanced Materials. 13 (2001) 1431–1444. https://doi.org/10.1002/1521-4095(200110)13:19<1431::AID-ADMA1431>3.0.CO;2-Z.
- [98] G. Fang, Y. Cheng, L. Ai, C. Li, J. He, C. Wang, H. Huang, L. Yuan, X. Zhao, Fabrication and electrical and photosensitive properties of silicon nanowire p—n homojunctions, Physica Status Solidi (a). 205 (2008) 2722–2728. https://doi.org/10.1002/pssa.200723266.
- [99] M. Tamura, Damage formation and annealing of ion implantation in Si, Materials Science Reports. 6 (1991) 141–214. https://doi.org/10.1016/0920-2307(91)90007-A.

- [100] Z. Huang, T. Shimizu, S. Senz, Z. Zhang, N. Geyer, U. Gösele, Oxidation Rate Effect on the Direction of Metal-Assisted Chemical and Electrochemical Etching of Silicon, J. Phys. Chem. C. 114 (2010) 10683–10690. https://doi.org/10.1021/jp911121q.
- [101] hydrothermal synthesis, (n.d.). https://eng.thesaurus.rusnano.com/wiki/article729 (accessed February 24, 2021).
- [102] K. Byrappa, T. Adschiri, Hydrothermal technology for nanotechnology, Progress in Crystal Growth and Characterization of Materials. 53 (2007) 117–166. https://doi.org/10.1016/j.pcrysgrow.2007.04.001.
- [103] D.K. Pathak, A. Chaudhary, S. Mishra, P. Yogi, S.K. Saxena, P.R. Sagdeo, R. Kumar, Precursor concentration dependent hydrothermal NiO nanopetals: Tuning morphology for efficient applications, Superlattices and Microstructures. 125 (2019) 138–143. https://doi.org/10.1016/j.spmi.2018.11.001.
- [104] D.K. Pathak, A. Chaudhary, S. Mishra, P. Yogi, P.R. Sagdeo, R. Kumar, Improved field emission from appropriately packed TiO2 nanorods: Designing the miniaturization, Superlattices and Microstructures. 126 (2019) 1–7. https://doi.org/10.1016/j.spmi.2018.12.003.
- [105] W. Ruythooren, K. Attenborough, S. Beerten, P. Merken, J. Fransaer, E. Beyne, C.V. Hoof, J.D. Boeck, J.P. Celis, Electrodeposition for the synthesis of microsystems, J. Micromech. Microeng. 10 (2000) 101–107. https://doi.org/10.1088/0960-1317/10/2/301.
- [106] D.K. Pathak, A. Chaudhary, M. Tanwar, U.K. Goutam, H. Pfnür, R. Kumar, Chronopotentiometric Deposition of Nanocobalt Oxide for Electrochromic Auxiliary Active Electrode Application, Physica Status Solidi (a). 217 (2020) 2000173. https://doi.org/10.1002/pssa.202000173.
- [107] D.K. Pathak, A. Chaudhary, M. Tanwar, U.K. Goutam, R. Kumar, Nano-cobalt oxide/viologen hybrid solid state device: Electrochromism beyond chemical cell, Appl. Phys. Lett. 116 (2020) 141901. https://doi.org/10.1063/1.5145079.
- [108] A. Chaudhary, D.K. Pathak, T. Ghosh, S. Kandpal, M. Tanwar, C. Rani, R. Kumar, Prussian Blue-Cobalt Oxide Double Layer for Efficient All-Inorganic Multicolor Electrochromic Device, ACS Appl. Electron. Mater. 2 (2020) 1768–1773. https://doi.org/10.1021/acsaelm.0c00342.
- [109] Spin Coating an overview | ScienceDirect Topics, (n.d.). https://www.sciencedirect.com/topics/chemistry/spin-coating (accessed February 24, 2021).
- [110] Discover the new ZEISS GeminiSEM Family, (n.d.). https://www.zeiss.com/microscopy/int/cmp/mat/21/geminisem/gem inisem-family.html (accessed February 24, 2021).
- [111] FEI Tecnai G2 20 TWIN Transmission Electron Microscope | www.bionand.es, (n.d.). http://www.bionand.es/equipment/feitecnai-tem (accessed February 24, 2021).

- [112] Park NX10 Overview | Park Atomic Force Microscope, (n.d.). https://www.parksystems.com/index.php/products/small-sample-afm/park-nx10/overview?gclid=Cj0KCQiA7NKBBhDBARIsAHbXCB6aLN 0UjLqgUfh-5SYpzCDNx3wnlBP81L3IlbFBzIFh2dgAPoyCI4YaAsokEALw\_wcB (accessed February 24, 2021).
- [113] SmartLab® Automated Multipurpose XRD with Guidance Software, AZoM.Com. (n.d.). https://www.azom.com/equipment-details.aspx?EquipID=5989 (accessed February 24, 2021).
- [114] Detail, (n.d.). https://www.horiba.com/en\_en/products/detail/action/show/Product /labram-hr-evolution-1083/ (accessed February 24, 2021).
- [115] LAMBDA 365 UV/Vis Spectrophotometer-N4100020|PerkinElmer, (n.d.). https://www.perkinelmer.com/product/lambda-365-spectrophotometer-uv-express-n4100020 (accessed February 24, 2021).
- [116] UV-Vis Spectrophotometer, Routine UV-Vis, Cary 60 | Agilent, (n.d.). https://www.agilent.com/en/product/molecular-spectroscopy/uv-vis-uv-vis-nir-spectroscopy/uv-vis-uv-vis-nir-systems/cary-60-uv-vis-spectrophotometer (accessed February 24, 2021).
- [117] SMU Source Measurement Unit, (n.d.).
  https://www.tektronixindia.com/source-measurementunit/?\_bt=495464254251&\_bk=%2B2450%20%2Bsmu&\_bm=b&
  \_bn=g&\_bg=112358064930&gclid=Cj0KCQiA7NKBBhDBARIs
  AHbXCB4sGfSgeZOkL\_hYTHCYMPpQ9qXaZIUjBLUxTwVGF
  NEjfbVmOu4ttlwaAsMrEALw\_wcB (accessed February 24, 2021).
- [118] D.K. Pathak, A. Chaudhary, M. Tanwar, U.K. Goutam, P. Mondal, R. Kumar, Nickel Cobalt Oxide Nanoneedles for Electrochromic Glucose Sensors, ACS Appl. Nano Mater. (2021). https://doi.org/10.1021/acsanm.0c03451.
- [119] S. Darmawi, S. Burkhardt, T. Leichtweiss, D. A. Weber, S. Wenzel, J. Janek, M. T. Elm, P. J. Klar, Correlation of electrochromic properties and oxidation states in nanocrystalline tungsten trioxide, Physical Chemistry Chemical Physics. 17 (2015) 15903–15911. https://doi.org/10.1039/C5CP02482J.
- [120] G. Canzi, J.C. Goeltz, J.S. Henderson, R.E. Park, C. Maruggi, C.P. Kubiak, On the Observation of Intervalence Charge Transfer Bands in Hydrogen-Bonded Mixed-Valence Complexes, J. Am. Chem. Soc. 136 (2014) 1710–1713. https://doi.org/10.1021/ja410540m.
- [121] H. Feil, Intervalence charge transfer transitions in superconductors and related compounds, Solid State Communications. 69 (1989) 245–248. https://doi.org/10.1016/0038-1098(89)90843-0.
- [122] orbitals Why do rare earth metal oxides vary in color so much?, Chemistry Stack Exchange. (n.d.).

- https://chemistry.stackexchange.com/questions/66745/why-do-rare-earth-metal-oxides-vary-in-color-so-much (accessed February 24, 2021).
- [123] J. Peng, H.-H. Jeong, Q. Lin, S. Cormier, H.-L. Liang, M.F.L.D. Volder, S. Vignolini, J.J. Baumberg, Scalable electrochromic nanopixels using plasmonics, Science Advances. 5 (2019) eaaw2205. https://doi.org/10.1126/sciadv.aaw2205.
- [124] M. Qiu, F. Zhou, P. Sun, X. Chen, C. Zhao, W. Mai, Unveiling the electrochromic mechanism of Prussian Blue by electronic transition analysis, Nano Energy. 78 (2020) 105148. https://doi.org/10.1016/j.nanoen.2020.105148.
- [125] P. Salles, D. Pinto, K. Hantanasirisakul, K. Maleski, C.E. Shuck, Y. Gogotsi, Electrochromic Effect in Titanium Carbide MXene Thin Films Produced by Dip-Coating, Advanced Functional Materials. 29 (2019) 1809223. https://doi.org/10.1002/adfm.201809223.
- [126] R.J. Mortimer, Organic electrochromic materials, Electrochimica Acta. 44 (1999) 2971–2981. https://doi.org/10.1016/S0013-4686(99)00046-8.
- [127] K.-C. Cheng, F.-R. Chen, J.-J. Kai, V2O5 nanowires as a functional material for electrochromic device, Solar Energy Materials and Solar Cells. 90 (2006) 1156–1165. https://doi.org/10.1016/j.solmat.2005.07.006.
- [128] P.A. Sheena, H. Hitha, A. Sreedevi, T. Varghese, Influence of finite size and surface effects on the structural, electrical and magnetic properties of nanostructured nickel oxide, J Mater Sci: Mater Electron. 31 (2020) 5769–5778. https://doi.org/10.1007/s10854-020-03147-7.
- [129] R.E. Dietz, G.I. Parisot, A.E. Meixner, Infrared Absorption and Raman Scattering by Two-Magnon Processes in NiO, Phys. Rev. B. 4 (1971) 2302–2310. https://doi.org/10.1103/PhysRevB.4.2302.
- [130] G.A. Sawatzky, J.W. Allen, Magnitude and Origin of the Band Gap in NiO, Phys. Rev. Lett. 53 (1984) 2339–2342. https://doi.org/10.1103/PhysRevLett.53.2339.
- [131] E. Şilik, S. Pat, S. Özen, R. Mohammadigharehbagh, H.H. Yudar, C. Musaoğlu, Ş. Korkmaz, Electrochromic properties of TiO2 thin films grown by thermionic vacuum arc method, Thin Solid Films. 640 (2017) 27–32. https://doi.org/10.1016/j.tsf.2017.07.073.
- [132] M.N. Tahir, P. Theato, P. Oberle, G. Melnyk, S. Faiss, U. Kolb, A. Janshoff, M. Stepputat, W. Tremel, Facile Synthesis and Characterization of Functionalized, Monocrystalline Rutile TiO2 Nanorods, Langmuir. 22 (2006) 5209–5212. https://doi.org/10.1021/la052664y.
- [133] Q. Huang, L. Gao, A Simple Route for the Synthesis of Rutile TiO2 Nanorods, Chem. Lett. 32 (2003) 638–639. https://doi.org/10.1246/cl.2003.638.
- [134] V. Mishra, M.K. Warshi, A. Sati, A. Kumar, V. Mishra, A. Sagdeo, R. Kumar, P.R. Sagdeo, Diffuse reflectance spectroscopy: An effective tool to probe the defect states in wide band gap

- semiconducting materials, Materials Science in Semiconductor Processing. 86 (2018) 151–156. https://doi.org/10.1016/j.mssp.2018.06.025.
- [135] P. Yogi, D. Poonia, S. Mishra, S.K. Saxena, S. Roy, V. Kumar, P.R. Sagdeo, R. Kumar, Spectral Anomaly in Raman Scattering from p-Type Silicon Nanowires, J. Phys. Chem. C. 121 (2017) 5372–5378. https://doi.org/10.1021/acs.jpcc.6b12811.
- [136] P. Yogi, M. Tanwar, S.K. Saxena, S. Mishra, D.K. Pathak, A. Chaudhary, P.R. Sagdeo, R. Kumar, Quantifying the Short-Range Order in Amorphous Silicon by Raman Scattering, Anal. Chem. 90 (2018) 8123–8129. https://doi.org/10.1021/acs.analchem.8b01352.
- [137] S.-J. Bao, C.M. Li, J.-F. Zang, X.-Q. Cui, Y. Qiao, J. Guo, New Nanostructured TiO2 for Direct Electrochemistry and Glucose Sensor Applications, Advanced Functional Materials. 18 (2008) 591–599. https://doi.org/10.1002/adfm.200700728.
- [138] C.N. Polo da Fonseca, M.-A. De Paoli, A. Gorenstein, Electrochromism in cobalt oxide thin films grown by anodic electroprecipitation, Solar Energy Materials and Solar Cells. 33 (1994) 73–81. https://doi.org/10.1016/0927-0248(94)90291-7.
- [139] M. Manickam, V. Ponnuswamy, C. Sankar, R. Suresh, R. Mariappan, J. Chandrasekaran, The Effect of Solution pH on the Properties of Cobalt Oxide Thin Films Prepared by Nebulizer Spray Pyrolysis Technique, Int. J. Thin Fil. Sci. Tec. 5 (2016) 155–161. https://doi.org/10.18576/ijtfst/050302.
- [140] V.G. Hadjiev, M.N. Iliev, I.V. Vergilov, The Raman spectra of Co3O4, J. Phys. C: Solid State Phys. 21 (1988) L199–L201. https://doi.org/10.1088/0022-3719/21/7/007.
- [141] L. Armelao, D. Barreca, S. Gross, E. Tondello, Sol-Gel and CVD Co3O4 Thin Films Characterized by XPS, Surface Science Spectra. 8 (2001) 14. https://doi.org/10.1116/11.20010601.
- [142] A. Younis, D. Chu, X. Lin, J. Lee, S. Li, Bipolar resistive switching in p-type Co3O4 nanosheets prepared by electrochemical deposition, Nanoscale Res Lett. 8 (2013) 36. https://doi.org/10.1186/1556-276X-8-36.
- [143] A. Chaudhary, D.K. Pathak, M. Tanwar, P.R. Sagdeo, R. Kumar, Prussian Blue-Viologen Inorganic—Organic Hybrid Blend for Improved Electrochromic Performance, ACS Appl. Electron. Mater. 1 (2019) 892–899. https://doi.org/10.1021/acsaelm.9b00089.
- [144] D.M. DeLongchamp, P.T. Hammond, High-Contrast Electrochromism and Controllable Dissolution of Assembled Prussian Blue/Polymer Nanocomposites, Advanced Functional Materials. 14 (2004) 224–232. https://doi.org/10.1002/adfm.200304507.
- [145] G. Moretti, C. Gervais, Raman spectroscopy of the photosensitive pigment Prussian blue, Journal of Raman Spectroscopy. 49 (2018) 1198–1204. https://doi.org/10.1002/jrs.5366.
- [146] J. Wang, L. Zhang, L. Yu, Z. Jiao, H. Xie, X.W. (David) Lou, X.W. Sun, A bi-functional device for self-powered electrochromic

- window and self-rechargeable transparent battery applications, Nat Commun. 5 (2014) 1–7. https://doi.org/10.1038/ncomms5921.
- [147] X. Yu, T.J. Marks, A. Facchetti, Metal oxides for optoelectronic applications, Nature Materials. 15 (2016) 383–396. https://doi.org/10.1038/nmat4599.
- [148] M.M. Rahman, A.J.S. Ahammad, J.-H. Jin, S.J. Ahn, J.-J. Lee, A Comprehensive Review of Glucose Biosensors Based on Nanostructured Metal-Oxides, Sensors. 10 (2010) 4855–4886. https://doi.org/10.3390/s100504855.
- [149] G.H.A. Therese, P.V. Kamath, Electrochemical Synthesis of Metal Oxides and Hydroxides, Chem. Mater. 12 (2000) 1195–1204. https://doi.org/10.1021/cm990447a.
- [150] M.V. Reddy, G.V. Subba Rao, B.V.R. Chowdari, Metal Oxides and Oxysalts as Anode Materials for Li Ion Batteries, Chem. Rev. 113 (2013) 5364–5457. https://doi.org/10.1021/cr3001884.
- [151] A. Vilan, D. Cahen, Chemical Modification of Semiconductor Surfaces for Molecular Electronics, Chem. Rev. 117 (2017) 4624–4666. https://doi.org/10.1021/acs.chemrev.6b00746.
- [152] J. Du, G. Zhou, H. Zhang, C. Cheng, J. Ma, W. Wei, L. Chen, T. Wang, Ultrathin Porous NiCo2O4 Nanosheet Arrays on Flexible Carbon Fabric for High-Performance Supercapacitors, ACS Appl. Mater. Interfaces. 5 (2013) 7405–7409. https://doi.org/10.1021/am4017335.
- [153] S. Jain, S. Mishra, T.K. Sarma, Zn2+ Induced Self-Assembled Growth of Octapodal CuxO–ZnO Microcrystals: Multifunctional Applications in Reductive Degradation of Organic Pollutants and Nonenzymatic Electrochemical Sensing of Glucose, ACS Sustainable Chem. Eng. 6 (2018) 9771–9783. https://doi.org/10.1021/acssuschemeng.8b00838.
- [154] B.A. Nail, J.M. Fields, J. Zhao, J. Wang, M.J. Greaney, R.L. Brutchey, F.E. Osterloh, Nickel oxide particles catalyze photochemical hydrogen evolution from water--nanoscaling promotes p-type character and minority carrier extraction, ACS Nano. 9 (2015) 5135–5142. https://doi.org/10.1021/acsnano.5b00435.
- [155] S.M.N. Jeghan, G. Lee, One-dimensional hierarchical nanostructures of NiCo2O4, NiCo2S4 and NiCo2Se4 with superior electrocatalytic activities toward efficient oxygen evolution reaction, Nanotechnology. 31 (2020) 295405. https://doi.org/10.1088/1361-6528/ab8667.
- [156] A. Chaudhary, D.K. Pathak, M. Tanwar, P.R. Sagdeo, R. Kumar, Prussian Blue-Viologen Inorganic—Organic Hybrid Blend for Improved Electrochromic Performance, ACS Appl. Electron. Mater. 1 (2019) 892–899. https://doi.org/10.1021/acsaelm.9b00089.
- [157] D.A. Wruck, M. Rubin, Structure and Electronic Properties of Electrochromic NiO Films, J. Electrochem. Soc. 140 (1993) 1097–1104. https://doi.org/10.1149/1.2056205.
- [158] P. Poizot, S. Laruelle, S. Grugeon, L. Dupont, J.-M. Tarascon, Nano-sized transition-metal oxides as negative-electrode materials

- for lithium-ion batteries, Nature. 407 (2000) 496–499. https://doi.org/10.1038/35035045.
- [159] M.U. Anu Prathap, R. Srivastava, Synthesis of NiCo2O4 and its application in the electrocatalytic oxidation of methanol, Nano Energy. 2 (2013) 1046–1053. https://doi.org/10.1016/j.nanoen.2013.04.003.
- [160] A. Ahlawat, V.G. Sathe, Raman study of NiFe2O4 nanoparticles, bulk and films: effect of laser power, Journal of Raman Spectroscopy. 42 (2011) 1087–1094. https://doi.org/10.1002/jrs.2791.
- [161] T. Yu, Z.X. Shen, Y. Shi, J. Ding, Cation migration and magnetic ordering in spinel CoFe2O4powder: micro-Raman scattering study, J. Phys.: Condens. Matter. 14 (2002) L613–L618. https://doi.org/10.1088/0953-8984/14/37/101.
- [162] Y. Ding, Y. Wang, L. Su, M. Bellagamba, H. Zhang, Y. Lei, Electrospun Co3O4 nanofibers for sensitive and selective glucose detection, Biosensors and Bioelectronics. 26 (2010) 542–548. https://doi.org/10.1016/j.bios.2010.07.050.
- [163] O.N. Shebanova, P. Lazor, Raman study of magnetite (Fe3O4): laser-induced thermal effects and oxidation, Journal of Raman Spectroscopy. 34 (2003) 845–852. https://doi.org/10.1002/jrs.1056.
- [164] H. Karimi-Maleh, O.A. Arotiba, Simultaneous determination of cholesterol, ascorbic acid and uric acid as three essential biological compounds at a carbon paste electrode modified with copper oxide decorated reduced graphene oxide nanocomposite and ionic liquid, Journal of Colloid and Interface Science. 560 (2020) 208–212. https://doi.org/10.1016/j.jcis.2019.10.007.
- [165] H. Karimi-Maleh, F. Karimi, Y. Orooji, G. Mansouri, A. Razmjou, A. Aygun, F. Sen, A new nickel-based co-crystal complex electrocatalyst amplified by NiO dope Pt nanostructure hybrid; a highly sensitive approach for determination of cysteamine in the presence of serotonin, Scientific Reports. 10 (2020) 11699. https://doi.org/10.1038/s41598-020-68663-2.
- [166] J.F. Marco, J.R. Gancedo, M. Gracia, J.L. Gautier, E. Ríos, F.J. Berry, Characterization of the Nickel Cobaltite, NiCo2O4, Prepared by Several Methods: An XRD, XANES, EXAFS, and XPS Study, Journal of Solid State Chemistry. 153 (2000) 74–81. https://doi.org/10.1006/jssc.2000.8749.
- [167] S. Khalid, C. Cao, L. Wang, Y. Zhu, Microwave Assisted Synthesis of Porous NiCo 2 O 4 Microspheres: Application as High Performance Asymmetric and Symmetric Supercapacitors with Large Areal Capacitance, Scientific Reports. 6 (2016) 22699. https://doi.org/10.1038/srep22699.
- [168] M.N. Iliev, P. Silwal, B. Loukya, R. Datta, D.H. Kim, N.D. Todorov, N. Pachauri, A. Gupta, Raman studies of cation distribution and thermal stability of epitaxial spinel NiCo2O4 films, Journal of Applied Physics. 114 (2013) 033514. https://doi.org/10.1063/1.4815874.
- [169] M. Tanwar, A. Chaudhary, D.K. Pathak, P. Yogi, S.K. Saxena, P.R. Sagdeo, R. Kumar, Deconvoluting Diffuse Reflectance

- Spectra for Retrieving Nanostructures' Size Details: An Easy and Efficient Approach, J. Phys. Chem. A. 123 (2019) 3607–3614. https://doi.org/10.1021/acs.jpca.9b01935.
- [170] E. Umeshbabu, G. Rajeshkhanna, P. Justin, G.R. Rao, Magnetic, optical and electrocatalytic properties of urchin and sheaf-like NiCo2O4 nanostructures, Materials Chemistry and Physics. 165 (2015) 235–244. https://doi.org/10.1016/j.matchemphys.2015.09.023.
- [171] P. Sinha, A. Datar, C. Jeong, X. Deng, Y.G. Chung, L.-C. Lin, Surface Area Determination of Porous Materials Using the Brunauer–Emmett–Teller (BET) Method: Limitations and Improvements, J. Phys. Chem. C. 123 (2019) 20195–20209. https://doi.org/10.1021/acs.jpcc.9b02116.
- [172] G.T. Tyuliev, K.L. Kostov, XPS/HREELS study of NiO films grown on Ni(111), Phys. Rev. B. 60 (1999) 2900–2907. https://doi.org/10.1103/PhysRevB.60.2900.
- [173] Ya.M. Kolotyrkin, I.D. Belova, Yu.E. Roginskaya, V.B. Kozhevnikov, D.S. Zakhar'in, Yu.N. Venevtsev, High-spin configuration of Co(III) in nonstoichiometric Co3O4 films. XPS investigations, Materials Chemistry and Physics. 11 (1984) 29–48. https://doi.org/10.1016/0254-0584(84)90086-5.
- [174] K.D. Gilroy, A. Ruditskiy, H.-C. Peng, D. Qin, Y. Xia, Bimetallic Nanocrystals: Syntheses, Properties, and Applications, Chem. Rev. 116 (2016) 10414–10472. https://doi.org/10.1021/acs.chemrev.6b00211.
- [175] S. Cao, F. (Feng) Tao, Y. Tang, Y. Li, J. Yu, Size- and shape-dependent catalytic performances of oxidation and reduction reactions on nanocatalysts, Chem. Soc. Rev. 45 (2016) 4747–4765. https://doi.org/10.1039/C6CS00094K.
- [176] Y. Xia, Y. Xiong, B. Lim, S.E. Skrabalak, Shape-controlled synthesis of metal nanocrystals: simple chemistry meets complex physics?, Angew Chem Int Ed Engl. 48 (2009) 60–103. https://doi.org/10.1002/anie.200802248.
- [177] H. Karimi-Maleh, F. Karimi, S. Malekmohammadi, N. Zakariae, R. Esmaeili, S. Rostamnia, M.L. Yola, N. Atar, S. Movaghgharnezhad, S. Rajendran, A. Razmjou, Y. Orooji, S. Agarwal, V.K. Gupta, An amplified voltammetric sensor based on platinum nanoparticle/polyoxometalate/two-dimensional hexagonal boron nitride nanosheets composite and ionic liquid for determination of N-hydroxysuccinimide in water samples, Journal of Molecular Liquids. 310 (2020) 113185. https://doi.org/10.1016/j.molliq.2020.113185.
- [178] T.Y. Wong, C.M.G. Cheung, M. Larsen, S. Sharma, R. Simó, Diabetic retinopathy, Nat Rev Dis Primers. 2 (2016) 16012. https://doi.org/10.1038/nrdp.2016.12.
- [179] Diabetic kidney disease, Nature Reviews Disease Primers. 1 (2015) 1–1. https://doi.org/10.1038/nrdp.2015.38.
- [180] H. Teymourian, A. Barfidokht, J. Wang, Electrochemical glucose sensors in diabetes management: an updated review (2010–2020),

- Chem. Soc. Rev. 49 (2020) 7671–7709. https://doi.org/10.1039/D0CS00304B.
- [181] A. Heller, B. Feldman, Electrochemical Glucose Sensors and Their Applications in Diabetes Management, Chem. Rev. 108 (2008) 2482–2505. https://doi.org/10.1021/cr068069y.
- [182] US6743635B2 System and methods for blood glucose sensing Google Patents, (n.d.). https://patents.google.com/patent/US6743635B2/en (accessed August 7, 2019).
- [183] J. Wang, L. Xu, Y. Lu, K. Sheng, W. Liu, C. Chen, Y. Li, B. Dong, H. Song, Engineered IrO2@NiO Core–Shell Nanowires for Sensitive Non-enzymatic Detection of Trace Glucose in Saliva, Anal. Chem. 88 (2016) 12346–12353. https://doi.org/10.1021/acs.analchem.6b03558.
- [184] M. Saraf, K. Natarajan, S.M. Mobin, Non-enzymatic amperometric sensing of glucose by employing sucrose templated microspheres of copper oxide (CuO), Dalton Trans. 45 (2016) 5833–5840. https://doi.org/10.1039/C6DT00670A.
- [185] B.-A. Mei, O. Munteshari, J. Lau, B. Dunn, L. Pilon, Physical Interpretations of Nyquist Plots for EDLC Electrodes and Devices, J. Phys. Chem. C. 122 (2018) 194–206. https://doi.org/10.1021/acs.jpcc.7b10582.
- [186] T. Zhai, X. Fang, Y. Bando, Q. Liao, X. Xu, H. Zeng, Y. Ma, J. Yao, D. Golberg, Morphology-Dependent Stimulated Emission and Field Emission of Ordered CdS Nanostructure Arrays, ACS Nano. 3 (2009) 949–959. https://doi.org/10.1021/nn800895k.
- [187] V.V. Zhirnov, G.J. Wojak, W.B. Choi, J.J. Cuomo, J.J. Hren, Wide band gap materials for field emission devices, Journal of Vacuum Science & Technology A. 15 (1997) 1733–1738. https://doi.org/10.1116/1.580929.
- [188] J.W. Gadzuk, E.W. Plummer, Field Emission Energy Distribution (FEED), Rev. Mod. Phys. 45 (1973) 487–548. https://doi.org/10.1103/RevModPhys.45.487.
- [189] F.A. Padovani, R. Stratton, Field and thermionic-field emission in Schottky barriers, Solid-State Electronics. 9 (1966) 695–707. https://doi.org/10.1016/0038-1101(66)90097-9.
- [190] C.A. Spindt, A Thin-Film Field-Emission Cathode, Journal of Applied Physics. 39 (1968) 3504–3505. https://doi.org/10.1063/1.1656810.
- [191] Y.W. Zhu, H.Z. Zhang, X.C. Sun, S.Q. Feng, J. Xu, Q. Zhao, B. Xiang, R.M. Wang, D.P. Yu, Efficient field emission from ZnO nanoneedle arrays, Appl. Phys. Lett. 83 (2003) 144–146. https://doi.org/10.1063/1.1589166.
- [192] C.X. Xu, X.W. Sun, Field emission from zinc oxide nanopins, Appl. Phys. Lett. 83 (2003) 3806–3808. https://doi.org/10.1063/1.1625774.
- [193] M. Grifoni, P. Hänggi, Driven quantum tunneling, Physics Reports. 304 (1998) 229–354. https://doi.org/10.1016/S0370-1573(98)00022-2.

- [194] W.B. Choi, D.S. Chung, J.H. Kang, H.Y. Kim, Y.W. Jin, I.T. Han, Y.H. Lee, J.E. Jung, N.S. Lee, G.S. Park, J.M. Kim, Fully sealed, high-brightness carbon-nanotube field-emission display, Appl. Phys. Lett. 75 (1999) 3129–3131. https://doi.org/10.1063/1.125253.
- [195] Q.H. Wang, A.A. Setlur, J.M. Lauerhaas, J.Y. Dai, E.W. Seelig, R.P.H. Chang, A nanotube-based field-emission flat panel display, Appl. Phys. Lett. 72 (1998) 2912–2913. https://doi.org/10.1063/1.121493.
- [196] W.B. Choi, Y.W. Jin, H.Y. Kim, S.J. Lee, M.J. Yun, J.H. Kang, Y.S. Choi, N.S. Park, N.S. Lee, J.M. Kim, Electrophoresis deposition of carbon nanotubes for triode-type field emission display, Appl. Phys. Lett. 78 (2001) 1547–1549. https://doi.org/10.1063/1.1349870.
- [197] J. Robertson, Amorphous carbon cathodes for field emission display, Thin Solid Films. 296 (1997) 61–65. https://doi.org/10.1016/S0040-6090(96)09381-9.
- [198] P. Liu, Y. Wei, K. Liu, L. Liu, K. Jiang, S. Fan, New-Type Planar Field Emission Display with Superaligned Carbon Nanotube Yarn Emitter, Nano Lett. 12 (2012) 2391–2396. https://doi.org/10.1021/nl3003792.
- [199] N. Shimoi, S. Tanaka, Numerical Analysis of Electron Emission Site Distribution of Carbon Nanofibers for Field Emission Properties, ACS Appl. Mater. Interfaces. 5 (2013) 768–773. https://doi.org/10.1021/am302324w.
- [200] C.A. Spindt, I. Brodie, L. Humphrey, E.R. Westerberg, Physical properties of thin-film field emission cathodes with molybdenum cones, Journal of Applied Physics. 47 (1976) 5248–5263. https://doi.org/10.1063/1.322600.
- [201] W. Shi, S. Song, H. Zhang, Hydrothermal synthetic strategies of inorganic semiconducting nanostructures, Chemical Society Reviews. 42 (2013) 5714–5743. https://doi.org/10.1039/C3CS60012B.
- [202] S. Mishra, P. Yogi, S.K. Saxena, J. Jayabalan, P. Behera, P.R. Sagdeo, R. Kumar, Significant field emission enhancement in ultrathin nano-thorn covered NiO nano-petals, J. Mater. Chem. C. 5 (2017) 9611–9618. https://doi.org/10.1039/C7TC01949A.
- [203] S. Ssenyange, H. Yan, R.L. McCreery, Redox-Driven Conductance Switching via Filament Formation and Dissolution in Carbon/Molecule/TiO2/Ag Molecular Electronic Junctions, Langmuir. 22 (2006) 10689–10696. https://doi.org/10.1021/la0611530.
- [204] S. Barman, F. Deng, R.L. McCreery, Conducting Polymer Memory Devices Based on Dynamic Doping, J. Am. Chem. Soc. 130 (2008) 11073–11081. https://doi.org/10.1021/ja802673w.
- [205] O. Niitsoo, S.K. Sarkar, C. Pejoux, S. Rühle, D. Cahen, G. Hodes, Chemical bath deposited CdS/CdSe-sensitized porous TiO2 solar cells, Journal of Photochemistry and Photobiology A: Chemistry. 181 (2006) 306–313. https://doi.org/10.1016/j.jphotochem.2005.12.012.

- [206] A.L. Linsebigler, Guangquan. Lu, J.T. Yates, Photocatalysis on TiO2 Surfaces: Principles, Mechanisms, and Selected Results, Chem. Rev. 95 (1995) 735–758. https://doi.org/10.1021/cr00035a013.
- [207] P.R. Chikate, K.D. Daware, D.S. Gavhane, Y.-R. Ma, R.J. Choudhary, S.I. Patil, M.A. More, D.M. Phase, S.W. Gosavi, P.M. Shirage, R.S. Devan, Controlled Hetero-Architectures of Au-Nanoparticles-Decorated ZnO Nanowires for Enhanced Field Electron Emission Displays, ChemistrySelect. 3 (2018) 7891–7899. https://doi.org/10.1002/slct.201801282.
- [208] V. Paillard, P. Puech, M.A. Laguna, R. Carles, B. Kohn, F. Huisken, Improved one-phonon confinement model for an accurate size determination of silicon nanocrystals, Journal of Applied Physics. 86 (1999) 1921–1924. https://doi.org/10.1063/1.370988.
- [209] R. Wang, G. Zhou, Y. Liu, S. Pan, H. Zhang, D. Yu, Z. Zhang, Raman spectral study of silicon nanowires: High-order scattering and phonon confinement effects, Phys. Rev. B. 61 (2000) 16827–16832. https://doi.org/10.1103/PhysRevB.61.16827.
- [210] V. Kumar, S. K. Saxena, V. Kaushik, K. Saxena, A. K. Shukla, R. Kumar, Silicon nanowires prepared by metal induced etching (MIE): good field emitters, RSC Advances. 4 (2014) 57799–57803. https://doi.org/10.1039/C4RA11093E.
- [211] H.S. Mavi, A.K. Shukla, R. Kumar, S. Rath, B. Joshi, S.S. Islam, Quantum confinement effects in silicon nanocrystals produced by laser-induced etching and cw laser annealing, Semicond. Sci. Technol. 21 (2006) 1627–1632. https://doi.org/10.1088/0268-1242/21/12/021.
- [212] P. Yogi, S.K. Saxena, S. Mishra, H.M. Rai, R. Late, V. Kumar, B. Joshi, P.R. Sagdeo, R. Kumar, Interplay between phonon confinement and Fano effect on Raman line shape for semiconductor nanostructures: Analytical study, Solid State Communications. 230 (2016) 25–29. https://doi.org/10.1016/j.ssc.2016.01.013.
- [213] R. Kumar, A.K. Shukla, Quantum interference in the Raman scattering from the silicon nanostructures, Physics Letters A. 373 (2009) 2882–2886. https://doi.org/10.1016/j.physleta.2009.06.005.
- [214] T. Edvinsson, Optical quantum confinement and photocatalytic properties in two-, one- and zero-dimensional nanostructures, Royal Society Open Science. 5 (n.d.) 180387. https://doi.org/10.1098/rsos.180387.
- [215] R. Kumar, G. Sahu, S.K. Saxena, H.M. Rai, P.R. Sagdeo, Qualitative Evolution of Asymmetric Raman Line-Shape for NanoStructures, Silicon. 6 (2014) 117–121. https://doi.org/10.1007/s12633-013-9176-9.
- [216] S. K. Saxena, P. Yogi, S. Mishra, H. Mohan Rai, V. Mishra, M. Kamal Warshi, S. Roy, P. Mondal, P. R. Sagdeo, R. Kumar, Amplification or cancellation of Fano resonance and quantum confinement induced asymmetries in Raman line-shapes, Physical Chemistry Chemical Physics. 19 (2017) 31788–31795. https://doi.org/10.1039/C7CP04836J.